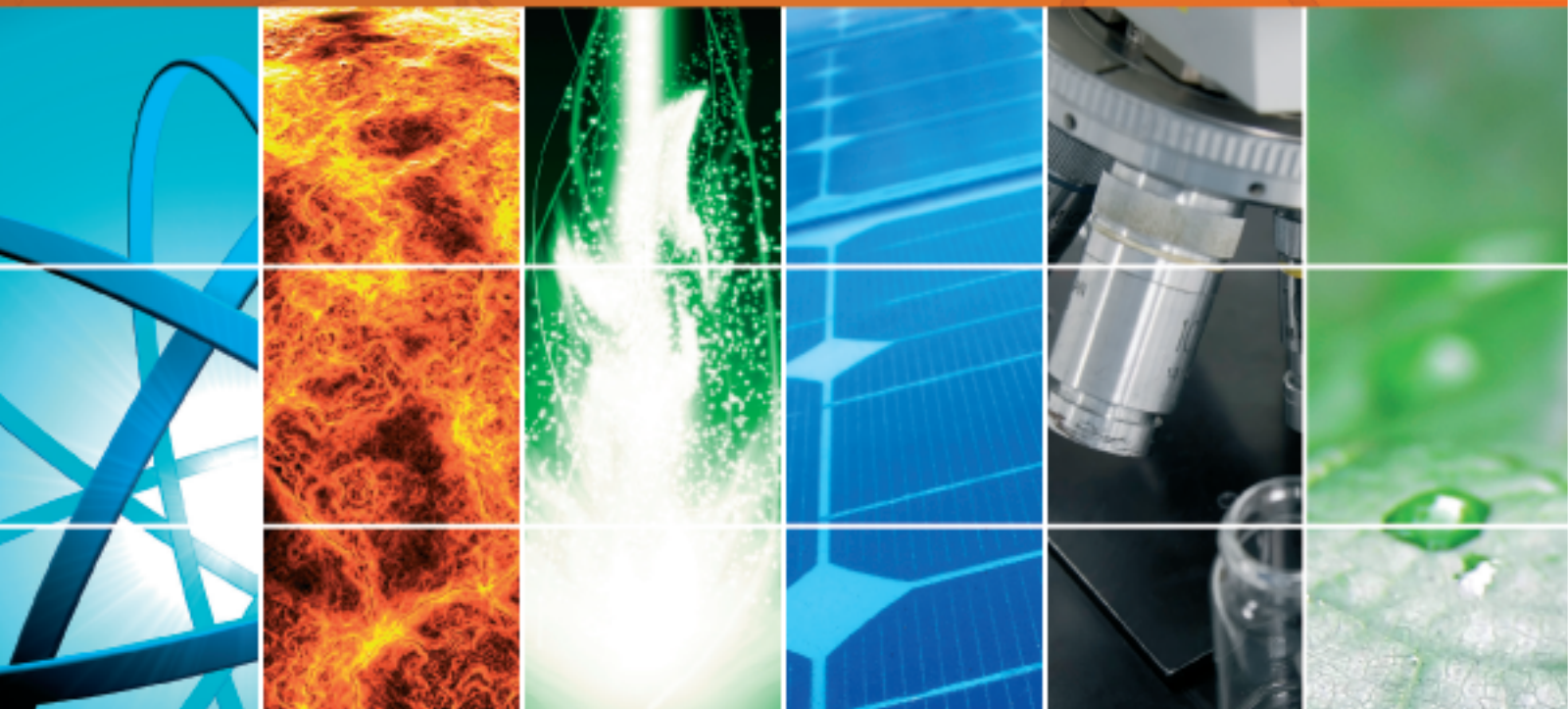


Heterojunction Solar Cells

Guest Editors: Aung Ko Ko Kyaw, Antonio Otavio T. Patrocínio,
Dewei Zhao, and Victor Brus





Heterojunction Solar Cells

International Journal of Photoenergy

Heterojunction Solar Cells

Guest Editors: Aung Ko Ko Kyaw, Antonio Otavio T. Patrocínio,
Dewei Zhao, and Victor Brus



Copyright © 2014 Hindawi Publishing Corporation. All rights reserved.

This is a special issue published in "International Journal of Photoenergy." All articles are open access articles distributed under the Creative Commons Attribution License, which permits unrestricted use, distribution, and reproduction in any medium, provided the original work is properly cited.

Editorial Board

- M. S. Abdel-Mottaleb, Egypt
Xavier Allonas, France
Nicolas Alonso-Vante, France
Wayne A. Anderson, USA
Yanhui Ao, China
Vincenzo Augugliaro, Italy
Detlef W. Bahnemann, Germany
Mohammad A. Behnajady, Iran
Ignazio Renato Bellobono, Italy
Raghu N. Bhattacharya, USA
Prmod H. Borse, India
Gion Calzaferri, Switzerland
Adriana G. Casas, Argentina
Chuncheng Chen, China
Sung Oh Cho, Republic of Korea
Wonyong Choi, Republic of Korea
Věra Cimrová, Czech Republic
Juan M. Coronado, Spain
Ying Dai, China
Vikram Dalal, USA
Dionysios D. Dionysiou, USA
Pingwu Du, China
Mahmoud M. El-Nahass, Egypt
Polycarpos Falaras, Greece
Chris Ferekides, USA
Paolo Fornasiero, Italy
Hermenegildo García, Spain
Elisa Isabel Garcia-Lopez, Italy
Beverley Glass, Australia
M. A. Gondal, Saudi Arabia
Jr-Hau He, Taiwan
Shinya Higashimoto, Japan
Wing-Kei Ho, Hong Kong
Cheuk-Lam Ho, Hong Kong
Fuqiang Huang, China
Adel A. Ismail, Egypt
Chun-Sheng Jiang, USA
Misook Kang, Republic of Korea
Shahed Khan, USA
Jong Hak Kim, Republic of Korea
- Sungjee Kim, Republic of Korea
Sun-Jae Kim, Republic of Korea
Cooper H. Langford, Canada
Tae-Woo Lee, Republic of Korea
Lecheng Lei, China
Zhaosheng Li, China
Xinjun Li, China
Yuexiang Li, China
Stefan Lis, Poland
Gongxuan Lu, China
Dongge Ma, China
Niyaz M. Mahmoodi, Iran
Nai Ki Mak, Hong Kong
Rajaram S. Mane, India
Dionissios Mantzavinos, Greece
Ugo Mazzucato, Italy
Sheng Meng, China
Jacek Miller, Poland
Claudio Minero, Italy
Jarugu N. Moorthy, India
Antoni Morawski, Poland
Franca Morazzoni, Italy
Fabrice Morlet-Savary, France
Mohammad Muneer, India
Kun Na, Republic of Korea
Ebinazar B. Namdas, Australia
Maria da Graça Neves, Portugal
Tebello Nyokong, South Africa
Kei Ohkubo, Japan
Haridas Pal, India
Leonidas Palilis, Greece
Leonardo Palmisano, Italy
Ravindra K. Pandey, USA
H. Park, Republic of Korea
David Lee Phillips, Hong Kong
Pierre Pichat, France
Gianluca Li Puma, UK
Xie Quan, China
Tijana Rajh, USA
Peter Robertson, UK
- Avigdor Scherz, Israel
Elena Selli, Italy
Ganesh D. Sharma, India
Jinn Kong Sheu, Taiwan
Panagiotis Smirniotis, USA
Zofia Stasicka, Poland
Elias Stathatos, Greece
M. Swaminathan, India
Kazuhiro Takanabe, Saudi Arabia
K. R. Justin Thomas, India
Yang Tian, China
Gopal N. Tiwari, India
Nikolai V. Tkachenko, Finland
Ahmad Umar, Saudi Arabia
Veronica Vaida, USA
Roel van De Krol, Germany
Mark van Der Auweraer, Belgium
Sheng Wang, China
Xuxu Wang, China
Mingkuai Wang, China
Ezequiel Wolcan, Argentina
Man Shing Wong, Hong Kong
David Worrall, UK
Jeffrey C. S. Wu, Taiwan
Fahrettin Yakuphanoglu, Turkey
Yanfa Yan, USA
Jiannian Yao, China
Minjoong Yoon, Republic of Korea
Hongtao Yu, USA
Jimmy C. Yu, Hong Kong
Jiangbo Yu, USA
Ying Yu, China
Klaas Zachariasse, Germany
Juan Antonio Zapien, Hong Kong
Tianyou Zhai, China
Lizhi Zhang, China
Jincai Zhao, China
Yong Zhou, China
Guijiang Zhou, China
Rui Zhu, China

Contents

Heterojunction Solar Cells, Aung Ko Ko Kyaw, Antonio Otavio T. Patrocínio, Dewei Zhao, and Victor Brus
Volume 2014, Article ID 163984, 2 pages

Design of a Free-Ruthenium In_2S_3 Crystalline Photosensitized Solar Cell, Byeong Sub Kwak, Younghwan Im, and Misook Kang
Volume 2014, Article ID 375746, 8 pages

Nanopatterned Silicon Substrate Use in Heterojunction Thin Film Solar Cells Made by Magnetron Sputtering, Shao-Ze Tseng, Chang-Rong Lin, Hung-Sen Wei, Chia-Hua Chan, and Sheng-Hui Chen
Volume 2014, Article ID 707543, 10 pages

Doped Heterojunction Used in Quantum Dot Sensitized Solar Cell, Yanyan Gao, Xiaoping Zou, and Zongbo Huang
Volume 2014, Article ID 179289, 7 pages

Excellent Silicon Surface Passivation Achieved by Industrial Inductively Coupled Plasma Deposited Hydrogenated Intrinsic Amorphous Silicon Suboxide, Jia Ge, Muzhi Tang, Johnson Wong, Zhenhao Zhang, Torsten Dippell, Manfred Doerr, Oliver Hohn, Marco Huber, Peter Wohlfart, Armin G. Aberle, and Thomas Mueller
Volume 2014, Article ID 752967, 12 pages

Ultrathin Anode Buffer Layer for Enhancing Performance of Polymer Solar Cells, Dun Wang, Jian Wang, Ling-liang Li, Qiao-shi An, Hui Huang, Chao-qun Jiao, Yang Liu, and Fu-jun Zhang
Volume 2014, Article ID 846581, 6 pages

The Promotion of the Efficiency of Organic Photovoltaic Devices by Addition of Anisotropic CdSe Nanocrystals, Shu-Ru Chung, Hong-Shuo Chen, Chen-Yu Chien, Meng-Yi Bai, and Kuan-Wen Wang
Volume 2014, Article ID 219123, 8 pages

Editorial

Heterojunction Solar Cells

Aung Ko Ko Kyaw,¹ Antonio Otavio T. Patrocínio,² Dewei Zhao,³ and Victor Brus⁴

¹ Institute of Materials Research and Engineering (A* STAR), 3 Research Link, Singapore 117602

² Institute of Chemistry, Federal University of Uberlandia, Uberlandia, MG, Brazil

³ Department of Electrical Engineering and Computer Science, the University of Michigan, Ann Arbor, MI 48109, USA

⁴ Department of Electronics and Energy Engineering, Chernivtsi National University, Chernivtsi 58000, Ukraine

Correspondence should be addressed to Aung Ko Ko Kyaw; aung0069@ntu.edu.sg

Received 11 August 2014; Accepted 11 August 2014; Published 24 August 2014

Copyright © 2014 Aung Ko Ko Kyaw et al. This is an open access article distributed under the Creative Commons Attribution License, which permits unrestricted use, distribution, and reproduction in any medium, provided the original work is properly cited.

With endless energy demand and climate change issue, solar cells which convert sun light directly into electricity are becoming increasingly important in the world's renewable energy mix. The development of new solar cell technologies with lower production costs is therefore of great interest to industry. New and prospective materials are under intensive research in order to create low cost and highly efficient photovoltaic devices based on various organic, hybrid organic-inorganic, and inorganic heterojunctions. Heterojunction solar cells possess a combination of unique properties of different materials that helps to improve their operational characteristics comparing with traditional homojunction silicon solar cells.

In this special issue, we selected 6 peer-reviewed research articles which present the recent developments in various types of heterojunction solar cells, including organic bulk-heterojunction solar cells, dye/quantum dot sensitized solar cells, hybrid organic-inorganic solar cells, and inorganic heterojunction solar cells. A broad range of topics, from material synthesis and thin film deposition technique to device architecture, are discussed in this special issue. A brief overview of each paper highlighting the key result and discovery is as follows.

In the paper “*Design of a free-ruthenium In₂S₃ crystalline photosensitized solar cell*,” a new sulfide-based solid state sensitizer was assessed as a potential replacement for traditional Ru-based dyes. The morphology of In₂S₃ on TiO₂ films was investigated and the role of its concentration on the overall conversion efficiency of DSCs was discussed.

The paper “*Nanopatterned silicon substrate use in heterojunction thin film solar cells made by magnetron sputtering*” proposed a method for the fabrication of novel nanopatterned silicon heterojunction thin film solar cells ITO/p-type a-Si:H/n-type c-Si. The nanopatterned silicon wafers with a self-assembled monolayer of SiO₂ nanospheres 550 nm in diameter were used in order to achieve 31.49% higher efficiency comparing to that of heterojunction solar cells based on planar silicon substrates.

In “*Doped heterojunction used in quantum dot sensitized solar cell*,” quantum dot sensitized solar cells with indium-doped PbS/CdS QDs forming In-PbS/In-CdS heterojunction were presented by successive ionic layer adsorption and reaction method. Such an incorporation results in the light harvesting of heterojunction, leading to enhanced device performance.

In “*Excellent silicon surface passivation achieved by industrial inductively coupled plasma deposited hydrogenated intrinsic amorphous silicon suboxide*,” authors present an alternative method of depositing a high-quality passivation film for silicon solar cells. The deposition of hydrogenated intrinsic amorphous silicon suboxide was accomplished by decomposing hydrogen, silane, and carbon dioxide in an industrial remote inductively coupled plasma platform. Through the precise control of CO₂ partial pressure and process temperature, excellent surface passivation quality and optical properties were achieved.

In the paper “*Ultrathin anode buffer layer for enhancing performance of polymer solar cells*,” an enhanced polymer

solar cell was achieved by adding an ultrathin layer of lithium fluoride in between PEDOT:PSS and polymer active layer. The dominant mechanism for performance improvement was explained as the increased charge collection by anode buffer layers.

In the paper “*The promotion of the efficiency of organic photovoltaic devices by addition of anisotropic CdSe nanocrystals*,” CdSe nanocrystals with different morphologies such as tetrapod and nanorod were synthesized by seed growth method and applied as the acceptor in the active layer of the organic photovoltaic (OPV) devices. When the concentration of CdSe in P3HT: PCBM system is 50 wt% optimally, the efficiency can be promoted about 4.3%.

We do believe that the collection of papers from multidisciplinary areas will benefit the community of heterojunction solar cell research for the further development of this research area.

Acknowledgments

We would like to express our sincere appreciation to all the authors for submitting their exciting scientific results to this special issue. We are also grateful to all the reviewers around the world, whose dedicated efforts and high-quality work have made this issue possible. Last but not least, we would like to thank the editorial board of International Journal of Photoenergy for giving us opportunity to publish this special issue.

*Aung Ko Ko Kyaw
Antonio Otavio T. Patrocinio
Dewei Zhao
Victor Brus*

Research Article

Design of a Free-Ruthenium In_2S_3 Crystalline Photosensitized Solar Cell

Byeong Sub Kwak, Younghwan Im, and Misook Kang

Department of Chemistry, College of Science, Yeungnam University, Gyeongsan, Gyeongbuk 712-749, Republic of Korea

Correspondence should be addressed to Misook Kang; mksang@ynu.ac.kr

Received 13 March 2014; Revised 17 May 2014; Accepted 3 June 2014; Published 7 July 2014

Academic Editor: Antonio Otavio Patrocinio

Copyright © 2014 Byeong Sub Kwak et al. This is an open access article distributed under the Creative Commons Attribution License, which permits unrestricted use, distribution, and reproduction in any medium, provided the original work is properly cited.

A new type of sulfide-based, solid-state dye material that is sensitive to visible radiation was assessed as a potential replacement for commercial ruthenium complex dyes in a dye-sensitized solar cell (DSSC) assembly. The In_2S_3 crystals on the surface of the TiO_2 bottom blocking layer were grown as a solid-state dye material. Scanning electron microscopy of In_2S_3 revealed a microsized, 3D-connected sheet-like shape, which was confirmed by X-ray diffraction to be a beta-structure. The efficiency of the dye-sensitized solar cells assembled with a layer grown with In_2S_3 increased with increasing In_2S_3 mole concentrations to 0.05 M (1.02%) but decreased at concentrations greater than 0.6~0.8%. This suggests that crystalline In_2S_3 acts as a dye sensitized to visible radiation, but the short-circuit current density is too low compared to the commercially available ruthenium dye. This suggests that In_2S_3 crystals did not grow densely but were bulk-grown with large pores, resulting in a smaller amount of In_2S_3 per unit area. Two IPCE curves were observed, which were assigned to TiO_2 and In_2S_3 , meaning that the TiO_2 surfaces were covered completely with In_2S_3 crystals. The exposure of TiO_2 eventually leads to a reaction with the electrolytes, resulting in lower quantum efficiency.

1. Introduction

The increasing demand for energy and the limited oil reserves have highlighted the need for the development of alternative forms of renewable energy. Solar energy is one option proposed to deal with the energy crisis because it is abundant, unlimited, and clean. Sunlight can be harvested and converted directly to electricity using photovoltaic devices [1–5]. Since O'Regan and Gratzel first reported dye-sensitized solar cells (DSSCs) in 1991 [6], there has been continuous research into DSSCs because of their numerous advantages over silicon solar cells, such as low cost, easy assembly, and relatively high efficiency [7–10]. DSSCs are one of the most promising methods for future large-scale energy production from renewable energy sources. DSSCs are composed of four major parts, a semiconducting cathode, Pt anode, iodine electrolyte, and photosensitive dye [11], which is the most important component. The photosensitizer, that is, the dye, in DSSCs should fulfill the following essential characteristics:

- (1) the excited state energy level of the photosensitizer should be higher than that of the conduction band edge of the semiconductor;
- (2) the absorption spectrum of the sensitizer should cover as much as of the visible light and even the near-infrared region as possible;
- (3) the dye molecule should bind to the surface of the semiconductor efficiently through certain anchoring groups;
- (4) the oxidized state level of the sensitizer should match the redox potential of the electrolyte;
- (5) the sensitizer should be photo- and electrochemically and thermally stable.

Over the last 20 years, ruthenium (II) complexes based on carboxylic pyridine ruthenium compounds, such as N3 [12], N719 [13], N907 [14], and black dye [15], have shown a clear lead in the solar cell performance. The best solar-to-electricity

conversion efficiency of >10% was achieved using these ruthenium-complex photosensitizers. On the other hand, ruthenium-complex photosensitizers tend to deteriorate the lifespan of the cell, making the photosensitizers unstable under thermal stress and light soaking [16, 17].

Therefore, it is important to explore novel inorganic sensitizers composed of transition metals. Recently, as an alternative to dye sensitizers, narrow-band gap semiconducting quantum dots, such as CdS [18], CdSe [1], PbS [19], Sb₂S₃ [20], and CuInS₂ [21], have also been tested as photosensitizers. These cells are called quantum dot-sensitized solar cells (QDSSCs). The use of semiconductor QDs as sensitizers has the following advantages in solar cell applications over conventional dyes: possible tuning of the visible response by changing the QD size [22], large intrinsic dipole moment resulting from quantum confinement and a high extinction coefficient [23], possible multiple electron-hole pairs [24], and a potential theoretical maximum efficiency of 31% [25]. Although the above advantages are quite promising, the efficiencies of QDSSCs (typically below 5%) are much lower than that of DSSCs (ca. 10%). One of the reasons for the poor performance of QDSSCs is the difficulty in assembling the QDs on a mesoporous TiO₂ matrix to obtain a well-covered QD layer on the TiO₂ surface. Therefore, new metal sulfide materials including QDs, which are easier to manufacture, absorb visible light easily, and have excellent electron-transfer ability, are needed.

Although many studies have assessed a range of metal sulfide materials for solar cell applications, there are no reports of a detailed study of In₂S₃ for solar cell applications. Therefore, In₂S₃ was evaluated as a photosensitizer in this study. The In₂S₃ is an excellent electron donor, and three different structures are as follows: yellow α -In₂S₃ has a defect cubic structure; red β -In₂S₃ has a defect spinal, tetragonal structure; and γ -In₂S₃ has a layered structure. The β -form is believed to be the most stable form at room temperature. In addition, it is diamagnetic and exhibits n-type semiconductivity with an optical band gap of 2.1 eV [26]. In₂S₃ crystals are grown directly onto the surface of a TiO₂ seed layer electrode using a chemical bath deposition (CBD) method [27], and its photosensitive effect in DSSCs is discussed.

2. Experimental

2.1. In₂S₃ Crystals Grown over TiO₂ Seed Blocking Layers and Their Characterization. In₂S₃ crystals were grown on the surface of the TiO₂ seed blocking layer using a general CBD method [28]. First, a sol-gel dip-coating technique was used to fabricate a TiO₂ seed blocking layer onto a fluorine-doped tin oxide (FTO) conducting glass plate (Hartford, 30 ohm cm⁻² and 80% transmittance in visible region). A FTO glass substrate, which covered one side with black tape, was dipped into a 0.1 M TTIP ethanol solution fixed at pH = 2.5 with acetic acid and aged for 24 h. The prepared TiO₂ blocking layer film was then annealed at 450°C for 30 minutes in air to remove the additives. In the secondary step, the In₂S₃ crystals were grown on the TiO₂ seed blocking layer using thiourea ((NH₂)₂C=S, 99.9%, Junsei Chemical, Japan)

and indium chloride (InCl₃, 99.9%, Junsei Chemical, Japan) as the S and In precursors, respectively. Indium chloride (0.001~0.5 M) was dissolved in distilled water, and thiourea (0.0015~0.75 M) was then added slowly with stirring. The solution was fixed to pH = 2.5 using acetic acid. After stirring homogeneously for 2 h, the final solution was transferred to an autoclave, which included a TiO₂ seed blocking layered glass, and treated thermally at 80°C for 24 h. The resulting glass was washed with ethanol and dried at 60°C for 24 h. Here, a TiO₂ paste was not used. Instead, the TiO₂ seed blocking layer eventually acted as a working electrode.

2.2. Assembly of TiO₂ Seed Blocking/In₂S₃ Photosensitizer Layered-Solar Cells. To prepare a solar cell, a working TiO₂ seed blocking/In₂S₃ photosensitizer layered electrode was covered with a Pt-coated FTO counterelectrode, and the edges of the cell were sealed with a sealing sheet (PECHM-1, Mitsui-Dupont Polychemical) at 110°C. The used redox electrolyte consisted of 0.5 mol KI, 0.05 mol I₂, and 0.5 mol 4-tert-butylpyridine with an acetonitrile solvent. Sufficient electrolyte was injected into cells using a vacuum pump.

2.3. Characterization. The prepared TiO₂ (bottom)/In₂S₃ (top) films were examined by X-ray diffraction (XRD; MPD, PANalytical) using nickel-filtered CuK α radiation (40 kV, 30 mA). The surface morphology of the film was examined by scanning electron microscopy (SEM, S-4100, Hitachi). Cyclic voltammetry (CV, BAS 100B) of the TiO₂ and In₂S₃ powder disc was performed at room temperature at a scan rate of 100 mV s⁻¹ in an electrolyte composed of 0.5 mol KI, 0.05 mol I₂, and 0.5 mol 4-tert-butylpyridine in acetonitrile. Platinum wire was used as the working and counterelectrodes, and Ag/AgCl was used as the reference electrode. The UV-visible (Cary 500 spectrometer) spectra of TiO₂ (bottom)/In₂S₃ (top) films were obtained using a reflectance sphere in the range, 200~800 nm.

The photovoltaic efficiency of the TiO₂ seed blocking/In₂S₃ photosensitizer layered-solar cells was calculated from the *I-V* curves that had been determined using a Sun 2000 solar simulator (ABET technology) equipped with a xenon lamp (max. 150 W). The light intensity of the solar simulator was equivalent to one sun at AM 1.5. The instrument was calibrated using a c-Si reference cell. The spectral output of the lamp was matched in the region, 350~800 nm, using a Schott KG-5 sunlight filter to reduce the mismatch between the simulated and true solar spectrum to less than 2%. The incident light intensity and active cell area were 100 mWcm⁻² and 0.40 cm² (0.8 × 0.5 cm), respectively. The solar cell was measured at room temperature using a shading mask and the aperture area was used for the calculation. The major factors determining the efficiencies of the solar cells were the open-circuit voltage (*V*_{oc}), short-circuit current density (*J*_{sc}), and fill factor (FF).

Using the same equipment, the equilibrium conditions are important considerations in the IPCE measurements, where the spectral response is obtained under short-circuit conditions. In AC mode, the test SC was illuminated by monochromatic light with the addition of simulated AM 1.5 G

solar light to represent the solar cell working conditions. The photocurrent responding to monochromatic light was measured precisely using a lock-in amplifier at a frequency that was also applied to a mechanical chopper to modulate the monochromatic light. The total photocurrent could be estimated from the IPCE spectra by integrating the incident photon flux density, $I_{\text{photon}}(\lambda)$, and IPCE (λ) over the wavelength of incident light, which is expressed as [28]

$$J = q_e \int I_{\text{photon}}(\lambda) \cdot \text{IPCE}(\lambda) d\lambda, \quad (1)$$

where J is the photocurrent, q_e is the electron charge, and λ is the wavelength.

3. Results and Discussion

3.1. Physicochemical Properties of the TiO₂ Seed Blocking/In₂S₃ Photosensitizer Layered Film. Figure 1 shows XRD patterns of the prepared TiO₂ seed blocking/In₂S₃ photosensitizer (0.001, 0.01, 0.05, 0.1, and 0.5 M) layered films. Anatase TiO₂ [29] and tetragonal tin oxide [30] induced from the FTO glass were observed in the In₂S₃ film sample grown using the 0.001 M-In precursor, but no peaks were assigned to β -In₂S₃. On the other hand, with the exception of the 0.001 M-In precursor sample, all the diffraction peaks of the samples were indexed to β -In₂S₃ with a Fd-3m space group, which are in good agreement with the data reported in the literature [31]. Compared to the standard card, the relative intensities of the peaks at 14.3° (111 plane), 23.4° (220), 27.4° (311), 28.5° (222), 33.4° (400), 36.2° (331), 40.9° (422), 43.7° (511), 47.8° (440), 55.8° (533), 59.3° (444), 67.0° (731), 69.6° (800), 77.1° (751), 79.1° (840), and 88.9° (844) were obvious. The (311) XRD peak is normally the strongest. The mean crystalline sizes of the samples containing 0.001, 0.01, 0.05, 0.1, and 0.5 M of the In₂S₃ photosensitizer, which was calculated using Scherrer's equation, $D = \kappa\lambda/\beta \cos \theta$, were 48.10, 19.78, 36.21, 18.10, and 21.72 nm, respectively.

Figures 2(a) and 2(b) show a high-magnification SEM image (top view and side view) of the In₂S₃ crystals grown over the TiO₂ seed blocking layer. The TiO₂ seed blocking layer thickness was approximately 0.5 μm in all samples and the depths of the grown In₂S₃ crystals increased from 0.7 to 5.0 μm . The 3D-structured and connected sheet-like In₂S₃ particles were observed. According to the In₂S₃ concentration, the sheets on the top view were largely grown and the pore sizes were larger. The densities also increased with increasing In₂S₃ concentration to 0.05 M but decreased at concentrations >0.05 M.

Figures 3(a) and 3(b) present the UV-visible absorption spectra and Tauc's plot of the TiO₂ seed blocking/In₂S₃ photosensitizer (0.001, 0.01, 0.05, 0.1, and 0.5 M) layered films, respectively. This is a practical method for estimating the energy gap from an extrapolation of the absorption edge intercept on the x -axis or of that at the excitonic (shoulder) peak, called $\lambda_{1/2}$. The absorption spectra had a steeper absorption edge, which is similar to the results obtained from the Tauc equation [32]. The absorption band of the TiO₂ film normally appears at approximately 350 nm. According

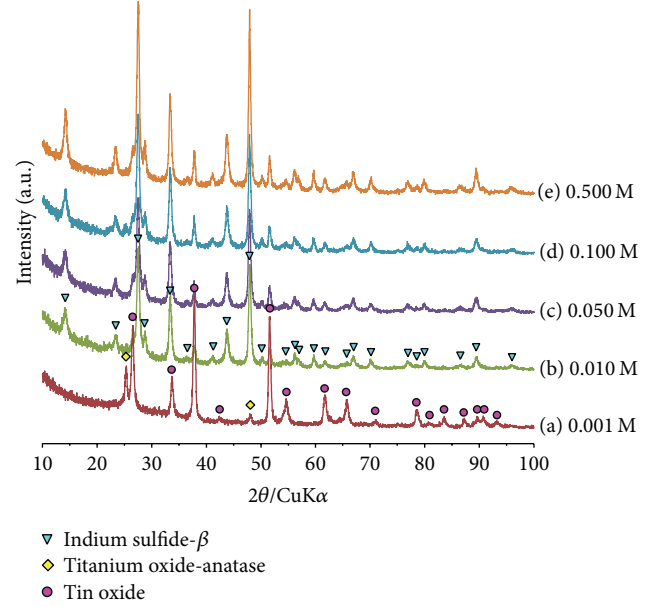


FIGURE 1: The XRD patterns of the prepared TiO₂ seed blocking/In₂S₃ photosensitizer (0.001, 0.01, 0.05, 0.1, and 0.5 M) layered films.

to the concentrations of the grown In₂S₃, the absorption bands shifted to a higher wavelength around the maximum, 450~650 nm. The band gap of semiconductor materials is closely related to the wavelength absorbed, where the band gap decreases with increasing absorption wavelength. The band gap can be calculated from the following Tauc equation: $(\alpha h\nu)^n = B(h\nu - E_g)$, where $h\nu$ is the photon energy, α is the absorption coefficient, B is a constant relative to the material, and the exponent n is a value that depends on the nature of the transition (2 for a direct allowed transition, 2/3 for a direct forbidden transition, and 1/2 for an indirect allowed transition). The band gap obtained by extrapolating the linear portion of the graph in the 0.05 M In₂S₃ photosensitizer layered on TiO₂ seed blocking (700 nm) was approximately 1.72 eV. In contrast, the TiO₂ seed blocking layered film had a band gap of 2.81 eV. Generally, the band gap of anatase TiO₂ is approximately 3.02 eV. On the other hand, the absorption in the visible region was attributed to the transition from the ground state to a few defects. This excitation character of the absorption spectra indicated the excellent crystal quality of the semiconductor. A redshift was observed in the optical absorption spectra of the TiO₂ hexagonal columns, which indicated that the TiO₂ particles showed quantum confinement related effects. This absorption in the visible region was attributed more to the transition from the ground state to a few defect-related deep states [33–35]: the value of E_g for bulk CdS was 2.5 eV, but a wide range of E_g values have been reported for CdS thin films depending mainly on the deposition technique. Evaporated CdS films with band gaps as low as 2.2 eV and chemically deposited CdS films with band gaps as high as 2.6 eV have been reported. These high E_g values for CdS have been attributed to quantum confinement effects due to the small grain size of the polycrystalline films.

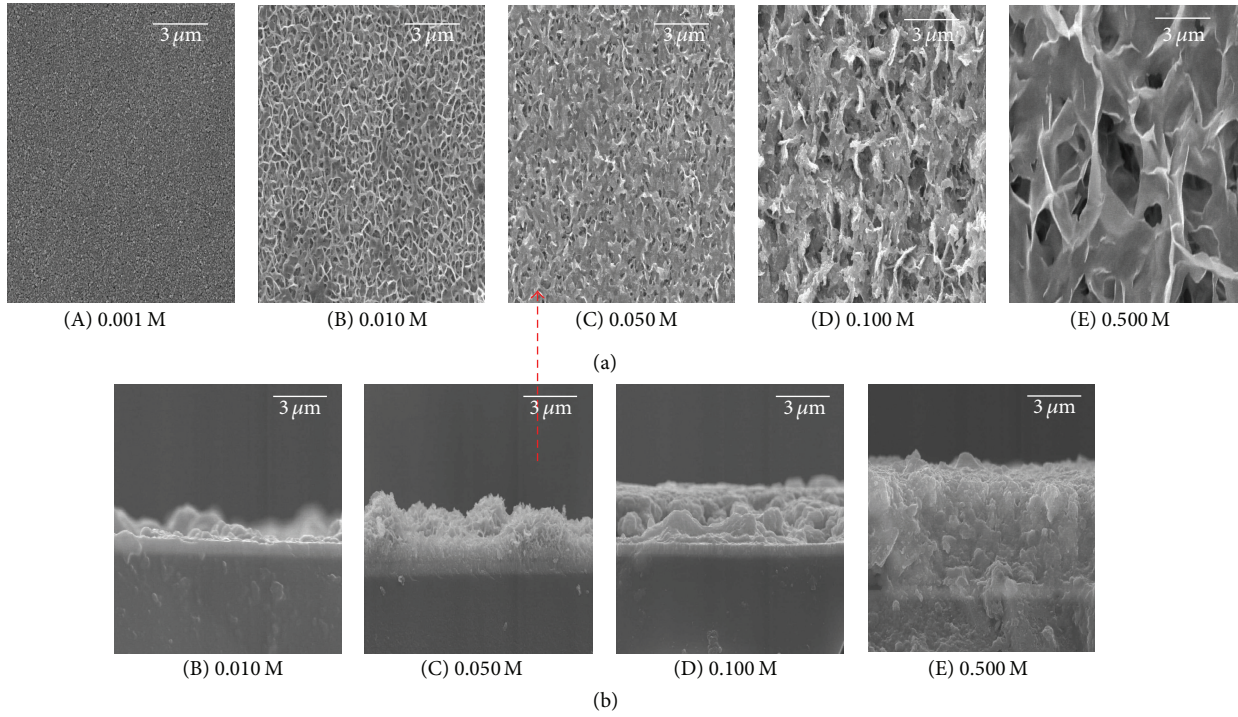


FIGURE 2: High-magnification SEM images (top view (a) and side view (b)) of the In_2S_3 crystals grown on TiO_2 seed blocking layer.

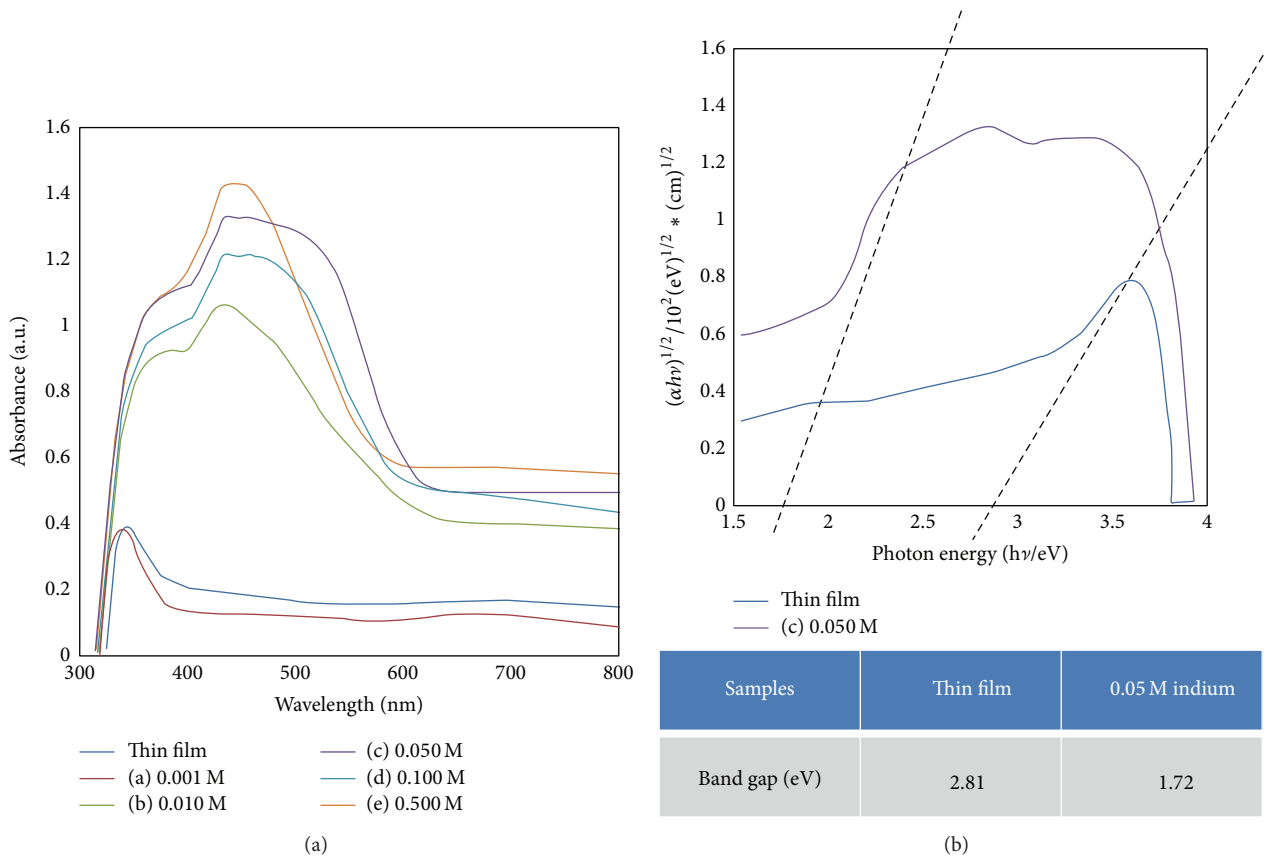


FIGURE 3: UV-visible absorption spectra (a) and Tauc's plots (b) of the TiO_2 seed blocking/ In_2S_3 photosensitizer (0.001, 0.01, 0.05, 0.1, and 0.5 M) layered films.

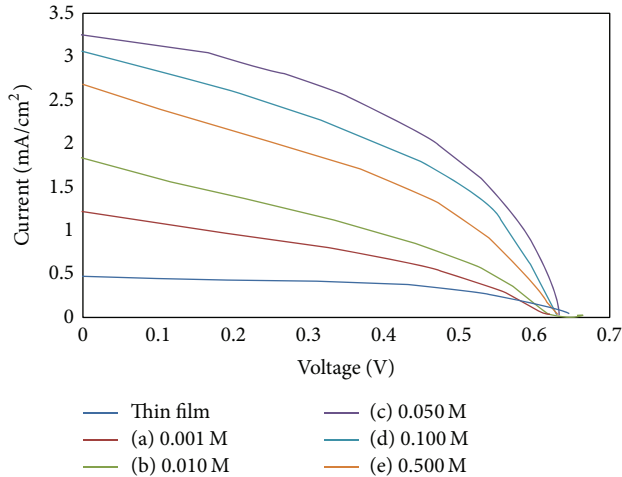


FIGURE 4: I - V curve (up) and photovoltaic efficiencies (down) of the TiO_2 seed blocking/ In_2S_3 photosensitizer layered-solar cells.

Consequently, the band gap can be varied according to the particle size or crystal defects. In addition, the band gap indicates that its electronic properties changed due to the small particle sizes of TiO_2 , indicating that the energy of the lowest excited state of the sample and heat treatment depend on their size: the highest energy is reached at a smaller particle size. The band gap energies could be explained by the volume conservation law, which states that an increase in at least one lattice constant should be compensated for by a decrease in another and vice versa, as is the case in the low-energy regions. Therefore, anatase (2.81 eV) shows an almost linear decrease in the band gap with increasing volume or decreasing lattice constant. A smaller band gap is achieved by compressing the lattice constant [36, 37]. Because the semiconductor electrode plays an important role in accepting electrons and donating them to the solar cells, its light absorption is important. This suggests that In_2S_3 effectively absorbs a large range of visible light similar to commercial ruthenium dyes.

3.2. Photovoltaic Efficiency and Electronic Properties of the TiO_2 Seed Blocking/ In_2S_3 Photosensitizer Layered-Solar Cells. Figure 4 shows the I - V curve (up) and photovoltaic efficiencies (down) of the TiO_2 seed blocking/ In_2S_3 photosensitizer layered-solar cells. The TiO_2 nanoparticles typically used in DSSCs have a diameter of approximately 10~30 nm, through which it is easy for the long wavelengths of light to permeate.

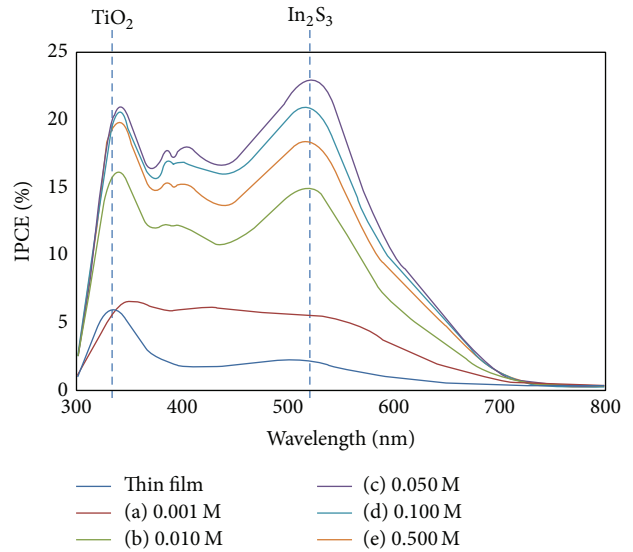


FIGURE 5: Incident photon-to-current conversion efficiencies of the TiO_2 seed blocking/ In_2S_3 photosensitizer layered-solar cells.

Unfortunately, long-wavelength light is not used effectively in solar cells. In recent years, DSSCs assembled with a second layer film with a 4~5 μm thickness comprised of large nanoparticles or nanopores coated on the top of a dense TiO_2 electrode exhibited improved efficiency. The added second layer consisting of TiO_2 , 400 nm in size, acts as a scattering material for increasing the incident light path, resulting in an array of photons that in turn improve the current density. This highlights the importance of the scattering materials in a DSSC assembly. On the other hand, a TiO_2 thick film as a second layer or scattering material was not used, and only a 0.5 μm TiO_2 seed blocking layer and 0.7~5 μm In_2S_3 photosensitizer layer were used. The 0.5 μm TiO_2 seed blocking layered-solar cell showed a power conversion efficiency of only 0.20% with $V_{oc} = 0.65$ V and $J_{sc} = 0.52$ mA/cm². This corresponds to the cell without a dye. On the other hand, the cases of the TiO_2 seed blocking/ In_2S_3 photosensitizer layered-solar cells showed a higher J_{sc} . In particular, the current density increased until a In_2S_3 photosensitizer content of 0.05 M. The conversion efficiency was maximized to 1.20% in the TiO_2 seed blocking/0.05 M In_2S_3 photosensitizer layered-solar cell. This suggests that the In_2S_3 crystalline acts as a dye sensitized to visible radiation, even though the short-circuit current density is too small compared to the use of the commercially available ruthenium dye. This suggests that In_2S_3 crystals are not grown densely and are bulk-grown with rather large pores, resulting in the existence of a smaller amount of In_2S_3 per unit area. Moreover, the exposure of TiO_2 eventually leads to a reaction with the electrolytes and a smaller quantum efficiency. Chemical bath deposition provides a high surface coverage of crystals, but a lack of capping agents leads to a broad size distribution as well as a higher density of surface defects of crystals [38]. Therefore, a photoanode with a high crystal loading, fewer surface traps,

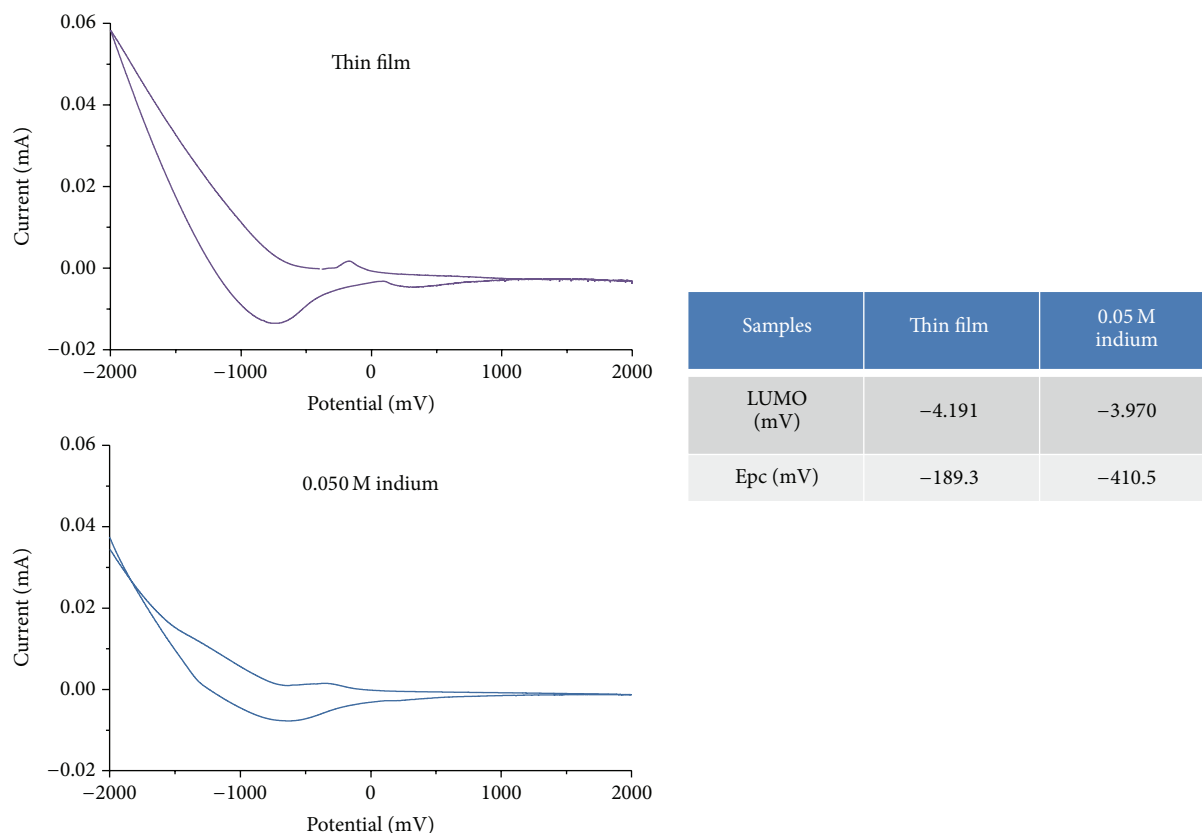


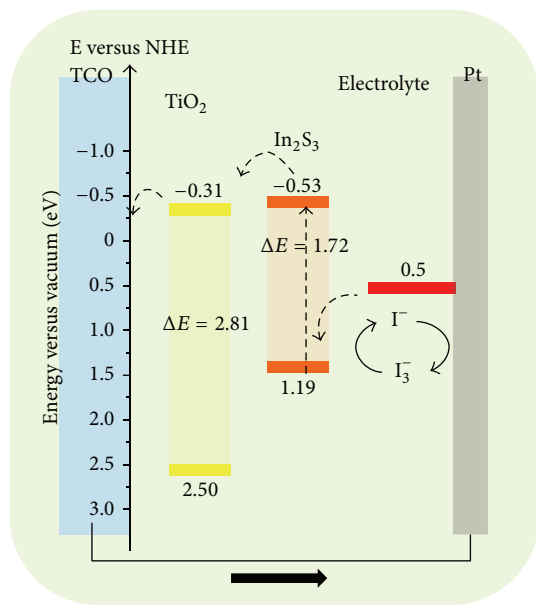
FIGURE 6: Cyclic voltammetry measurements of the TiO_2 and In_2S_3 pellets.

and strong crystals/ TiO_2 electronic coupling is essential for constructing highly efficient solar cells.

The incident photon-to-current conversion efficiencies (IPCE) in Figure 5 indicate the number of incident photons inside the cell as well as their contribution to the conversion efficiency. The commercial ruthenium dyes used in general DSSCs that respond primarily to the wavelength of visible light were measured in the region, 300~750 nm, and reacted at approximately 530 nm, showing the highest quantum number ($\approx 60\sim 80\%$) [39]. Two IPCE curves were observed, which were assigned to TiO_2 and In_2S_3 at a maximum of 320 and 520 nm, respectively, and the curves increased with increasing In_2S_3 concentration. On the other hand, the quantum efficiencies were smaller than those of the commercial ruthenium dyes because the TiO_2 surfaces were not covered perfectly with In_2S_3 crystals. Eventually, the quantum efficiency for visible radiation decreased. The solar cell assembled with a 0.05 M In_2S_3 dye layer showed a maximum quantum efficiency of 22%, resulting in a lower solar conversion to electron efficiency ratio.

Figure 6 shows the cyclic voltammetry measurements for the TiO_2 and In_2S_3 pellets. In the present study, the oxidation potentials were measured by cyclic voltammetry in distilled water solutions. The pelletized samples were used as the working electrodes, Ag/AgCl was used as the reference electrode, and 0.1 M KCl was used as the supporting electrolyte. A reversible wave is needed for the absolute potentials

between the reduction (E_{pc}) and oxidation peaks (E_{pa}). When such reversible peaks are observed, thermodynamic information in the form of a half cell potential $E_{1/2}^0$ can also be determined [40]. Recently, some studies devised a useful equation based on cyclic voltammetry for determining the HOMO and LUMO energy levels. The ferrocene ($E_{1/2}$ versus $\text{Ag}/\text{Ag}^+ = +0.42$ eV) potential, which is used as a standard, should be measured in the electrolyte solution using the same reference electrode, with a fixed -4.8 eV energy level in the vacuum set. The HOMO or LUMO energy levels can be calculated using the following formula: HOMO (or LUMO) (eV) = $-4.8 - (E_{\text{onset}} - E_{1/2(\text{Ferrocene})})$ or E_g (= band gap) = HOMO-LUMO. Here, E_{onset} is the starting point of the redox potential, which was used more often than the peak potential value. In synthesized TiO_2 , the $\text{Ti(IV)} \rightarrow \text{Ti(0)}$ redox reaction appears reversible, and the absolute reduction potential (E_{pc}) was observed at -189.3 mV. Using the Ag/AgCl reference electrode, the onset potential for reduction was determined for In_2S_3 powder and was -410.5 mV. Therefore, the corresponding LUMO energy levels for TiO_2 and In_2S_3 were calculated to be -4.191 and -3.970 eV, respectively. Consequently, these values could change to -0.31 and -0.53 eV depending on the upper equation. In DSSCs, the potential location of the conduction band is more important than the band gap of the semiconductor electrode because it should always be lower than the LUMO level of the dye (normally by 0.2 eV).



SCHEME 1: Model for the potential energy diagram expected from the results of the CV curves and UV-visible spectra.

A model of the potential energy diagram was suggested from the CV curves and UV-visible spectra, as shown in Scheme 1. The conduction band of the TiO_2 blocking layer was located at slightly (0.22 eV) lower energy levels than the LUMO level of the In_2S_3 dye. This suggests that electrons donated from the LUMO of the In_2S_3 dye are transferred easily to the conduction band of the TiO_2 film with less electron loss. The transferred electrons can move easily to the external circuit through the TCO electrode.

4. Conclusions

In this study, β -type In_2S_3 crystals with various concentrations were grown on the surface of the TiO_2 bottom blocking layer by CBD. The grown In_2S_3 crystals were applied to dye-sensitized solar cells as a solid dye. Micron-sized, 3D-connected sheet-like shapes were observed by SEM. The efficiency of the dye-sensitized solar cells prepared from the 0.05 M- In_2S_3 crystals was the highest at 1.02%. Two IPCE curves were observed, which were assigned to TiO_2 and In_2S_3 , respectively. This means that the TiO_2 surfaces are not perfectly covered with In_2S_3 crystals. The exposure of TiO_2 can lead to a reaction with the electrolyte, resulting in an increase in resistance, an interruption of current flow, and a decrease in photoelectric efficiency. These results confirmed that the performance in DSSCs relies on a complete coating method. Therefore, more reliable coating methods will be needed to improve the efficiency.

Conflict of Interests

The authors declare that there is no conflict of interests regarding the publication of this paper.

Acknowledgment

This work was supported by 2013 the Innopolis Daegu Project, Research and Development Special Zones, Republic of Korea, for which the authors are very grateful.

References

- [1] A. Shah, P. Torres, R. Tscharnner, N. Wyrsh, and H. Keppner, "Photovoltaic technology: the case for thin-film solar cells," *Science*, vol. 285, no. 5428, pp. 692–698, 1999.
- [2] A. Hiroki, P. Klaus, S. P. S. Milo, H. W. Alan, and H. F. Richard, "Composites of carbon nanotubes and conjugated polymers for photovoltaic devices," *Advanced Materials*, vol. 11, no. 15, pp. 1281–1285, 1999.
- [3] M. C. Kevin and D. M. Michael, "Conjugated polymer photovoltaic cells," *Chemistry of Materials*, vol. 16, p. 23, 2004.
- [4] M. A. Martínez, J. Herrero, and M. T. Gutiérrez, "Deposition of transparent and conductive Al-doped ZnO thin films for photovoltaic solar cells," *Solar Energy Materials and Solar Cells*, vol. 45, no. 1, pp. 75–86, 1997.
- [5] G. Yu, J. Gao, J. C. Hummelen, F. Wudl, and A. J. Heeger, "Polymer photovoltaic cells: enhanced efficiencies via a network of internal donor-acceptor heterojunctions," *Science*, vol. 270, no. 5243, pp. 1789–1791, 1995.
- [6] B. O'Regan and M. Gratzel, "A low-cost, high-efficiency solar cell based on dye sensitized colloidal TiO_2 films," *Nature*, vol. 353, pp. 737–740, 1991.
- [7] S. Y. Huang, G. Schlichthorl, A. J. Nozik, M. Gratzel, and A. J. Frank, "Kinetics for the recombination of phenyl radicals," *The Journal of Physical Chemistry B*, vol. 101, pp. 14–18, 1997.
- [8] G. K. Mor, K. Shankar, M. Paulose, O. K. Varghese, and C. A. Grimes, "Use of highly-ordered TiO_2 nanotube arrays in dye-sensitized solar cells," *Nano Letters*, vol. 6, no. 2, pp. 215–218, 2006.
- [9] M. Gratzel, "Conversion of sunlight to electric power by nanocrystalline dyesensitized solar cells," *Journal of Photochemistry and Photobiology A*, vol. 164, no. 1–3, pp. 3–14, 2004.
- [10] M. Gratzel, "Dye-sensitized solar cells," *Journal of Photochemistry and Photobiology C*, vol. 4, pp. 145–153, 2003.
- [11] N. Robertson, "Optimizing dyes for dye-sensitized solar cells," *Angewandte Chemie International Edition*, vol. 45, pp. 2338–2345, 2006.
- [12] R. Katoh, A. Furube, T. Yoshihara et al., "Efficiencies of electron injection from excited N_3 dye into nanocrystalline semiconductor (ZrO_2 , TiO_2 , ZnO , Nb_2O_5 , SnO_2 , In_2O_3) films," *Journal of Physical Chemistry B*, vol. 108, no. 15, pp. 4818–4822, 2004.
- [13] W. Zhong-Sheng, K. Hiroshi, K. Takeo, and A. Hironori, "Significant influence of TiO_2 photoelectrode morphology on the energy conversion efficiency of N719 dye-sensitized solar cell," *Coordination Chemistry Reviews*, vol. 248, pp. 1381–1389, 2004.
- [14] P. Wang, B. Wenger, R. Humphry-Baker et al., "Charge separation and efficient light energy conversion in sensitized mesoscopic solar cells based on binary ionic liquids," *Journal of the American Chemical Society*, vol. 127, no. 18, pp. 6850–6856, 2005.
- [15] M. K. Nazeeruddin, P. Pechy, and M. Gratzel, "Efficient panchromatic sensitization of nanocrystalline TiO_2 films by a black dye based on atrithiocyanato-ruthenium complex," *Chemical Communications*, vol. 1997, no. 18, pp. 1705–1706, 1997.

- [16] C. Li, C. Su, H. Wang et al., "Design and development of cyclometalated ruthenium complexes containing thiophenylpyridine ligand for dye-sensitized solar cells," *Dyes and Pigments*, vol. 100, no. 1, pp. 57–65, 2014.
- [17] G. J. Wilson and G. D. Will, "Density-functional analysis of the electronic structure of tris-bipyridyl Ru(II) sensitizers," *Inorganica Chimica Acta*, vol. 363, pp. 1627–1638, 2010.
- [18] D. J. Kim, Y. M. Yu, J. W. Lee, and Y. D. Choi, "Investigation of energy band gap and optical properties of cubic CdS epilayers," *Applied Surface Science*, vol. 254, pp. 7522–7526, 2008.
- [19] S. Thangavel, S. Ganesan, S. Chandramohan, P. Sudhagar, Y. S. Kang, and C. Hong, "Band gap engineering in PbS nanostructured thin films from near-infrared down to visible range by in situ Cd-doping," *Journal of Alloys and Compounds*, vol. 495, no. 1, pp. 234–237, 2010.
- [20] V. P. Zakaznova-Herzog, S. L. Harmer, H. W. Nesbitt, G. M. Bancroft, R. Flemming, and A. R. Pratt, "High resolution XPS study of the large-band-gap semiconductor stibnite (Sb₂S₃): structural contributions and surface reconstruction," *Surface Science*, vol. 600, no. 2, pp. 348–356, 2006.
- [21] G. Chen, L. Wang, X. Sheng, H. Liu, X. Pi, and D. Yang, "Chemical synthesis of Cu(In) metal inks to prepare CuInS₂ thin films and solar cells," *Journal of Alloys and Compounds*, vol. 507, pp. 317–321, 2010.
- [22] A. Kongkanand, K. Tvrđy, K. Takechi, M. Kuno, and P. V. Kamat, "Quantum dot solar cells. Tuning photoresponse through size and shape control of CdSe-TiO₂ architecture," *Journal of the American Chemical Society*, vol. 130, no. 12, pp. 4007–4015, 2008.
- [23] I. Moreels, K. Lambert, D. De Muynck et al., "Composition and size-dependent extinction coefficient of colloidal PbSe quantum dots," *Chemistry of Materials*, vol. 19, no. 25, pp. 6101–6106, 2007.
- [24] L. Jonsson, M. M. Steiner, and J. W. Wilkins, "Coherent electron-hole correlations in quantum dots," *Applied Physics Letters*, vol. 70, no. 9, p. 1140, 1997.
- [25] R. Windisch, P. Heremans, A. Knobloch et al., "Light-emitting diodes with 31% external quantum efficiency by outcoupling of lateral waveguide modes," *Applied Physics Letters*, vol. 74, article 2256, 1999.
- [26] N. Barreau, S. Marsillac, D. Albertini, and J. C. Bernede, "Structural, optical and electrical properties of β -In₂S₃-3xO₃x thin films obtained by PVD," *Thin Solid Films*, vol. 403-404, pp. 331–334, 2002.
- [27] C. D. Lokhande, A. Ennaoui, P. S. Patil et al., "Chemical bath deposition of indium sulphide thin films: preparation and characterization," *Thin Solid Films*, vol. 340, no. 1, pp. 18–23, 1999.
- [28] M. K. Nazeeruddin, A. Kay, I. Rodicio et al., "Solvation changes accompanying proton transfer from a carbon acid to alkoxide bases as revealed by kinetic isotope effects," *Journal of the American Chemical Society*, vol. 115, pp. 14–20, 1993.
- [29] N. Serpone, D. Lawless, and R. Khairutdinov, "Size effects on the photophysical properties of colloidal anatase TiO₂ particles: size quantization or direct transitions in this indirect semiconductor?" *Journal of Physical Chemistry*, vol. 99, no. 45, pp. 16646–16654, 1995.
- [30] R. G. Pavelko, F. Gispert-Guirado, and E. Llobet, "Parametric line profile analysis for in situ XRD of SnO₂ materials: separation of size and strain contributions," *Solid State Ionics*, vol. 255, pp. 21–29, 2014.
- [31] S. Cingarapu, M. A. Ikenberry, D. B. Hamal, C. M. Sorensen, K. Hohn, and K. J. Klabunde, "Transformation of indium nanoparticles to β -indium sulfide: digestive ripening and visible light-induced photocatalytic properties," *Langmuir*, vol. 28, no. 7, pp. 3569–3575, 2012.
- [32] J. Tauc, R. Grigorovich, and A. Vancu, "Optical properties and electronic structure of amorphous germanium," *Physica Status Solidi*, vol. 15, no. 2, pp. 627–637, 1966.
- [33] K. L. Narayanan, K. P. Vijayakumar, K. G. M. Nair, N. S. Thampi, and K. Krishan, "Structural transformation of dip coated CdS thin films during annealing," *Journal of Materials Science*, vol. 32, no. 18, pp. 4837–4840, 1997.
- [34] D. Lincot, B. Mokili, M. Froment et al., "Phase transition and related phenomena in chemically deposited polycrystalline cadmium sulfide thin films," *Journal of Physical Chemistry B*, vol. 101, no. 12, pp. 2174–2181, 1997.
- [35] M. B. Ortuno-Lopez, M. Sotelo-Lerma, A. Mendoza-Galvan, and R. Ramirez-Bon, "Optical band gap tuning and study of strain in CdS thin films," *Vacuum*, vol. 76, no. 2-3, pp. 181–184, 2004.
- [36] H. Mathieu, J. Pascual, and J. Camassel, "Uniaxial stress dependence of the direct-forbidden and indirect-allowed transitions of TiO₂," *Physical Review B*, vol. 18, no. 12, pp. 6920–6929, 1978.
- [37] H. Lin, C. P. Huang, W. Li, C. Ni, S. Ismat Shah, and Y.-H. Tseng, "Size dependency of nanocrystalline TiO₂ on its optical property and photocatalytic reactivity exemplified by 2-chlorophenol," *Applied Catalysis B: Environmental*, vol. 68, no. 1, pp. 1–11, 2006.
- [38] P. K. Nair, M. T. S. Nair, V. M. Garcia et al., "Semiconductor thin films by chemical bath deposition for solar energy related applications," *Solar Energy Materials and Solar Cells*, vol. 52, no. 3-4, pp. 313–344, 1998.
- [39] M. Zalas, B. Gierczyk, M. Klein, K. Siuzdak, T. Pedzinski, and T. Łuczak, "Synthesis of a novel dinuclear ruthenium polypyridine dye for dye-sensitized solar cells application," *Polyhedron*, vol. 67, p. 381, 2014.
- [40] J. Kim, H. Lee, and M. Kang, "Newly designed dye-sensitized solar cells fabricated with double-layered TiO₂ (bottom layer)/B_x-TiO₂ (top layer) combined electrodes for improved photocurrent," *Solar Energy*, vol. 86, no. 9, pp. 2862–2870, 2012.

Research Article

Nanopatterned Silicon Substrate Use in Heterojunction Thin Film Solar Cells Made by Magnetron Sputtering

Shao-Ze Tseng,¹ Chang-Rong Lin,² Hung-Sen Wei,¹
Chia-Hua Chan,² and Sheng-Hui Chen¹

¹ Department of Optics and Photonics, National Central University, 300 Chung-Da Road, Chungli 32001, Taiwan

² Graduate Institute of Energy Engineering, National Central University, 300 Chung-Da Road, Chungli 32001, Taiwan

Correspondence should be addressed to Chia-Hua Chan; hua0121.tw@yahoo.com.tw

Received 16 April 2014; Accepted 18 May 2014; Published 15 June 2014

Academic Editor: Viktor Brus

Copyright © 2014 Shao-Ze Tseng et al. This is an open access article distributed under the Creative Commons Attribution License, which permits unrestricted use, distribution, and reproduction in any medium, provided the original work is properly cited.

This paper describes a method for fabricating silicon heterojunction thin film solar cells with an ITO/p-type a-Si:H/n-type c-Si structure by radiofrequency magnetron sputtering. A short-circuit current density and efficiency of 28.80 mA/cm² and 8.67% were achieved. Novel nanopatterned silicon wafers for use in cells are presented. Improved heterojunction cells are formed on a nanopatterned silicon substrate that is prepared with a self-assembled monolayer of SiO₂ nanospheres with a diameter of 550 nm used as an etching mask. The efficiency of the nanopattern silicon substrate heterojunction cells was 31.49% greater than that of heterojunction cells on a flat silicon wafer.

1. Introduction

More energy is consumed as technology advances. Therefore, the discovery and development of new energy sources have become global issues. In response to global environmental problems, many countries have begun research into green power, including tidal power, wind power, geothermal power, and solar power. Solar energy provides a promising means of satisfying the growing demand for energy, and the development of lower cost and higher efficiency solar cells is being pursued. Silicon-based solar cells account for the largest single share of the photovoltaic market.

Nontandem amorphous silicon (a-Si) thin film solar cells and conventional diffused monocrystalline silicon (c-Si) solar cells are compared herein. The a-Si devices have a higher open-circuit voltage (V_{oc}) and higher energy band gap. However, the conversion efficiency of a-Si devices is lower than that of c-Si devices, because a-Si devices have a narrow range of absorption wavelengths and suffer from photodegradation [1]. In 1992, Sanyo developed a new a-Si/c-Si heterojunction solar cell structure, called HIT (heterojunction with intrinsic thin film), using plasma-enhanced chemical vapor deposition (PECVD) [2]. This structure was newly developed for Si-based solar cells. HIT solar cells have the following three

advantages [3, 4]: (1) high-quality a-Si films that exhibit excellent surface passivation and favorable p-n junction properties, (2) a low processing temperature, and (3) better thermal stability and higher V_{oc} than conventional c-Si solar cells [5]. Most corporations and research institutes use chemical vapor deposition (CVD) methods to prepare a-Si thin films [6–8]. This method has several advantages, including favorable step coverage, the formation of a film of high density owing to the few pinholes and voids formed, and a high deposition rate, but it also has some shortcomings, such as expensive equipment costs, contamination of chemical particles, and the use of extremely toxic gases such as SiH₄, B₂H₆, and PH₃ in the CVD deposition process, which may result in problems of industrial safety and environmental pollution. In contrast, the physical vapor deposition (PVD) method has many advantages, such as nontoxicity, better process control, and lower cost. Therefore, the PVD method was used herein to investigate Si-based heterojunction thin film solar cells.

Sputtering high quality doped/un-doped a-Si films is difficult. The difficulties are that (1) ion bombardment is likely to form an unwanted microstructure in the thin films, reducing their quality, and (2) the PVD processes have

a low doping efficiency, so the number of doping atoms in the sputtering deposition processes should be increased to achieve the same degree of doping as in doped a-Si films that are formed by CVD. Therefore, some research is being performed under way to improve the quality of doped a-Si thin films that are formed by sputtering. In 2001, Ohmura et al. sputtered p-type a-Si films with extra boron grains on a silicon wafer to obtain more dopant boron atoms [9]. In 2002, De Lima et al. deposited p-type a-Si films with extra boron grains by sputtering a Si target; the sputtering increased the number of boron dopant atoms in the p-type a-Si films, yielding the same conductivity as that of a-Si films that are formed by CVD [10].

The reflectance of polished silicon wafers is about 36% at visible wavelengths. Therefore, a simple and powerful way to improve the efficiency of solar cells that are made by sputtering is to increase the number of absorbed photons to increase the photocurrent. Many methods can effectively reduce the Fresnel reflection of silicon-based optical components, such as the application of antireflection coatings (ARCs) [11, 12] and roughening of the surface. A single-layered antireflection thin film can only reflect particular wavelengths, whereas a multilayer coating is more effective for reflecting a broad range of wavelengths. Unfortunately, ARCs are made from limited materials and they suffer from such shortcomings as thermal mismatch, which is caused by lamination, and the need for expensive and complicated equipment to fabricate them.

Surface roughening is used in various applications, for example, LEDs [13, 14], MENS devices, and solar cells [15–19]. As more advanced fabrication methods have been developed, periodic antireflection structures have attracted increasing interest. Moth-eye antireflection structures are the most well-known [20, 21]. Periodic structures can generally be divided into microstructures and nanostructures based on their critical dimension. Various techniques can be used to fabricate and pattern a nanostructure substrate, including E-beam lithography, nanoimprint lithography [22, 23], holographic lithography [24], nanosphere lithography [25–28], and chemical wet etching [29–31]. In the present authors' previous study, a nanoscale patterned sapphire substrate was used to improve the light extraction efficiency of LEDs [32]. The same approach can be used to develop silicon-based devices such as solar cells and optical sensors. Therefore, nanoscale structures can be simply and effectively used to reduce Fresnel reflection from the silicon surface.

In this work, a uniform and periodic nanopattern silicon substrate (NPSiS) was fabricated by the self-assembly of a monolayer array of nanospheres, which was followed by inductively coupled plasma (ICP) dry etching to translate a 2D periodic pattern on the silicon wafer. The ICP etching time was tuned to fabricate NPSiS structures of four depths. Then, these variously textured wafers were used on Si-based heterojunction thin-film (HJT) solar cells, which were fabricated using a radiofrequency (RF) magnetron sputtering cluster system. The consequent improvement in NPSiS HJT solar cells was investigated.

2. Experimental

2.1. Reflectance Spectra Simulation. To obtain NPSiS with excellent antireflection properties, the size of the textured structure must be within the subwavelength range. Well-designed periodic nanostructures exhibit a gradually changing refractive index, which can be used to maximize the omnidirectional antireflection character of NPSiS over a wide range of wavelengths. In this work, NPSiS structures were simulated and the three-dimensional (3D) finite-difference time-domain (FDTD) method (Lumerical Solutions, Inc.) was used to optimize their period and geometry. The size of the nanostructures for use in silicon solar cells must be less than 850 nm. Based on the results of an NPSiS simulation, the period of the nanostructures was designed to be 550 nm with periodic boundaries. With the NPSiS period set, other NPSiS structural parameters—top width (TW), bottom width (BW), and etching depth (D)—were simulated. Plane waves with wavelengths of 350 nm to 950 nm were normally incident on the structures.

2.2. Patterning Silicon Wafer. Highly uniform subwavelength SiO₂ nanospheres were prepared using the modified Stober process and an alcohol-rich phase. Purified water, ammonium hydroxide, and pure alcohol were added to a sealed bottle that was purged with nitrogen. The contents were stirred to ensure that they were thoroughly mixed. Tetraethyl orthosilicate (TEOS) was then added to the system. After two hours of stirring, the latex was centrifuged to collect the 550 nm SiO₂ nanospheres, which were washed three times with pure alcohol to remove any remaining impurities.

Figure 1 shows the flow chart of the preparation of NPSiS. First, the silicon wafer was immersed in latex that comprised SiO₂ nanospheres with a diameter of 550 nm. Next, a monolayer of nanospheres was arrayed on the surface of the silicon by the dip-coating method. The silicon substrate was a CZ n-type c-Si (100) wafer with a base resistivity of 1–10 Ω·cm, and its thickness was about 325 μm. After the SiO₂ nanospheres were arrayed on the wafer, they were used as the etching mask in the ICP process in which the NPSiS was fabricated. The ICP process involved the well-mixed gases BCl₃, Cl₂, and Ar with a reactor pressure of 7.5 mTorr, a top electrode RF power of 300 W, a bottom electrode RF power of 116 W, and a bias voltage of 210 V.

2.3. Deposition of Thin Films. The first step in the fabrication of the p-type a-Si:H thin films and the deposition of the transparent conductive oxide (TCO) layer was RCA cleaning. The native oxide layer on the surface of the Si wafer was removed using diluted HF (2%) solution for 120 s before the p-type a-Si:H thin film was deposited. The p-type a-Si:H thin films and TCO layer were deposited using a radiofrequency (RF, 13.56 MHz) magnetron sputtering cluster system. In the deposition of the p-type a-Si:H thin films, the sputtering target was a p-type Si disc with a diameter of 3", and some boron (B) grains were placed on the p-type Si target to increase the doping; the area of boron was about 30% of the area of the plasma ring of the target.

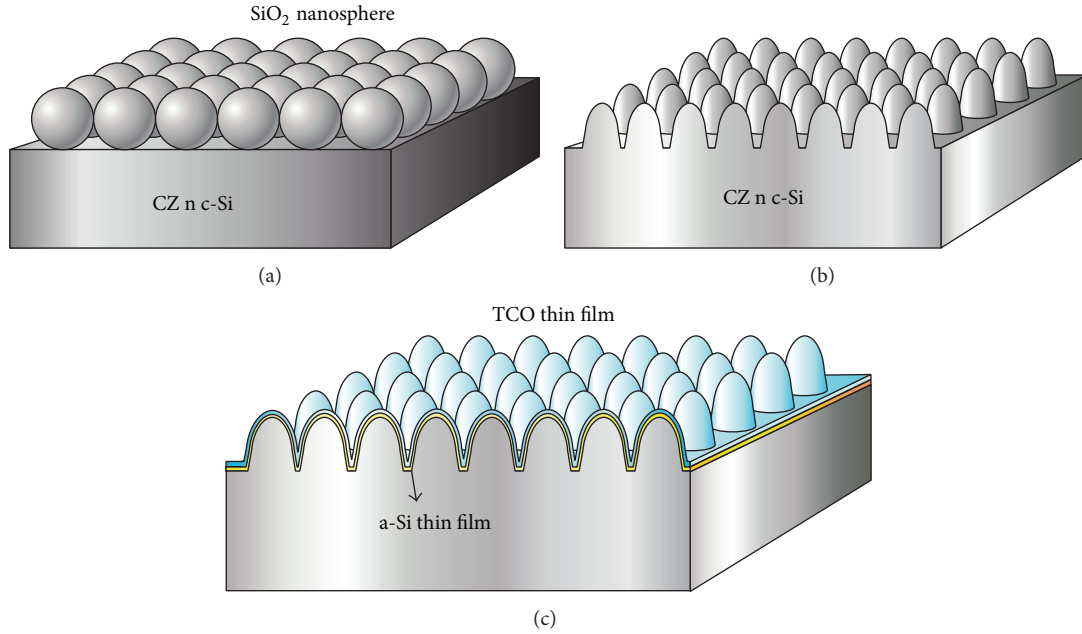


FIGURE 1: Flow chart of preparation of NPSiS HJT solar cells; (a) coating monolayer of SiO₂ nanospheres on CZ n-type c-Si substrate; (b) using SiO₂ nanospheres as etching mask in ICP process to fabricate NPSiS; (c) depositing the p-type a-Si : H thin films and TCO thin films by RF magnetron sputtering.

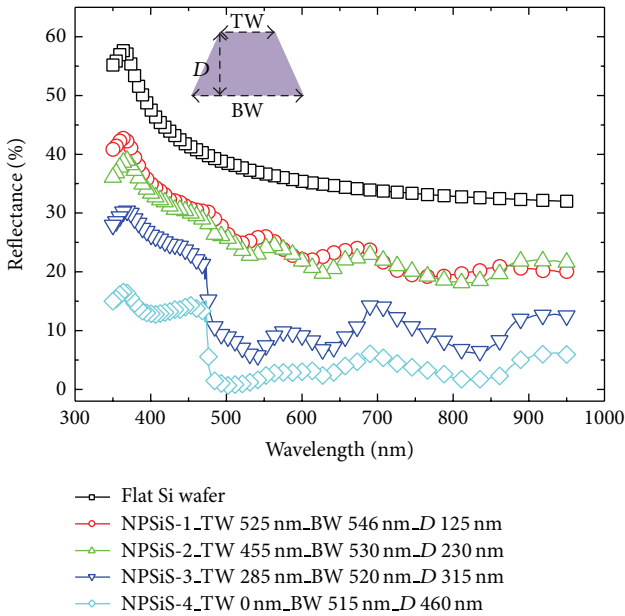


FIGURE 2: Using 3D-FDTD method to simulate reflectance spectra of periodic 550 nm NPSiS.

The p-type a-Si : H films were deposited at an RF power of 100 W under argon and hydrogen as working gases with a P_{H_2}/P_{Ar} partial pressure ratio set to three. The temperature of the chamber was 300 degrees Celsius. The base pressure and working pressure of the chamber were less than 5.0×10^{-6} torr and 2.1×10^{-3} torr, respectively. The thickness of the p-type a-Si : H thin film was 10 nm. Following the deposition of the

p-type a-Si : H thin films, the samples were moved to another chamber to deposit the TCO layer. During transportation, each sample was kept in a vacuum to prevent oxidation, which could have increased the number of defects in the silicon thin film. Indium tin oxide (ITO) films were used as the TCO layer. Two ITO layers were deposited on the p-type a-Si : H films; the first layer was an ITO : O₂ film that raised the work function to increase the V_{oc} of the silicon HJT solar cells. The thickness of the ITO : O₂ film that was deposited at an RF power of 100 W and a chamber temperature of 300 degrees Celsius was 20 nm. The working gases were argon, which flowed at 10 standard cubic centimeters per minute (SCCM), and oxygen, which flowed at 0.9 SCCM. Following the deposition of the ITO : O₂ film, the 80 nm thick ITO film without oxygen gas was deposited on the ITO : O₂ film. The two layers of ITO film increased the V_{oc} of the HJT cells and maintained favorable conductivity of the TCO layer [33, 34].

The last step of the fabrication of silicon HJT solar cells is coating both of the front (with a finger separation of 1.9 mm and a width 100 μ m) and rear metal electrodes with titanium (Ti) to a thickness of 20 nm and then aluminum (Al) to a thickness of 1~1.2 μ m using an e-gun evaporator. The performance of the solar cell thus formed was determined by making *I-V* measurements in the dark and under illumination (AM 1.5G condition, 100 mW/cm²).

3. Results and Discussion

3D-FDTD calculations were performed to simulate the optical behavior of the NPSiS wafer [35, 36]. Figure 2 shows the reflectance spectra of the flat silicon wafer and four NPSiS wafer. The curve through the black symbols represents

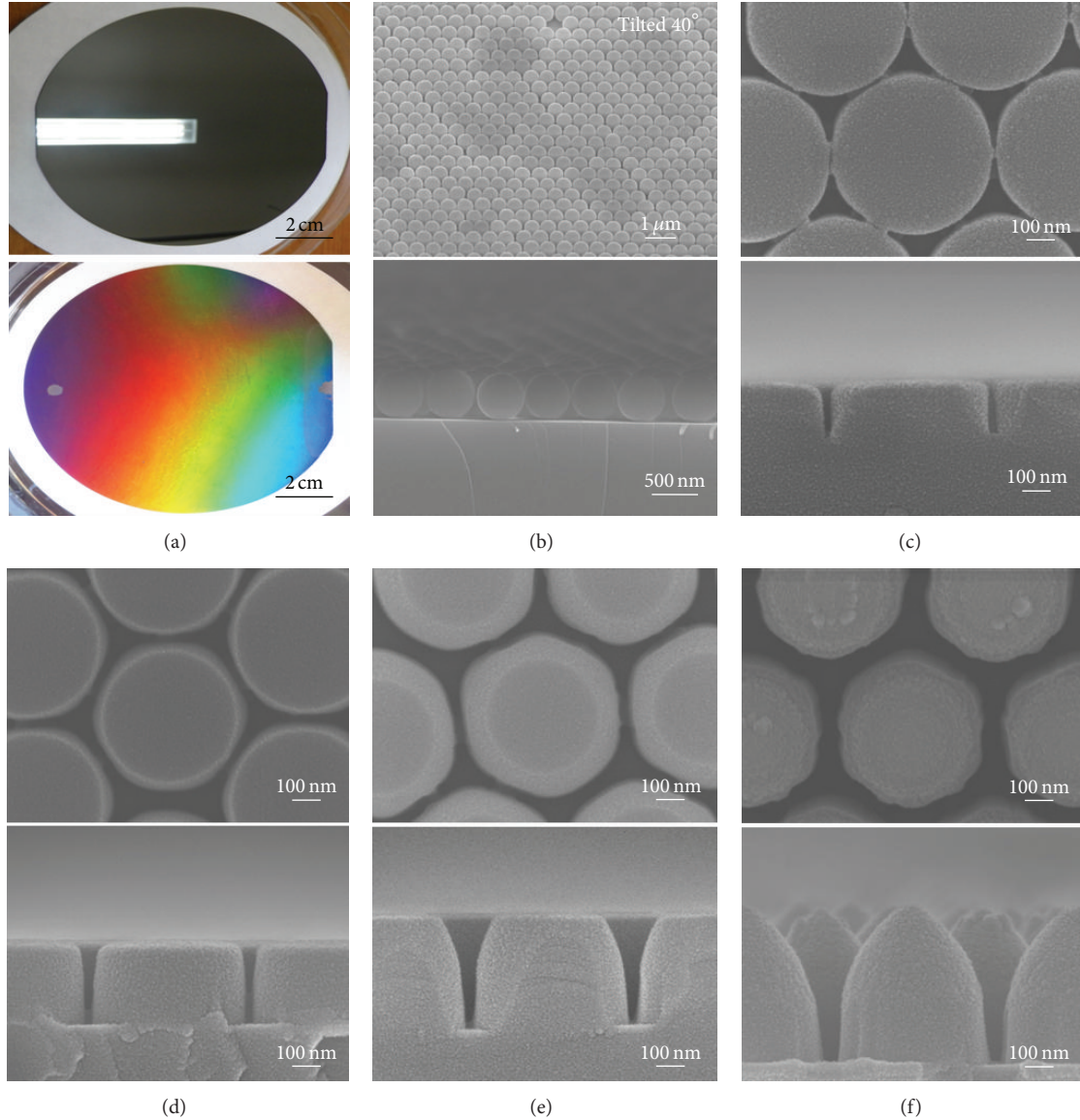


FIGURE 3: (a) Photograph of 4" bulk silicon wafer (top) and a monolayer array of 550 nm nanospheres that were deposited on a 4 inch silicon wafer (bottom). (b) Close view of a monolayer nanosphere on Si wafer; ((c)–(f)) NPSiS with different dry etching times: (c) NPSiS-1, 80 s (depth: 180 nm), (d) NPSiS-2, 150 s (depth: 270 nm), (e) NPSiS-3, 230 s (depth: 370 nm), and (f) NPSiS-4, 450 s (depth: 550 nm).

the simulated reflectance of the flat silicon wafer; the average reflectance at wavelengths from 350 nm to 950 nm is about 41%. The curves through the red, blue, pink, and green symbols plot the simulated reflectances of NPSiS-1, NPSiS-2, NPSiS-3, and NPSiS-4, which have average values of 28.42%, 26.99%, 16.41%, and 7.59%, respectively. The NPSiS-4 exhibits the best reduction of reflectance by the multireflection of the normally incident light.

The reflectance spectra that were obtained by the 3D-FDTD simulation demonstrate that the pointed NPSiS exhibited better antireflection properties than the frustum NPSiS. Since multireflection efficiently increased the absorption of light by the pointed NPSiS wafer, it reduced the reflectance. As the results of the simulation reveal, NPSiS with a deeper

frustum shape exhibited a stronger antireflection effect, revealing that the depth of the textured silicon structures affected its reflectance.

Based on the results of the simulation, the ICP dry etching recipes can be modified to fabricate various NPSiS wafer. Figure 3(a) presents the monolayer array of 550 nm nanospheres that were deposited on a 4 inch silicon substrate; the diffractive nature of the nanospheres is evident. The scanning electron microscopic (SEM) image in Figure 3(b) provides a close view of a monolayer of nanospheres, revealing their hexagonal arrangement; the side-view SEM image of the arrangement of nanospheres confirms the monolayer arrangement. Owing to the success of the aforementioned deposition process, the 550 nm nanospheres were used in the

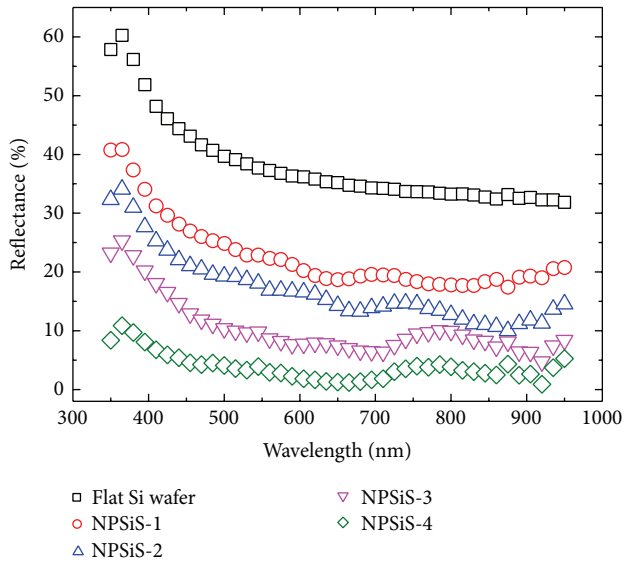


FIGURE 4: Reflectance spectra of flat c-Si wafer and NPSiS wafers obtained using integrated sphere system.

rest of this work. Figures 3(c) to 3(f) were obtained after etching times of 80 s (NPSiS-1), 150 s (NPSiS-2), 230 s (NPSiS-3), and 450 s (NPSiS-4), and the resulting depths of the four textured wafers were about 180 nm, 270 nm, 370 nm, and 550 nm, respectively. Gradually increasing the etching time reduced the diameter of the SiO₂ nanospheres and gradually reduced the top diameter of the frustum nanostructure until the nanosphere mask that had the shape of the NPSiS structure was overetched and so changed from a frustum shape to a bullet shape; its depth was limited to about 550 nm.

Figure 4 shows the reflectance spectra of flat c-Si wafer and NPSiS wafers that were obtained using the integrated sphere system with an angle of incidence of light of 8°, in a wavelength range from 350 nm to 950 nm. The curve through the black symbols reveals that the flat silicon wafer has an average reflectance of 37.96%; the curves through the red, blue, pink, and green symbols provide the measured reflectance results for NPSiS-1, NPSiS-2, NPSiS-3, and NPSiS-4, which have average reflectance values of 22.62%, 16.89%, 10.21%, and 3.64%, respectively. The measurements demonstrate that the total reflectance of NPSiS decreases as its depth increases, and the antireflective properties of all NPSiS wafers are evident not only in a particular range of wavelengths but also in the full range of wavelengths over which silicon absorbs region. The gradient of the refractive index of the nanostructure of the Si wafer surface can effectively reduce the Fresnel reflection of photons of short wavelengths (<550 nm). For long wavelength photons (>700 nm), the effective refractive index of the nanostructure as a porous layer between the Si wafer and air is a discontinuity of the refractive index, increasing the absorption of incident photons [37].

Figures 5(a) to 5(d) presented side-view SEM images of the NPSiS wafer following magnetron sputtering deposition. As shown in Figures 5(a)–5(d), the low step coverage that was

achieved using the sputter coating process yielded different thicknesses of the covering ITO thin films on the top and side of the nanostructure. However, even though the step coverage that was achieved by sputtering is not very uniform, the ITO films and the p-type a-Si film both nevertheless formed a continuous layer, as shown in Figures 5(a)–5(d). Moreover, the nonuniform ITO films formed a layer with a gradient in the refractive index, which enhanced the antireflection effect of the NPSiS cells, as presented in Figure 5(e).

To discuss the omnidirectional antireflection effect, the angle-resolved integrated sphere system was used to measure the average reflectance of NPSiS wafers in HJT cells when light was incident at various angles. Figures 6(a) and 6(b) show the average reflectance that was achieved with light at angles of incidence from 8° to 60°. The reflectance of NPSiS-4 wafers was less than 12% for all angles of incidence, and the NPSiS-4 HJT cell devices exhibited the strongest omnidirectional antireflection effect of all NPSiS HJT cells, with a reflectance of less than 6% for all angles of incidence at wavelengths between 350 nm and 950 nm. The above results demonstrate that the depth of NPSiS was 550 nm and the profile became bullet-shaped, and then its reflectance was nearly omnidirectional. Figure 6(c) presents a photograph of the reference HJT cell and the NPSiS HJT cells. As the depth of NPSiS increased, the outward appearance of the NPSiS HJT cell became more like that of a dark solar cell.

To analyze further the optical properties of NPSiS HJT cells, Figure 5(e) shows the reflectance spectra of NPSiS HJT cells and a nontextured HJT cell when light at wavelengths between 350 nm and 950 nm was normally incident. The curve through the black symbols reveals that the nontextured HJT cell had an average reflectance of 14.80%. The curves through the red, blue, pink, and green symbols represent the measured reflectances of the NPSiS-1, NPSiS-2, NPSiS-3, and NPSiS-4 HJT cells, which had average reflectance values of 10.75%, 9.28%, 6.18%, and 2.04%, respectively. The purple dashed curve represents the reflectance of the 100 nm thick ITO layer on a glass substrate (B270). Based on the conductivity and work function of the TCO layer, the antireflection wavelength of the TCO layer on the silicon wafer was designed to be about 780 nm, and its average absorption was about 3.4% at wavelengths from 350 nm to 950 nm. In this TCO design, the reflectance of the nontextured silicon HJT cells exhibited a peak at a wavelength close to 500 nm, at which wavelength the external quantum efficiency (EQE) of nontextured silicon HJT cell was reduced, as shown in Figure 7(c). However, the designed TCO layer increased the transmittance of incident light, increasing the EQE of the nontextured HJT cell to 75.5% at a wavelength of 400 nm.

To investigate the electrical properties of HJT solar cells, the EQE, dark current-voltage (*I-V*), and illuminated *I-V* properties under a simulated AM1.5G condition at room temperature were measured. The EQE measurements yield the photon conversion efficiency of HJT cells at wavelengths from 300 nm to 1100 nm in steps of 10 nm; the dark *I-V* results are related to the characteristics of the interface between the p-type a-Si:H thin films and the n-type c-Si substrates in the HJT cells, and the illuminated *I-V* measurements yield

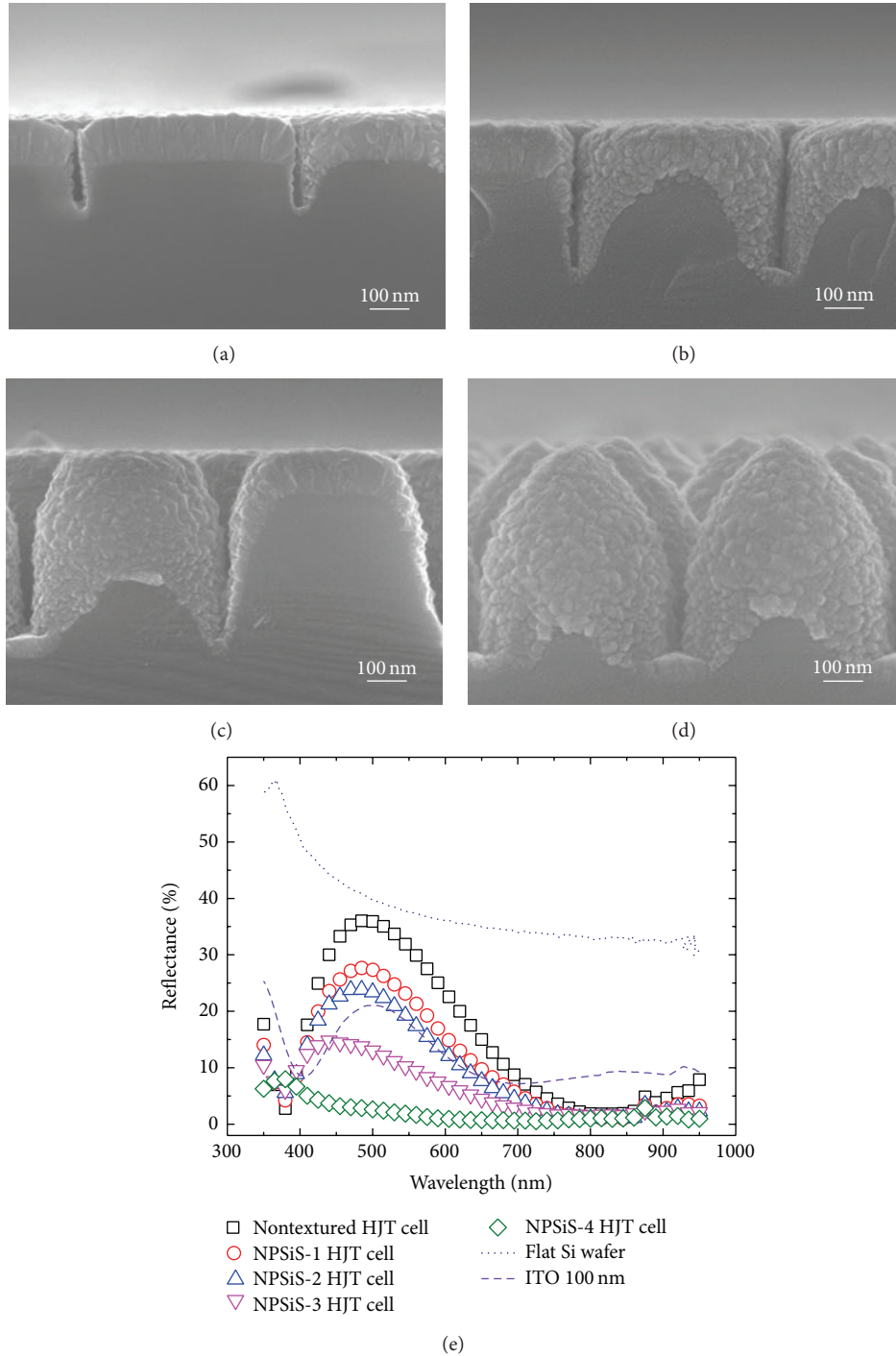


FIGURE 5: Side-view SEM images of NPSiS wafer following magnetron sputtering deposition on four NPSiS wafers. (a) NPSiS-1 HJT cell, (b) NPSiS-2 HJT cell, (c) NPSiS-3 HJT cell, (d) NPSiS-4 HJT cell, and (e) reflectance spectra of NPSiS HJT cells and nontextured HJT cell.

the V_{oc} , short current density (J_{sc}), fill-factor (FF), and power conversion efficiency of the HJT solar cells.

Figure 5(e) reveals that deeper NPSiS (1–4) HJT cells have a lower reflectance at a wavelength of 500 nm, so the J_{sc} values that are calculated from the measured EQE vary from 26.65 mA/cm² for the nontextured HJT cell to 30.81 mA/cm² for the NPSiS-1 HJT cell, 31.40 mA/cm² for the NPSiS-2 HJT cell, 33.08 mA/cm² for the NPSiS-3 HJT cell,

and 35.22 mA/cm² for the NPSiS4 HJT cell, as presented in Figure 7(c). These results demonstrate that the four NPSiS HJT cells exhibit differently enhanced EQE; in particular, in the NPSiS-4 HJT, the region of reduced EQE was completely repaired owing to the TCO layer, and its J_{sc} reached 35.22 mA/cm².

Figure 7(a) plots the measured dark I - V results that were obtained with injected voltages from -0.8 V to $+0.8$ V. The

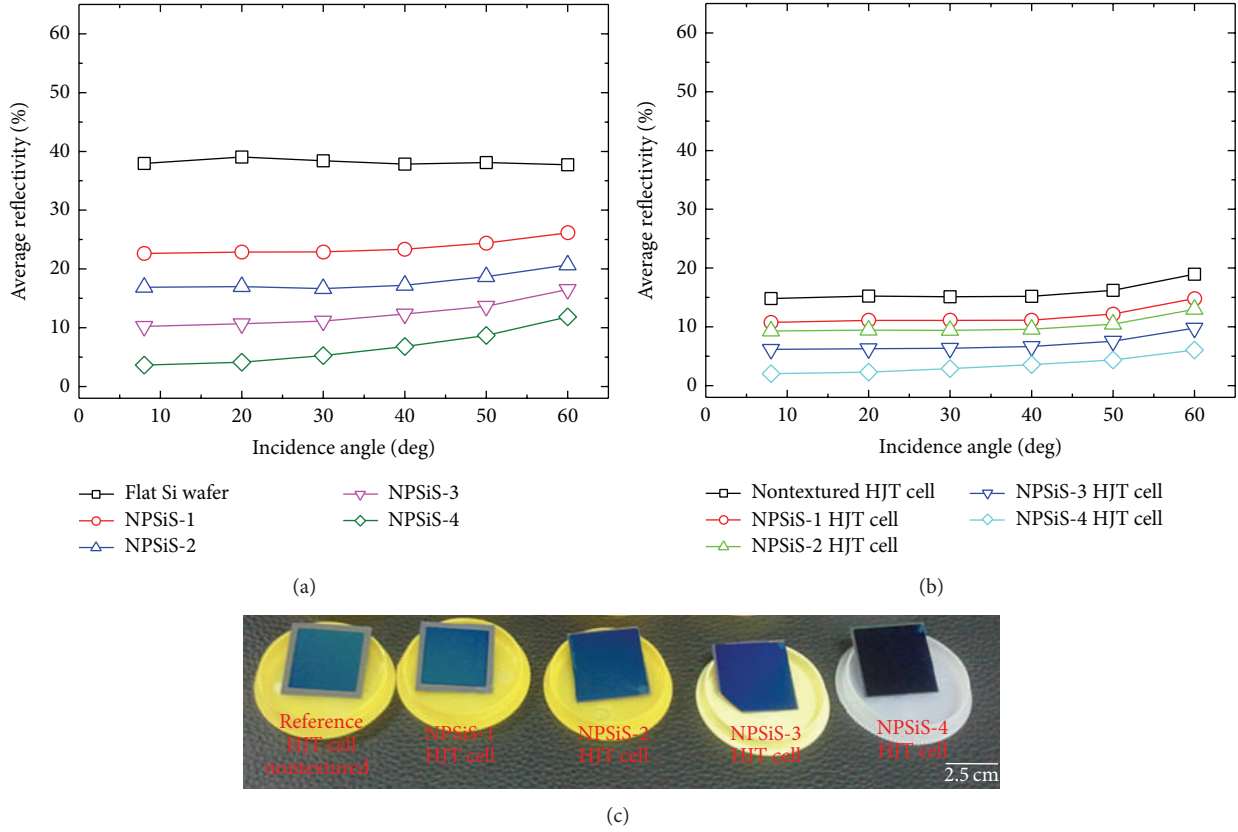


FIGURE 6: Average reflectance results achieved with light at angles of incidence from 8 degrees to 60 degrees at wavelengths between 350 nm and 950 nm; (a) flat Si wafer and NPSiS wafer, (b) nontextured HJT cell and four NPSiS HJT cells, and (c) photograph of reference HJT cell and NPSiS HJT cells.

TABLE 1: I - V characteristics of four NPSiS HJT cells and nontextured reference HJT cell.

	Reflectance at 500 nm (%)	Designated areas (cm^2)	V_{oc} (mV)	J_{sc} (mA/cm^2)	FF (%)	Eff (%)	Enhancement (%)	R_s ($\Omega\text{-cm}^2$)
Nontextured	35.91	0.76	537.69	28.80	56.30	8.67	—	9.61
NPSiS-1	27.33	0.68	461.84	31.42	68.90	9.99	15.22	3.08
NPSiS-2	23.38	0.76	434.89	32.26	65.00	9.12	5.19	3.07
NPSiS-3	12.99	0.79	442.96	33.70	66.50	9.93	14.53	2.54
NPSiS-4	2.64	0.71	481.94	36.20	65.20	11.40	31.49	2.68

left-most curve in Figure 7(a) shows that the leakage currents of NPSiS HJT cells of various depths all exceeded those of the nontextured HJT cell. The right-hand side of Figure 7(a) reveals that generation-recombination currents of the four NPSiS HJT cells at less than the threshold voltage all exceeded those of the nontextured HJT cell, implying that the junctions in the four NPSiS HJT cells contained more defects than those of the nontextured cell [38].

The above results follow mostly from the fact that the ICP dry etching process damages the NPSiS surface, so more defects are generated in that surface than in the surface of the nontextured Si wafer. Figure 7(b) compares the illuminated I - V characteristics of HJT solar cells with an NPSiS wafer with those of a cell with a flat silicon wafer. Table 1 also summarizes these characteristics. In Figure 7(b), the J_{sc} of the NPSiS-4

HJT cell is $36.20 \text{ mA}/\text{cm}^2$, and its efficiency is 11.4%, which is 31.49% greater than that, 8.67%, of the nontextured HJT cell (Table 1). This result is consistent with the reflectance that was obtained using the integrating sphere system (Figures 5(a) and 5(b)), indicating that the lower reflectance of NPSiS is associated with the absorption of more photons, so the NPSiS HJT cells have a higher J_{sc} .

All NPSiS HJT cells exhibited an improved FF, because NPSiS increased the surface contact areas (as presented in Figure 8), reducing the resistivity of the HJT cells, causing the series resistivity of all the NPSiS-HJT cells to be lower than that of the nontextured HJT cell and the FF of the NPSiS-HJT cells to be higher. However, the FF of NPSiS cannot grow steadily with the surface area being increased, because the dry etching processes damage the surface of the NPSiS

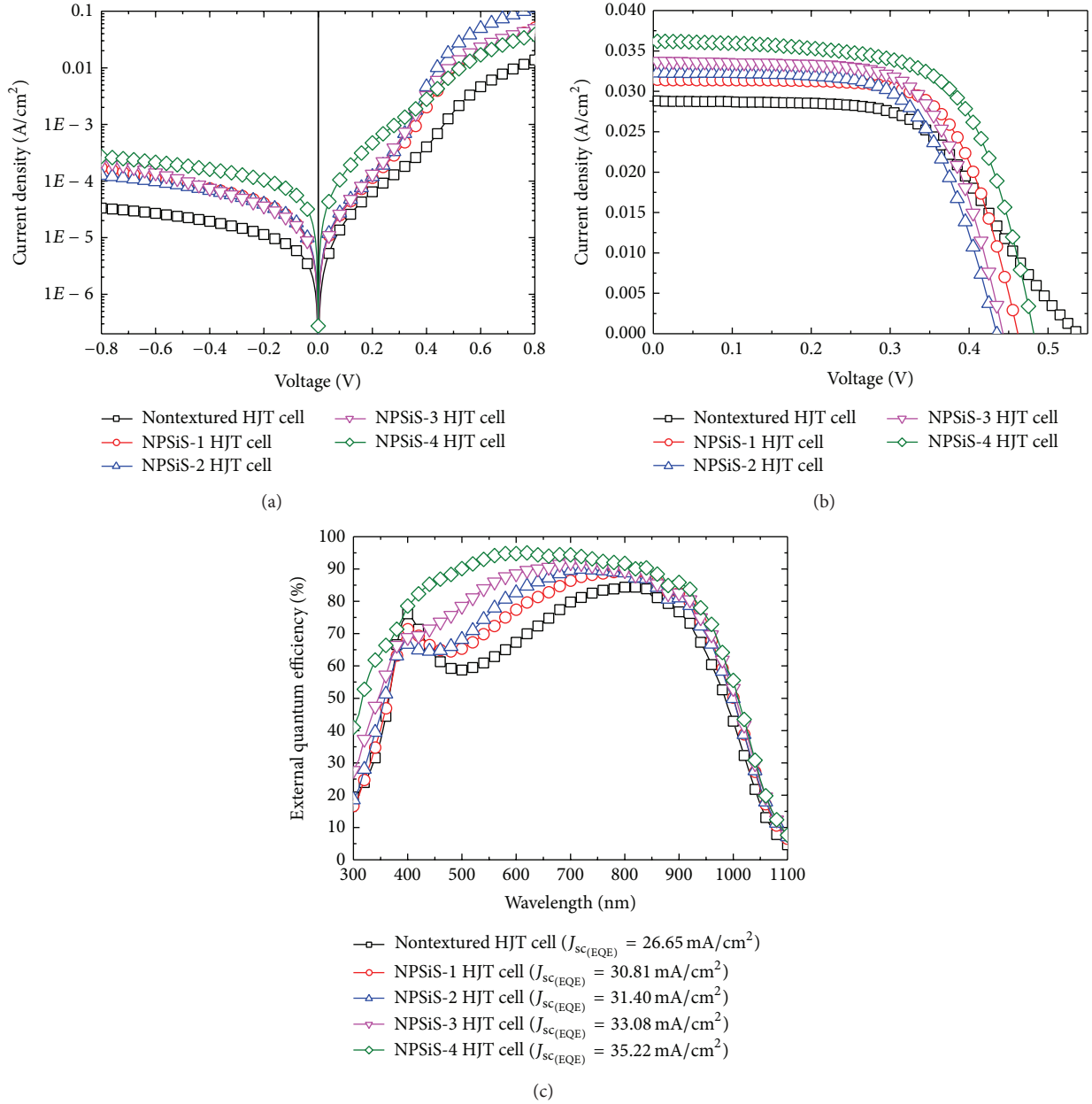


FIGURE 7: Measured $I-V$ curves of four NPSiS-HJT cells and nontextured HJT cell: (a) dark $I-V$, (b) illuminated $I-V$ (AM 1.5G condition), and (c) corresponding external quantum efficiency (EQE) characteristics.

wafer, generating more defects on its surface, increasing the leakage current of the cell, and reducing the shunt resistivity. The V_{oc} values of all of the NPSiS HJT cells were therefore reduced to different degrees. This phenomenon will be investigated by treating the plasma-damaged surfaces using various methods.

4. Conclusion

In this work, RF magnetron sputtering was performed to fabricate silicon HJT solar cells. In the sputtering deposition process, p-type a-Si:H films were sputtered with added

boron grains on the p-type c-Si target to increase the amount of dopant boron atoms in the thin films. Then, the ITO/p-type a-Si:H/n-type c-Si structure was fabricated for use in HJT solar cells, and its characteristics were measured. The V_{oc} , J_{sc} , FF, and power conversion efficiency of the reference Si-based HJT solar cells were 537 mV, 28.8 mA/cm², 56.3%, and 8.67%, respectively.

NPSiS wafer was demonstrated effectively to improve the power conversion efficiency of HJT cells. The NPSiS-4 HJT cell efficiency was 11.4%, representing an enhancement of 31.49% relative to that, 8.67%, of the flat silicon HJT cell. This enhancement arose from the improvement in J_{sc} , which

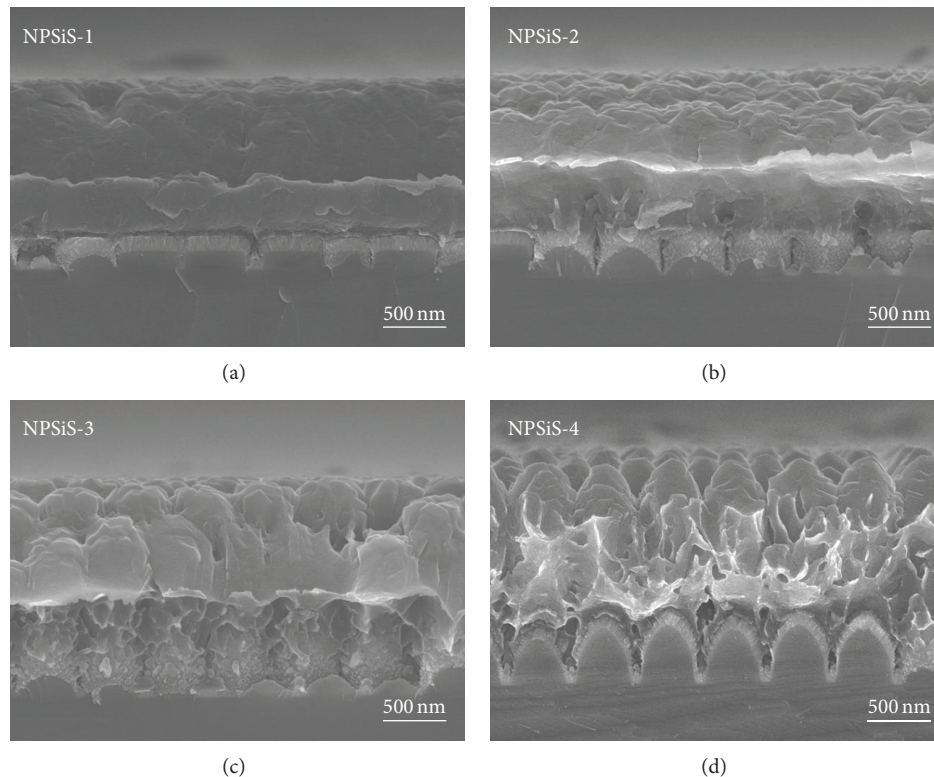


FIGURE 8: SEM images of metal contacts of four NPSiS HJT cells: (a) NPSiS-1 HJT cell, (b) NPSiS-2 HJT cell, (c) NPSiS-3 HJT cell, and (d) NPSiS-4 HJT cell.

increased the absorption of incident light on the surface of the NPSiS wafer, and from the improvement in FF by the increase in the surface area of the silicon, which reduced the series resistance of the NPSiS HJT cells. The dry etching process reduced the V_{oc} of the NPSiS HJT solar cells. A further investigation must be undertaken to solve this problem. Based on the above results, NPSiS that is patterned using nanospheres lithography in the sputtering deposition process can be used in the low-cost fabrication of Si-based HJT solar cells.

Conflict of Interests

The authors declare that there is no conflict of interests regarding the publication of this paper.

Acknowledgment

The authors would like to thank the National Science Council of Taiwan, Taiwan, for financially supporting this research under Contract no. NSC101-2221-E-008-027-MY2.

References

- [1] D. L. Staebler and C. R. Wronski, "Reversible conductivity changes in discharge-produced amorphous Si," *Applied Physics Letters*, vol. 31, no. 4, pp. 292–294, 1977.
- [2] M. Tanaka, M. Taguchi, T. Matsuyama et al., "Development of new a-Si/c-Si heterojunction solar cells: ACJ-HIT (Artificially Constructed Junction-Heterojunction with Intrinsic Thin-layer)," *Japanese Journal of Applied Physics 1: Regular Papers and Short Notes and Review Papers*, vol. 31, no. 11, pp. 3518–3522, 1992.
- [3] M. Tanaka, S. Okamoto, S. Tsuge, and S. Kiyama, "Development of HIT solar cells with more than 21% conversion efficiency and commercialization of highest performance hit modules," in *Proceedings of the 3rd World Conference on Photovoltaic Energy Conversion*, pp. 955–958, Osaka, Japan, May 2003.
- [4] M. Taguchi, A. Yano, S. Tohoda et al., "24.7% record efficiency HIT solar cell on thin silicon wafer," *Journal of Photovoltaics*, vol. 4, no. 1, pp. 96–99, 2014.
- [5] B. Jagannathan, W. A. Anderson, and J. Coleman, "Amorphous silicon/p-type crystalline silicon heterojunction solar cells," *Solar Energy Materials and Solar Cells*, vol. 46, no. 4, pp. 289–310, 1997.
- [6] K.-S. Ji, J. Choi, H. Yang, H.-M. Lee, and D. Kim, "A study of crystallinity in amorphous Si thin films for silicon heterojunction solar cells," *Solar Energy Materials and Solar Cells*, vol. 95, no. 1, pp. 203–206, 2011.
- [7] H. Angermann, E. Conrad, L. Korte, J. Rappich, T. F. Schulze, and M. Schmidt, "Passivation of textured substrates for a-Si:H/c-Si hetero-junction solar cells: Effect of wet-chemical smoothing and intrinsic a-Si:H interlayer," *Materials Science and Engineering B: Solid-State Materials for Advanced Technology*, vol. 159-160, pp. 219–223, 2009.
- [8] M. Gharghi, E. Fathi, B. Kante, S. Sivoththaman, and X. Zhang, "Heterojunction silicon microwire solar cells," *Nano Letters*, vol. 12, no. 12, pp. 6278–6282, 2012.

- [9] Y. Ohmura, M. Takahashi, M. Suzuki, N. Sakamoto, and T. Meguro, "P-type doping of hydrogenated amorphous silicon films with boron by reactive radio-frequency co-sputtering," *Physica B: Condensed Matter*, vol. 308-310, pp. 257–260, 2001.
- [10] M. M. De Lima Jr., F. L. Freire Jr., and F. C. Marques, "Boron doping of hydrogenated amorphous silicon prepared by rf-co-sputtering," *Brazilian Journal of Physics*, vol. 32, no. 2, pp. 379–382, 2002.
- [11] J.-Q. Xi, M. F. Schubert, J. K. Kim et al., "Optical thin-film materials with low refractive index for broadband elimination of Fresnel reflection," *Nature Photonics*, vol. 1, no. 3, pp. 176–179, 2007.
- [12] G. Crotty, T. Daud, and R. Kachare, "Front surface passivation of silicon solar cells with antireflection coating," *Journal of Applied Physics*, vol. 61, no. 8, pp. 3077–3079, 1987.
- [13] H.-W. Huang, J. T. Chu, C. C. Kao et al., "Enhanced light output of an InGaN/GaN light emitting diode with a nano-roughened p-GaN surface," *Nanotechnology*, vol. 16, no. 9, pp. 1844–1848, 2005.
- [14] W.-C. Lee, S.-J. Wang, K.-M. Uang et al., "Enhanced light output of GaN-based vertical-structured light-emitting diodes with two-step surface roughening using KrF laser and chemical wet etching," *IEEE Photonics Technology Letters*, vol. 22, no. 17, pp. 1318–1320, 2010.
- [15] D. Liang, Y. S. Kang, Y. Huo, Y. Chen, Y. Cui, and J. S. Harris, "High-efficiency nanostructured window GaAs solar cells," *Nano Letters*, vol. 13, no. 10, pp. 4850–4856, 2013.
- [16] K.-Q. Peng, X. Wang, L. Li, X.-L. Wu, and S.-T. Lee, "High-performance silicon nanohole solar cells," *Journal of the American Chemical Society*, vol. 132, no. 20, pp. 6872–6873, 2010.
- [17] E. Garnett and P. Yang, "Light trapping in silicon nanowire solar cells," *Nano Letters*, vol. 10, no. 3, pp. 1082–1087, 2010.
- [18] L. Cao, P. Fan, A. P. Vasudev et al., "Semiconductor nanowire optical antenna solar absorbers," *Nano Letters*, vol. 10, no. 2, pp. 439–445, 2010.
- [19] S. Jeong, E. C. Garnett, S. Wang et al., "Hybrid silicon nanocone-polymer solar cells," *Nano Letters*, vol. 12, no. 6, pp. 2971–2976, 2012.
- [20] Y. Kanamori, M. Sasaki, and K. Hane, "Broadband antireflection gratings fabricated upon silicon substrates," *Optics Letters*, vol. 24, no. 20, pp. 1422–1424, 1999.
- [21] M. Iwaya, H. Kasugai, T. Kawashima et al., "Improvement in light extraction efficiency in group III nitride-based light-emitting diodes using moth-eye structure," *Thin Solid Films*, vol. 515, no. 2, pp. 768–770, 2006.
- [22] H. Hlaing, X. Lu, T. Hofmann, K. G. Yager, C. T. Black, and B. M. Ocko, "Nanoimprint-induced molecular orientation in semiconducting polymer nanostructures," *ACS Nano*, vol. 5, no. 9, pp. 7532–7538, 2011.
- [23] Y. Yang, K. Mielczarek, M. Aryal, A. Zakhidov, and W. Hu, "Nanoimprinted polymer solar cell," *ACS Nano*, vol. 6, no. 4, pp. 2877–2892, 2012.
- [24] K. Hadobás, S. Kirsch, A. Carl, M. Acet, and E. F. Wassermann, "Reflection properties of nanostructure-arrayed silicon surfaces," *Nanotechnology*, vol. 11, no. 3, pp. 161–164, 2000.
- [25] C.-H. Sun, P. Jiang, and B. Jiang, "Broadband moth-eye antireflection coatings on silicon," *Applied Physics Letters*, vol. 92, no. 6, Article ID 061112, pp. 061112–061113, 2008.
- [26] T. Nakanishi, T. Hiraoka, A. Fujimoto, S. Saito, and K. Asakawa, "Nano-patterning using an embedded particle monolayer as an etch mask," *Microelectronic Engineering*, vol. 83, no. 4–9, pp. 1503–1508, 2006.
- [27] S.-Y. Chuang, H.-L. Chen, J. Shieh et al., "Nanoscale of biomimetic moth eye structures exhibiting inverse polarization phenomena at the Brewster angle," *Nanoscale*, vol. 2, no. 5, pp. 799–805, 2010.
- [28] C.-H. Chan, C.-H. Hou, C.-K. Huang et al., "Patterning periodic motif on substrates using monolayer of microspheres: application in GaN light-emitting diodes," *Japanese Journal of Applied Physics*, vol. 48, no. 2, Article ID 020212, 2009.
- [29] J.-Y. Jung, Z. Guo, S.-W. Jee, H.-D. Um, K.-T. Park, and J.-H. Lee, "A strong antireflective solar cell prepared by tapering silicon nanowires," *Optics Express*, vol. 18, no. 19, pp. A286–A292, 2010.
- [30] K. Kim, S. K. Dhungel, S. Jung, D. Mangalaraj, and J. Yi, "Texturing of large area multi-crystalline silicon wafers through different chemical approaches for solar cell fabrication," *Solar Energy Materials and Solar Cells*, vol. 92, no. 8, pp. 960–968, 2008.
- [31] H. Angermann, W. Henrion, M. Rebien, and A. Röseler, "Wet-chemical passivation and characterization of silicon interfaces for solar cell applications," *Solar Energy Materials and Solar Cells*, vol. 83, no. 4, pp. 331–346, 2004.
- [32] C.-H. Chan, C.-H. Hou, S.-Z. Tseng et al., "Improved output power of GaN-based light-emitting diodes grown on a nanopatterned sapphire substrate," *Applied Physics Letters*, vol. 95, no. 1, Article ID 011110, 2009.
- [33] E. Centurioni and D. Iencinella, "Role of front contact work function on amorphous silicon/crystalline silicon heterojunction solar cell performance," *IEEE Electron Device Letters*, vol. 24, no. 3, pp. 177–179, 2003.
- [34] L. Zhao, C. L. Zhou, H. L. Li, H. W. Diao, and W. J. Wang, "Role of the work function of transparent conductive oxide on the performance of amorphous/crystalline silicon heterojunction solar cells studied by computer simulation," *Physica Status Solidi A*, vol. 205, no. 5, pp. 1215–1221, 2008.
- [35] H. L. Chen, S. Y. Chuang, C. H. Lin, and Y. H. Lin, "Using colloidal lithography to fabricate and optimize sub-wavelength pyramidal and honeycomb structures in solar cells," *Optics Express*, vol. 15, no. 22, pp. 14793–14803, 2007.
- [36] C.-H. Sun, P. Jiang, and B. Jiang, "Broadband moth-eye antireflection coatings on silicon," *Applied Physics Letters*, vol. 92, no. 6, Article ID 061112, 2008.
- [37] H. Sai, H. Fujii, K. Arafune et al., "Antireflective subwavelength structures on crystalline Si fabricated using directly formed anodic porous alumina masks," *Applied Physics Letters*, vol. 88, no. 20, Article ID 201116, 2006.
- [38] S.-K. Kim, J. C. Lee, S.-J. Park, Y.-J. Kim, and K. H. Yoon, "Effect of hydrogen dilution on intrinsic a-Si:H layer between emitter and Si wafer in silicon heterojunction solar cell," *Solar Energy Materials and Solar Cells*, vol. 92, no. 3, pp. 298–301, 2008.

Research Article

Doped Heterojunction Used in Quantum Dot Sensitized Solar Cell

Yanyan Gao, Xiaoping Zou, and Zongbo Huang

Beijing Key Laboratory for Sensor, School of Applied Sciences, Beijing Information Science and Technology University, Jianxiangqiao Campus, Beijing 100101, China

Correspondence should be addressed to Xiaoping Zou; xpzou2005@gmail.com

Received 19 February 2014; Revised 13 May 2014; Accepted 26 May 2014; Published 9 June 2014

Academic Editor: Dewei Zhao

Copyright © 2014 Yanyan Gao et al. This is an open access article distributed under the Creative Commons Attribution License, which permits unrestricted use, distribution, and reproduction in any medium, provided the original work is properly cited.

Incorporated foreign atoms into the quantum dots (QDs) used in heterojunction have always been a challenge for solar energy conversion. A foreign atom indium atom was incorporated into PbS/CdS QDs to prepare In-PbS/In-CdS heterojunction by successive ionic layer adsorption and reaction method which is a chemical method. Experimental results indicate that PbS or CdS has been doped with In by SILAR method; the concentration of PbS and CdS which was doped In atoms has no significantly increase or decrease. In addition, incorporating of Indium atoms has resulted in the lattice distortions or changes of PbS or CdS and improved the light harvest of heterojunction. Using this heterojunction, Pt counter electrode and polysulfide electrolyte, to fabricate quantum dot sensitized solar cells, the short circuit current density ballooned to 27.01 mA/cm^2 from 13.61 mA/cm^2 and the open circuit voltage was improved to 0.43 V from 0.37 V at the same time.

1. Introduction

Doped quantum dot (QDs, semiconductor nanocrystal) which was fabricated by chemical method has been recently drawing great attention as a material for solar energy conversion. Incorporating foreign atoms can affect intrinsic property of semiconductor nanocrystals [1, 2]. By doping foreign atom, it is possible to modify the electronic and photophysical properties of QDs [3]. In addition, it is also possible to tune the optical and electronic properties of semiconductor nanocrystals by controlling the type and concentration of dopants [4]. The versatile properties of doped QDs such as red-shift of light harvest [5], create of electronic states in the mid-gap region of the QD [6], and long time of an electron [7] make them attractive candidates for quantum dot sensitized solar cell (QDSC).

The doped single QDs have been researched. But incorporating foreign atoms into the quantum dot used in heterojunction has always been a challenge for solar energy conversion. In addition, one of the current challenges for high performance QDSC is the limited light absorption range from the visible to the near-infrared (NIR) region for the solar spectrum, so wider light absorption range has

ability to generate extremely high J_{sc} [8]. Recently, the light absorption range red shifts to 1100 nm from 900 nm when PbS quantum dot was doped as Hg-PbS quantum dot, resulting in the short circuit current density (J_{sc}) remarkable increase. Although the J_{sc} have a remarkable increase, the open circuit voltage (V_{oc}) has no significant change [9]. While the V_{oc} was increased when CdS/CdSe were doped as Mn-CdS/CdSe, the J_{sc} has no significant change [10]. How to improve the J_{sc} and the V_{oc} of QDSC is always a goal that many investigators pursue.

We introduced foreign atoms—indium atoms into PbS/CdS heterojunction [11–13] on the TiO_2 film by successive ionic layer adsorption and reaction (SILAR) method [14]; SILAR method is a chemical method. The indium was doped in both the PbS and CdS, characterization of the sample display that incorporating of Indium atoms would enhance absorption in the near-infrared portion. Using Pt counter electrode and polysulfide electrolyte to fabricate QDSC, the J_{sc} ballooned to 27.01 mA/cm^2 from 13.61 mA/cm^2 and the V_{oc} was improved to 0.43 V from 0.37 V at the same time. Relative to other heterojunction cells [15, 16], we used the easier way to prepare doped heterojunction.

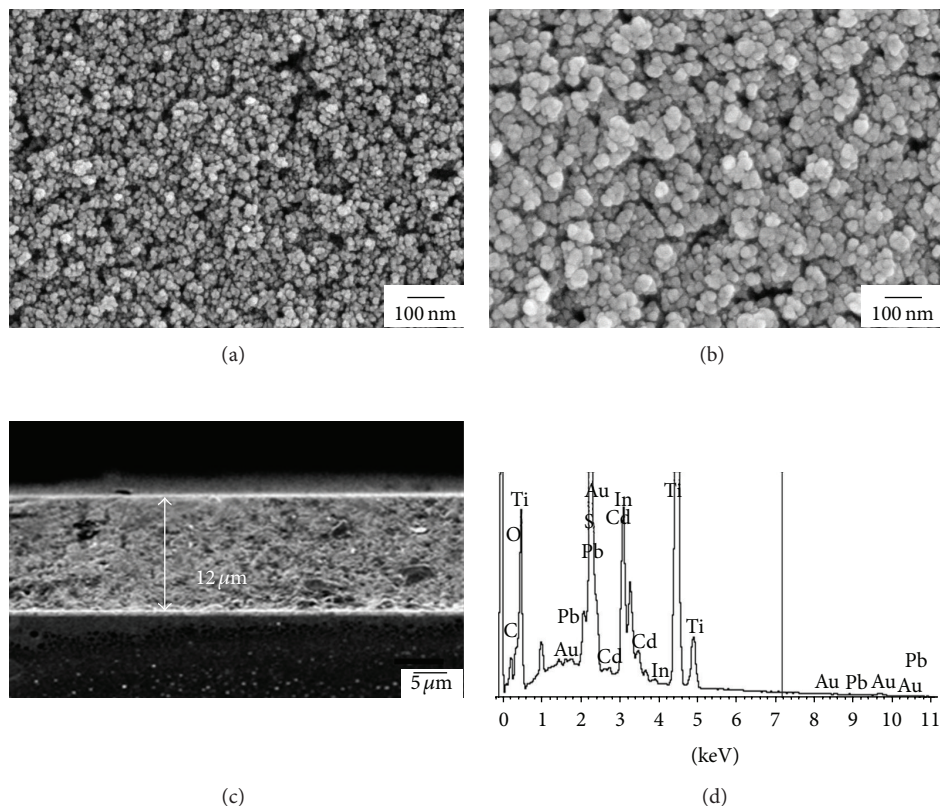


FIGURE 1: SEM image of (a) a bare TiO_2 mesoporous film and (b) In-PbS/In-CdS sensitized TiO_2 mesoporous film; (c) a cross-section SEM image of a bare TiO_2 film; (d) the EDX spectra of In-PbS/In-CdS QD sensitized TiO_2 film.

2. Experimental Procedure

The photoanode structure was FTO/ TiO_2 /QDs; mesoporous TiO_2 films were prepared by screen-printing of TiO_2 paste (the size of TiO_2 particle is about 20 nm) on clear fluorine-doped tin oxide (FTO) substrates, followed by sintering at 450°C for 30 min.

Quantum dots were deposited by successive ionic layer adsorption and reaction (SILAR) method. In brief, 0.1 M lead nitrate or cadmium nitrate in methanol was used as cation source and 0.1 M sodium sulfide in methanol as anion source. To incorporate doping of In^{3+} , indium chloride (0.01 M) was mixed with lead nitrate or cadmium nitrate. This allowed coadsorption of In^{3+} and Pb^{2+} (or Cd^{2+}) ions, which in turn facilitated incorporation of In^{3+} in the PbS (or CdS). The dipping time in the Pb^{2+} and S^{2-} solution was 60 s for each, and the SILAR cycle was repeated 2 times; the dipping time in the Cd^{2+} and S^{2-} solution was 5 min for each, and the SILAR cycle was repeated 6 times.

The counter electrode was Pt coated FTO, which was prepared by doctor blading chloroplatinic acid on FTO glass, then sintering at 450°C for 30 min. A solution of 0.5 M sodium sulfide, 2 M sulfur, and 0.2 M potassium chloride dissolved in 1:1 methanol and water was used as the liquid electrolyte. The cells were assembled in sandwich fashion using a parafilm spacer. Solar cell performance was evaluated under simulated AM1.5 irradiation conditions.

3. Results and Discussion

We prepared four different heterojunction types on TiO_2 film: (a) 2 SILAR cycles of PbS followed by 6 cycles of CdS ($\text{TiO}_2/\text{PbS}/\text{CdS}$), (b) 2 SILAR cycles of In-PbS followed by 6 cycles of CdS ($\text{TiO}_2/\text{In-PbS}/\text{CdS}$), (c) 2 SILAR cycles of PbS followed by 6 cycles of In-CdS ($\text{TiO}_2/\text{PbS}/\text{In-CdS}$), and (d) 2 SILAR cycles of In-PbS followed by 6 cycles of In-CdS ($\text{TiO}_2/\text{In-PbS}/\text{In-CdS}$). Figure 1(a) shows scanning electron micrograph (SEM) of a bare TiO_2 mesoporous film. It is clear that the particle size of TiO_2 ranges from 20 nm to 40 nm. When In-PbS and In-CdS were assembled in the TiO_2 film, a cluster of quantum dots in the surface was observed from the SEM images. This result indicates that a tiny amount of In-PbS and In-CdS was assembled in the SILAR process. A cross section SEM image of a bare TiO_2 mesoporous film is shown in Figure 1(c), in which the TiO_2 film thickness was clearly evident. Figure 1(d) presents energy dispersive X-ray spectroscopy (EDX) results obtained from $\text{TiO}_2/\text{In-PbS}/\text{In-CdS}$; EDX demonstrates the existence of In element in PbS or CdS. The actual Pb, Cd, and In concentration as measured from the inductively coupled plasma optical emission spectroscopy, ICP-OES, analysis was found to be 7.383%, 45.5%, and 0.97% in In-PbS/CdS QDs; 8.8143%, 47.86%, and 5.48% in PbS/In-CdS QDs; and 6.49%, 49.62%, and 5.49% in In-PbS/In-CdS QDs. This indicates the incorporation of Indium into PbS and CdS quantum dots by

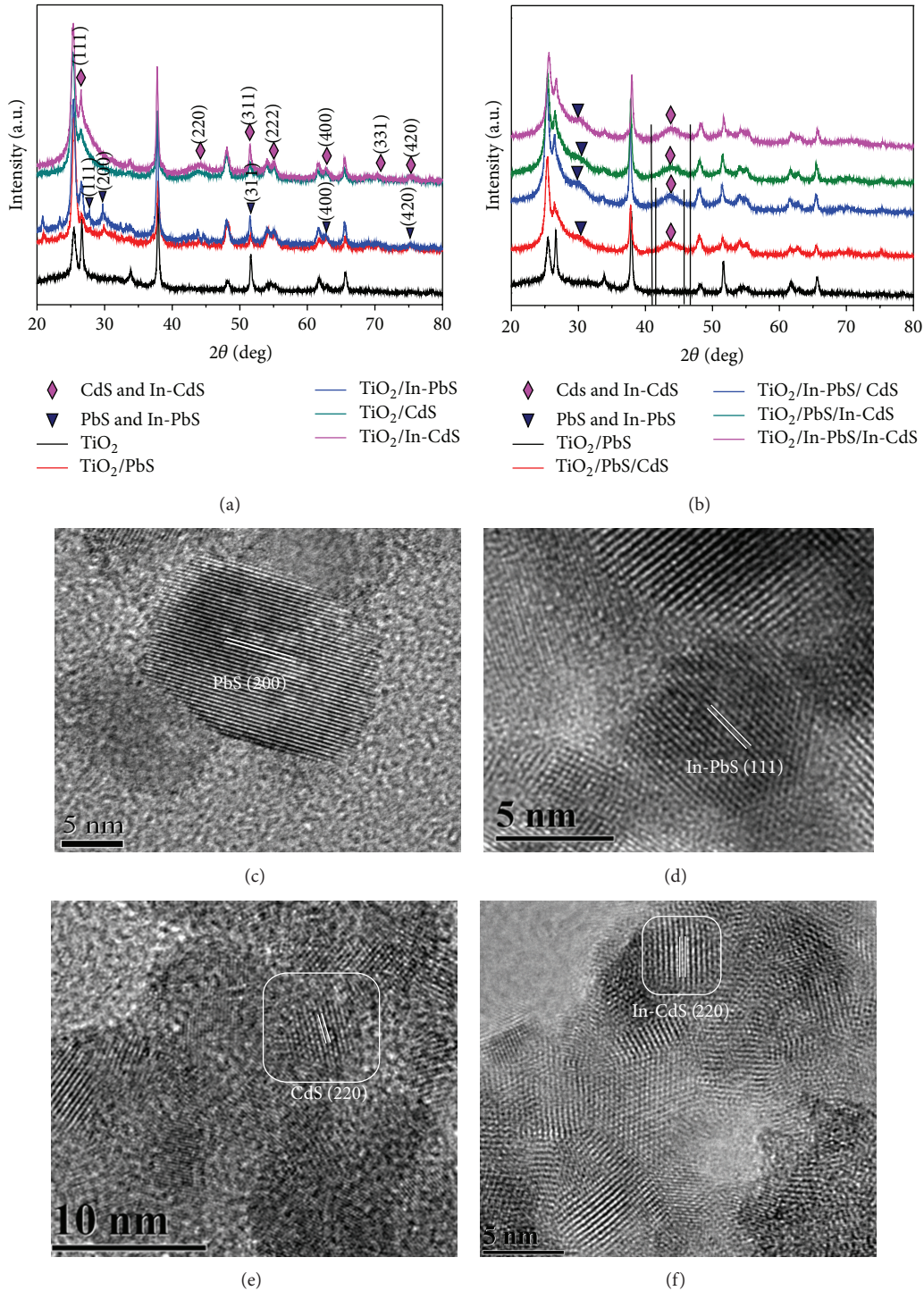


FIGURE 2: The XRD patterns of (a) four QDs and TiO₂ and (b) four heterojunctions and TiO₂; the HRTEM of (c) PbS, (d) In-PbS; (e) CdS, and (f) In-CdS.

SILAR method. In addition, the concentration of PbS and CdS which was doped In atoms has no significant increase or decrease, while the concentration in solid film of In atoms would vary with SILAR cycles.

The X-ray diffraction (XRD) patterns are shown in Figure 2. The XRD patterns show the PbS and CdS all are

cubic structure. The diffraction maximum peak of PbS is (200) at 27.834°, while the higher peaks of In-PbS are (111) and (200) at 26.76° and 27.834°, respectively. However, the major peaks of CdS and In-CdS both are (220) at 43.972°, but a broadening of the peak of In-CdS relative to CdS is seen. Figure 2(b) is the XRD patterns of four heterojunctions.

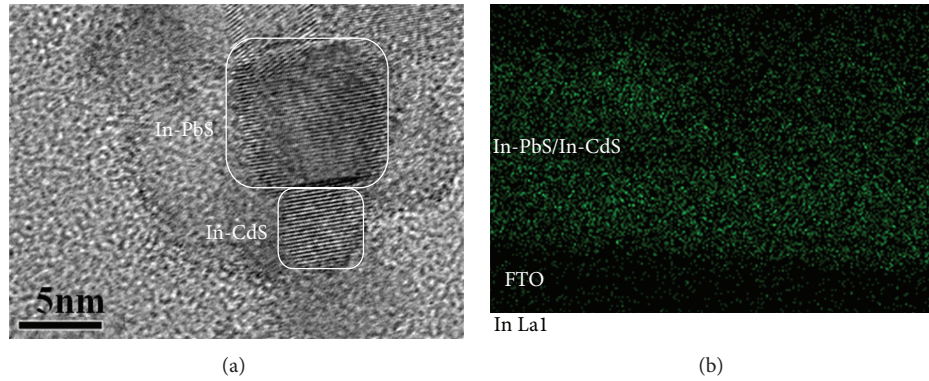


FIGURE 3: (a) The HRTEM of In-PbS/In-CdS and (b) the EDX mapping of the cross section In-PbS/In-CdS QD sensitized TiO_2 film.

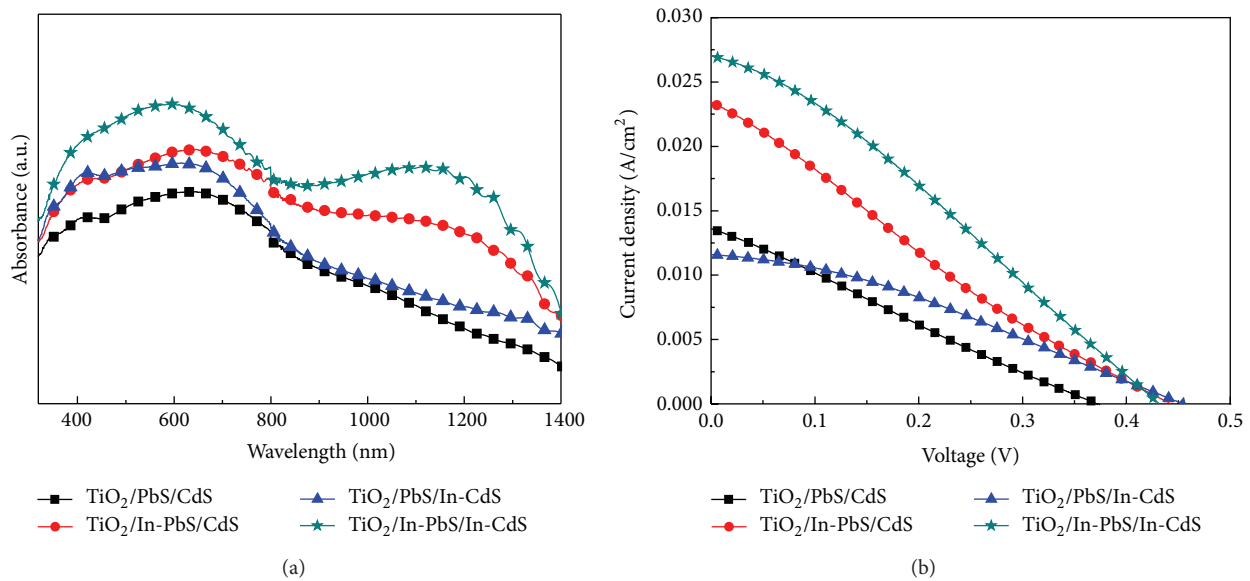


FIGURE 4: (a) Diffuse reflectance absorbance spectra of different QD sensitized films; (b) J - V characteristics of different working heterojunctions.

If In atoms were incorporated into PbS (In-PbS/CdS), the peak is moved to 26.76° from 27.834° ; this is because of the appearance of (111) peak of In-PbS at 26.76° , while the peak is broadened at 43.972° after incorporating In atom into CdS (PbS/In-CdS); this is because of the broadening of the (220) peak of In-CdS. When both incorporate In atom into PbS and CdS (In-PbS/In-CdS), the peak is moved from 27.834° to 26.76° and is broadened at 43.972° . Because of lattice distortions or changes as a result of In doping, it can be confirmed that PbS or CdS has been incorporated. The high-resolution electron transmission electron microscopy (HRTEM) images of QDs also are shown in Figure 2. We can reckon that the particle size of PbS and In-PbS is about 10 nm and 5 nm, respectively, while the major peaks is different, that matches the change of XRD patterns. The particle size of PbS or In-PbS is surprisingly smaller than their Bohr radius [17]. The particle sizes of CdS and In-CdS are all about 5 nm, which is bigger than their Bohr radius and smaller than 10 nm [18].

The HRTEM image of In-PbS/In-CdS QDs is shown in Figure 3(a). The information obtained from Figure 3(a) agrees with Figures 2(d) and 2(f). The EDX mapping of the cross section In-PbS/In-CdS QD sensitized TiO_2 film is shown in Figure 3(b). The In element not only exists in film, but also is evenly distributed along depth. Such a distribution is not only because In-PbS or In-CdS were assembled in the TiO_2 mesoporous by using SILAR but because same proportion indium chloride was mixed with lead nitrate or cadmium nitrate as a cation source.

The light absorption property of PbS/CdS without or with In dopant sensitized TiO_2 film is assessed by UV-vis absorption spectra, Figure 4(a). The absorption property in the visible range increased when the CdS was doped (PbS/In-CdS); however, no apparent contrast increase was found in the long wavelength region. The absorption property for wavelength longer than 1000 nm increases greatly when the PbS was doped (In-PbS/CdS). But the absorption of

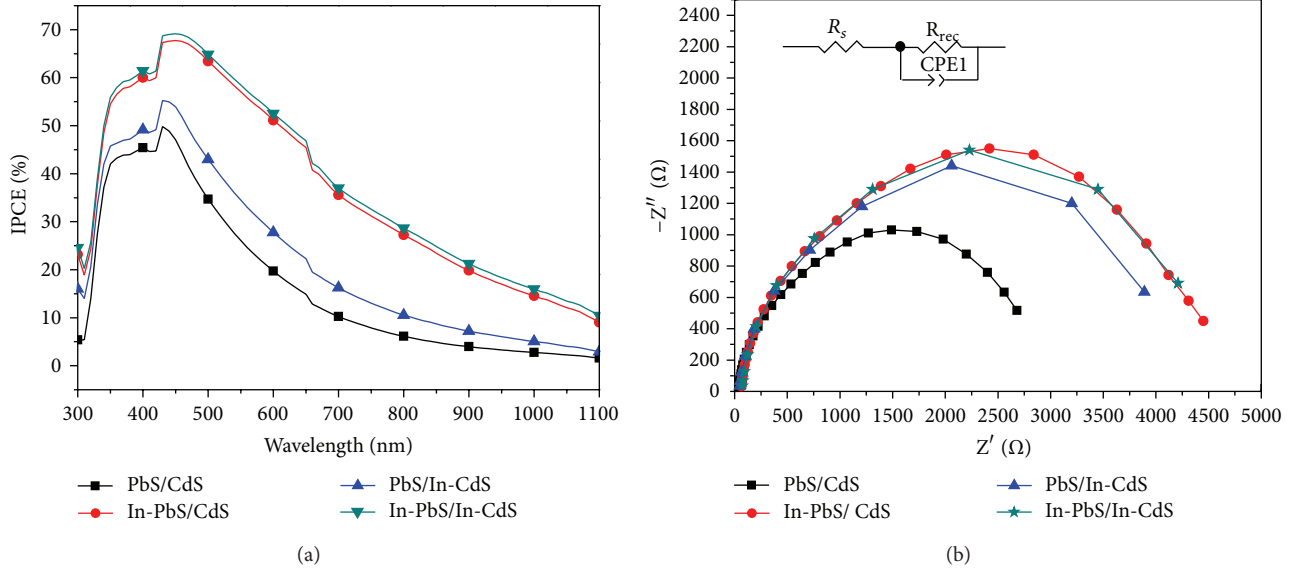


FIGURE 5: (a) IPCE spectra for four devices; (b) EIS spectra of QDSSCs measured in the dark at -0.4 V bias voltages. The inset illustrates the equivalent circuit simulated. R_{rec} and $CPE1$ represent the charge transfer resistance and capacitance at TiO_2 /electrolyte interface, respectively; R_s is a series resistance.

TABLE 1: Different photovoltaic parameter for different working heterojunctions.

Samples	J_{sc} (mA/cm^2)	V_{oc} (V)	FF	η (%)
$TiO_2/PbS/CdS$	13.61	0.37	0.25	1.26
$TiO_2/In-PbS/CdS$	23.4	0.44	0.23	2.36
$TiO_2/PbS/In-CdS$	11.6	0.45	0.32	1.69
$TiO_2/In-PbS/In-CdS$	27.01	0.43	0.29	3.42

In-PbS/CdS deposited film also increased in the visible range, which is due to the diffusion of indium atoms from In-PbS/CdS interface where In is not stable into CdS quantum dot [19]. Both the PbS and CdS were incorporated with indium (In-PbS/In-CdS), not only increased the light absorption in the visible range, and an absorption peak has emerged in the near-infrared portion. ICP-OES analysis illustrates that the concentration of PbS and CdS has no significant increase or decrease; it is excluded that the higher light adsorption was attributed to the possibility of the increase of PdS or CdS for the “doped” samples compared with the undoped ones fabricated via SILAR process, while, the absorption peak emerged in the near-infrared portion is the absorption peak of the exciton of the In-PbS QD.

The J - V characteristics of these four QDSSCs are presented in Figure 4(b). The J_{sc} , V_{oc} , fill factor (FF), and power conversion efficiency (η) are summarized in Table 1. An increase of V_{oc} is seen in the cells that incorporate foreign atoms. Similarly, cells that the PbS with indium atoms exhibited a significant increase in the photocurrent as compared to the corresponding cells without indium atoms. The absorption property has been able to explain why the higher J_{sc} was achieved in this study. However, PbS/In-CdS films exhibited decrease in the photocurrent and great increase in the J_{sc} ,

which is due to an accumulation of photo-generated electron in QD layers, but improve the V_{oc} . As we expect, doped heterojunction used in solar cells can significantly increase J_{sc} and the V_{oc} was improved at the same time; an energy conversion efficiency of 3.42% was achieved.

The incident photon to carrier conversion efficiency (IPCE) recorded at different incident light wavelengths for QDSC that employ four different photo-anodes is shown in Figure 5(a). The overall photocurrent response matches the absorption features; IPCE values as high as 70% can be achieved by the $TiO_2/In-PbS/In-CdS$ device. Significant retaining in IPCE is seen for $TiO_2/In-PbS/In-CdS$ device with 10% at 1100 nm. It is worth noting that the IPCE of $TiO_2/PbS/In-CdS$ is higher than undoped ones, but the J_{sc} is lower. As we know, the IPCE represents how many electrons were generated when a photon was absorbed. So the $TiO_2/PbS/In-CdS$ generated more electrons, but they could not transport completely to FTO. There are two reasons; the impurity energy level is lower than conduction band of $TiO_2/PbS/CdS$; some of the electrons accumulated on the impurity energy level to improve V_{oc} . On the other hand, the electron on the conduction band of In-CdS would be back to impurity energy level to combine with the hole. As we expect, doped heterojunction used in solar cells can significantly broaden scope of light harvest into near-infrared portion and promote IPCE at long wavelength. Figure 5(b) shows the electrochemical impedance spectroscopy (EIS) of QDSSCs based on PbS/CdS, In-PbS/CdS, PbS/In-CdS, and In-PbS/In-CdS electrodes measured in the dark at -0.4 V bias voltages. The equivalent circuit simulated which applies to the impedance spectroscopy was inset of Figure 5(b); R_{rec} and $CPE1$ represent the charge transfer resistance and capacitance at TiO_2 /electrolyte interface, respectively; R_s is series resistance that would account for the transport

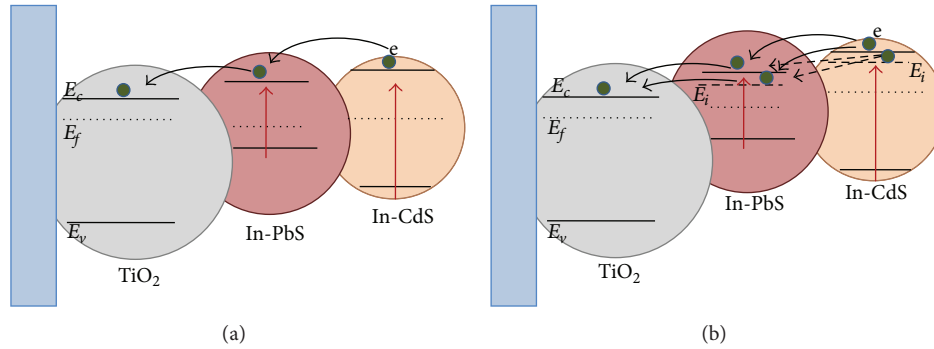


FIGURE 6: The schematic illustration of the carrier transfer in the (a) $\text{TiO}_2/\text{PbS}/\text{CdS}$ film and (b) $\text{TiO}_2/\text{In-PbS}/\text{In-CdS}$ film. Black arrow showed the electron transport; red arrow showed the electron transition.

resistance of FTO and the connection setup. It can be noticed that incorporating of indium atoms would enhance the value of the R_{rec} , which indicates that the recombination rate of electrons is slower than undoped ones. But seldom is a major change in the value of the R_s .

Figure 6(a) shows the schematic illustration of the electron transfer model for $\text{TiO}_2/\text{PbS}/\text{CdS}$ film. PbS QDs and CdS QDs absorb photon to create pairs of electrons and holes, the electron transports to TiO_2 from QDs, and then the electron transports to FTO from TiO_2 . The hole transports to electrolyte from QDs. The TiO_2 particles are designed to give a large surface area for QDs to grow on. In addition, TiO_2 particles are the transporting layer of the electron. As shown in Figure 5(b), the impurity energy level is the presence in PbS or CdS QD. The presence of impurity energy level not only increased the light absorption in the near-infrared portion, but also improves transmission dynamics of electron and transport path between two nanoparticles. Most electrons were transport to FTO; the combination rate of electrons in film would be slower. So the J_{sc} ballooned to $27.01 \text{ mA}/\text{cm}^2$ of $\text{TiO}_2/\text{In-PbS}/\text{In-CdS}$ devices. The presence of impurity energy level will accumulate electron within the QD layers, thus shifting the Fermi level to more negative potentials and increasing the conduction band of CdS. The V_{oc} of $\text{TiO}_2/\text{In-PbS}/\text{In-CdS}$ device was improved.

There is no doubt that incorporated heterojunction used in QDSCs would significantly increase the J_{sc} ; the V_{oc} have an improvement at the same time. Although such a high J_{sc} is rare, it can be further increased to prevent exciton fast recombining to, such as coat with ZnS or dyes at the outer surface of CdS [20]. In addition, the power conversion efficiency can be also enhanced by improve electrolyte and counter electrode [8, 9].

4. Conclusion

A foreign atom—indium atom was incorporated into PbS/CdS QDs to prepare In-PbS/In-CdS heterojunction by successive ionic layer adsorption and reaction method which is a chemical method. Experimental results indicate that PbS or CdS has been doped with In by SILAR method; the concentration of PbS and CdS which was doped In

atoms has no significant increase or decrease. In addition, incorporating of indium atoms has resulted in the lattice distortions or changes of PbS or CdS and improved the light harvest of heterojunction. Using this heterojunction, Pt counter electrode and polysulfide electrolyte to fabricate quantum dot sensitized solar cells, the short circuit current density ballooned to $27.01 \text{ mA}/\text{cm}^2$ from $13.61 \text{ mA}/\text{cm}^2$, and the open circuit voltage was improved to 0.43 V from 0.37 V at the same time.

Conflict of Interests

The authors declare that there is no conflict of interests regarding the publication of this paper.

Acknowledgments

This work was partially supported by Key Project of Beijing Natural Science Foundation (3131001), Key Project of Natural Science Foundation of China (91233201 and 61376057), Key Project of Beijing Education Committee Science & Technology Plan (KZ201211232040), State 863 Plan of MOST of PR China (2011AA050527), Beijing National Laboratory for Molecular Sciences (BNLMS2012-21), State Key Laboratory of Solid State Microstructures of Nanjing University (M27019), State Key Laboratory for Integrated Optoelectronics of Institute of Semiconductors of CAS (IOSKL2012KF11), State Key Laboratory for New Ceramic and Fine Processing of Tsinghua University (KF1210), Key Laboratory for Renewable Energy and Gas Hydrate of Chinese Academy of Sciences (y207ka1001), Beijing Key Laboratory for Sensors of BISTU (KF20131077208), and Beijing Key Laboratory for Photoelectrical Measurement of BISTU (GDKF2013005).

References

- [1] N. S. Karan, D. D. Sarma, R. M. Kadam, and N. Pradhan, "Doping transition metal (Mn or Cu) ions in semiconductor nanocrystals," *Journal of Physical Chemistry Letters*, vol. 1, no. 19, pp. 2863–2866, 2010.
- [2] V. Chikan, "Challenges and prospects of electronic doping of colloidal quantum dots: Case study of CdSe," *Journal of Physical Chemistry Letters*, vol. 2, no. 21, pp. 2783–2789, 2011.

- [3] S. Roy, C. Tuinenga, F. Fungura, P. Dagtepe, V. Chikan, and J. Jasinski, "Progress toward producing n-type CdSe quantum dots: Tin and indium doped CdSe quantum dots," *Journal of Physical Chemistry C*, vol. 113, no. 30, pp. 13008–13015, 2009.
- [4] Y. Justo, B. Goris, J. S. Kamal, P. Geiregat, S. Bals, and Z. Hens, "Multiple dot-in-rod PbS/CdS heterostructures with high photoluminescence quantum yield in the near-infrared," *Journal of the American Chemical Society*, vol. 134, no. 12, pp. 5484–5487, 2012.
- [5] W. Lee, W.-C. Kwak, S. K. Min et al., "Spectral broadening in quantum dots-sensitized photoelectrochemical solar cells based on CdSe and Mg-doped CdSe nanocrystals," *Electrochemistry Communications*, vol. 10, no. 11, pp. 1699–1702, 2008.
- [6] R. Zeng, M. Rutherford, R. Xie, B. Zou, and X. Peng, "Synthesis of highly emissive Mn-Doped ZnSe nanocrystals without pyrophoric reagents," *Chemistry of Materials*, vol. 22, no. 6, pp. 2107–2113, 2010.
- [7] Z. Huang, X. Zou, and H. Zhou, "A strategy to achieve superior photocurrent by Cu-doped quantum dot sensitized solar cells," *Materials Letters*, vol. 95, pp. 139–141, 2013.
- [8] A. Braga, S. Giménez, I. Concina, A. Vomiero, and I. Mora-Seró, "Panchromatic sensitized solar cells based on metal sulfide quantum dots grown directly on nanostructured TiO₂ electrodes," *Journal of Physical Chemistry Letters*, vol. 2, no. 5, pp. 454–460, 2011.
- [9] J. W. Lee, D. Y. Son, and T. K. Ahn, "Quantum-dot-sensitized solar cell with unprecedentedly high photocurrent," *Scientific Reports*, vol. 3, article 1050, 2013.
- [10] P. K. Santra and P. V. Kamat, "Mn-doped quantum dot sensitized solar cells: a strategy to boost efficiency over 5%," *Journal of the American Chemical Society*, vol. 134, no. 5, pp. 2508–2511, 2012.
- [11] H. J. Lee, P. Chen, S.-J. Moon et al., "Regenerative PbS and CdS quantum dot sensitized solar cells with a cobalt complex as hole mediator," *Langmuir*, vol. 25, no. 13, pp. 7602–7608, 2009.
- [12] J. Gao, J. M. Luther, O. E. Semonin, R. J. Ellingson, A. J. Nozik, and M. C. Beard, "Quantum dot size dependent J-V characteristics in heterojunction ZnO/PbS quantum dot solar cells," *Nano Letters*, vol. 11, no. 3, pp. 1002–1008, 2011.
- [13] S. Baidyaroy and P. Mark, "Analytical and experimental investigation of the effects of oxygen chemisorption on the electrical conductivity of CdS," *Surface Science*, vol. 30, no. 1, pp. 53–68, 1972.
- [14] H. M. Pathan and C. D. Lokhande, "Deposition of metal chalcogenide thin films by successive ionic layer adsorption and reaction (SILAR) method," *Bulletin of Materials Science*, vol. 27, no. 2, pp. 85–111, 2004.
- [15] A. H. Ip, S. M. Thon, S. Hoogland et al., "Hybrid passivated colloidal quantum dot solids," *Nature Nanotechnology*, vol. 7, pp. 577–582, 2012.
- [16] L. Y. Chang, R. R. Lunt, P. R. Brown, V. Bulovic, and M. G. Bawendi, "Low-temperature solution-processed solar cells based on PbS colloidal quantum Dot/CdS heterojunctions," *Nano Letters*, vol. 13, no. 3, pp. 994–999.
- [17] W. W. Frank, "Lead salt quantum dots: the limit of strong quantum confinement," *Accounts of Chemical Research*, vol. 33, no. 11, pp. 773–780, 2000.
- [18] X. Xu, Y. Zhao, E. J. Sie et al., "Dynamics of bound exciton complexes in CdS nanobelts," *ACS Nano*, vol. 5, no. 5, pp. 3660–3669, 2011.
- [19] J. N. David, L. E. Alexander, and C. E. Steven, *Accounts of Chemical Research*, vol. 33, pp. 773–780, 2000.
- [20] N. Gujjarro, J. M. Campiña, Q. Shen et al., "Uncovering the role of the ZnS treatment in the performance of quantum dot sensitized solar cells," *Physical Chemistry Chemical Physics*, vol. 13, no. 25, pp. 12024–12032, 2011.

Research Article

Excellent Silicon Surface Passivation Achieved by Industrial Inductively Coupled Plasma Deposited Hydrogenated Intrinsic Amorphous Silicon Suboxide

Jia Ge,^{1,2} Muzhi Tang,¹ Johnson Wong,¹ Zhenhao Zhang,³
Torsten Dippell,³ Manfred Doerr,³ Oliver Hohn,³ Marco Huber,³ Peter Wohlfart,³
Armin G. Aberle,¹ and Thomas Mueller¹

¹ Solar Energy Research Institute of Singapore, National University of Singapore, Singapore 117574

² NUS Graduate School for Integrative Sciences and Engineering, National University of Singapore, Singapore 117456

³ Singulus Technologies AG, Hanauer Landstraße 103, 63796 Kahl Am Main, Germany

Correspondence should be addressed to Jia Ge; gejia@nus.edu.sg

Received 28 March 2014; Accepted 11 May 2014; Published 1 June 2014

Academic Editor: Aung Ko Ko Kyaw

Copyright © 2014 Jia Ge et al. This is an open access article distributed under the Creative Commons Attribution License, which permits unrestricted use, distribution, and reproduction in any medium, provided the original work is properly cited.

We present an alternative method of depositing a high-quality passivation film for heterojunction silicon wafer solar cells, in this paper. The deposition of hydrogenated intrinsic amorphous silicon suboxide is accomplished by decomposing hydrogen, silane, and carbon dioxide in an industrial remote inductively coupled plasma platform. Through the investigation on CO₂ partial pressure and process temperature, excellent surface passivation quality and optical properties are achieved. It is found that the hydrogen content in the film is much higher than what is commonly reported in intrinsic amorphous silicon due to oxygen incorporation. The observed slow depletion of hydrogen with increasing temperature greatly enhances its process window as well. The effective lifetime of symmetrically passivated samples under the optimal condition exceeds 4.7 ms on planar *n*-type Czochralski silicon wafers with a resistivity of 1 Ωcm, which is equivalent to an effective surface recombination velocity of less than 1.7 cm s⁻¹ and an implied open-circuit voltage (V_{oc}) of 741 mV. A comparison with several high quality passivation schemes for solar cells reveals that the developed inductively coupled plasma deposited films show excellent passivation quality. The excellent optical property and resistance to degradation make it an excellent substitute for industrial heterojunction silicon solar cell production.

1. Introduction

Heterojunction silicon wafer (HET) solar cells have achieved very high efficiencies of up to 24.7% on a large area (101.8 cm²) [1]. Its high efficiency mainly stems from an extremely high open-circuit voltage (V_{oc}) of up to 750 mV thanks to the excellent surface passivation. Such a cell structure has attracted attention not only due to its high conversion efficiency, but also due to its low process temperature which avoids bowing when using thin wafers [2, 3]. The insertion of a high-quality hydrogenated intrinsic amorphous silicon (a-Si:H(i)) thin film between the emitter (or back surface field) and the bulk material is the key to such a high cell efficiency

[4–7]. Therefore, optimization of this buffer layer is of utmost importance.

Plasma-enhanced chemical vapour deposition (PECVD) of a-Si:H(i) has been the key to the successful industrial implementation of this technology as a passivation scheme, since the early 1990s [5, 8, 9], mainly thanks to its low temperature process and good surface passivation quality [10]. However, it is also reported that the optimization for such a layer is difficult because of possible epitaxial growth and the need to balance plasma species during deposition [11–14].

PECVD hydrogenated intrinsic amorphous silicon suboxide (a-SiO_x:H(i)) thin films are emerging as an alternative

to replace a-Si:H(i) as passivation layer in HET solar cells. Its excellent passivation quality and optical property has been demonstrated by several groups in recent years [15–19]. Notably, Mueller et al. [16, 18, 20, 21] have shown a record of high passivation quality on highly doped wafers using direct capacitively coupled plasma (CCP). The optical loss reported was also much lower than that of a-Si:H(i), proving promising potential as a passivation layer. However, in order to achieve a state-of-the-art passivation level, the mentioned group has used very high plasma frequencies (70–110 MHz) and prolonged annealing processes, which can be difficult to implement in industrial production. Furthermore, direct CCP can introduce extra damage to wafer surface during deposition, thus limiting the film's passivation quality.

In this paper, we present an alternative method of depositing a-SiO_x:H(i) thin film using a remote inductively coupled plasma (ICP) source operating at conventional frequency (13.56 MHz). It is well known that very high density plasma can be produced in an ICP system with low and narrowly distributed particle energy compared to CCP [22–24], and the wafer surface is less influenced by plasma condition by keeping substrate from plasma in a remote system. Therefore, the passivation quality of a-SiO_x:H(i) can be further improved with reduced process time. In this preliminary study, the optimization of a-SiO_x:H(i) is carried out in terms of passivation quality on highly doped material. The influence of CO₂ partial pressure and process temperature on the passivation quality is investigated. Detailed analyses, such as quasi-steady-state photoconductance (QSSPC) measurements, spectroscopic ellipsometry (SE), time-of-flight (TOF) secondary ion mass spectroscopy (SIMS), and Fourier transform infrared (FTIR) spectroscopy, are conducted to understand the passivation quality, film thickness, composition, optical bandgap, and chemical bonding configuration. In the last section, comparison with other high-quality passivation schemes is made in order to demonstrate the excellent passivation and optical qualities with good stability against ambient environment of the ICP a-SiO_x:H(i) films.

2. Experimental Details

The a-SiO_x:H(i) thin films were fabricated by decomposing silane (SiH₄), hydrogen (H₂), and carbon dioxide (CO₂) in a remote ICP system, the SINGULAR-HET. It is a fully automatic ICPECVD system developed by Singulus Technologies in collaboration with SERIS for industrial HET solar cell processing. The system has one infrared (IR) heating station (PS1) for preheating and four other process stations (PS2–PS5) for deposition. It has two stations (PS2 and PS5) for topside deposition and two stations (PS3 and PS4) for bottom-side deposition. Double-side deposition is accomplished by using PS2 and PS3 without breaking the vacuum. The process temperature is adjusted by changing the heater power setting in PS1 as well as the stabilization heater in each process station. The temperature is monitored by pyrometers installed after each station. The pyrometers are calibrated to Si wafers and verified using in situ thermal couple readings in the temperature range of interest. The Si wafers are loaded into the system using an automated cassette

TABLE 1: Plasma parameter variation used in this paper.

Plasma parameter	Value/range
Power	750 W
Deposition time	1–60 s
[SiH ₄]/[H ₂]	1
CO ₂ partial pressure (χ _o)	0–22%
Temperature	50–400°C

wafer handling unit. The structure and process cycle of the SINGULAR-HET is illustrated in Figures 1(a) and 1(b).

In each process station, the ICP source is driven by a radiofrequency (RF, 13.56 MHz) generator through a matching box. The reactive gases (H₂ and CO₂) are fed through a gas shower into the area surrounded by an inductive coil, where the plasma is generated. The deposition precursor gas (SiH₄) is introduced through a distribution ring outside the inductive coil near the wafers. The decomposed species travel downwards for PS2/5 onto the wafer surface to form the film. The ICP source and process station design are shown in Figure 1(c).

The a-SiO_x:H(i) films were deposited onto both sides of planar 160 μm thick 156 mm wide Czochralski (Cz) wafers with crystal orientation of ⟨100⟩. The choice of the *n*-type 1 Ωcm Cz wafer as the bulk material is based on the applicability to real HET solar cell fabrication. The film thickness was about 20 nm, except for the results shown in Section 3.1. This symmetrical a-SiO_x:H(i)/c-Si/a-SiO_x:H(i) structure was used to monitor the passivation quality. The same films were also deposited onto one side of highly resistive Si wafers for FTIR analyses. Before deposition, all wafers underwent an alkaline based silicon etch and a standard RCA (Radio Cooperation of America) cleaning followed by a one-minute dip in 1% hydrofluoric (HF) acid solution to remove the chemical oxide. After rinse and drying, the wafers were loaded onto substrate carriers and transferred into the load lock. Plasma parameters used in this work are summarized in Table 1. It should be noted that equal flow rates for SiH₄ and H₂ were used throughout this investigation. CO₂ flow rate was monitored and shown in terms of partial pressure defined by

$$\chi_o = \frac{[\text{CO}_2]}{[\text{CO}_2] + [\text{SiH}_4]} \times 100\%, \quad (1)$$

where square brackets represent the corresponding gas flow rate in standard cubic centimetre per minute (sccm). Furthermore, the process temperature is reported using the pyrometer reading on the wafer surface after PS1.

The effective minority carrier lifetime (τ_{eff}) of the symmetrical samples was determined using the QSSPC method in appropriate modes [39]. The τ_{eff} reported are as-deposited values extracted at a minority carrier injection level of 10¹⁵ cm⁻³ and approximately two minutes after deposition. Thermal annealing was avoided in this study so that the process is industrially compatible. The thickness of the film was determined by fitting SE data (300–800 nm). The fitting model comprised an underlying SiO₂ layer with a fixed

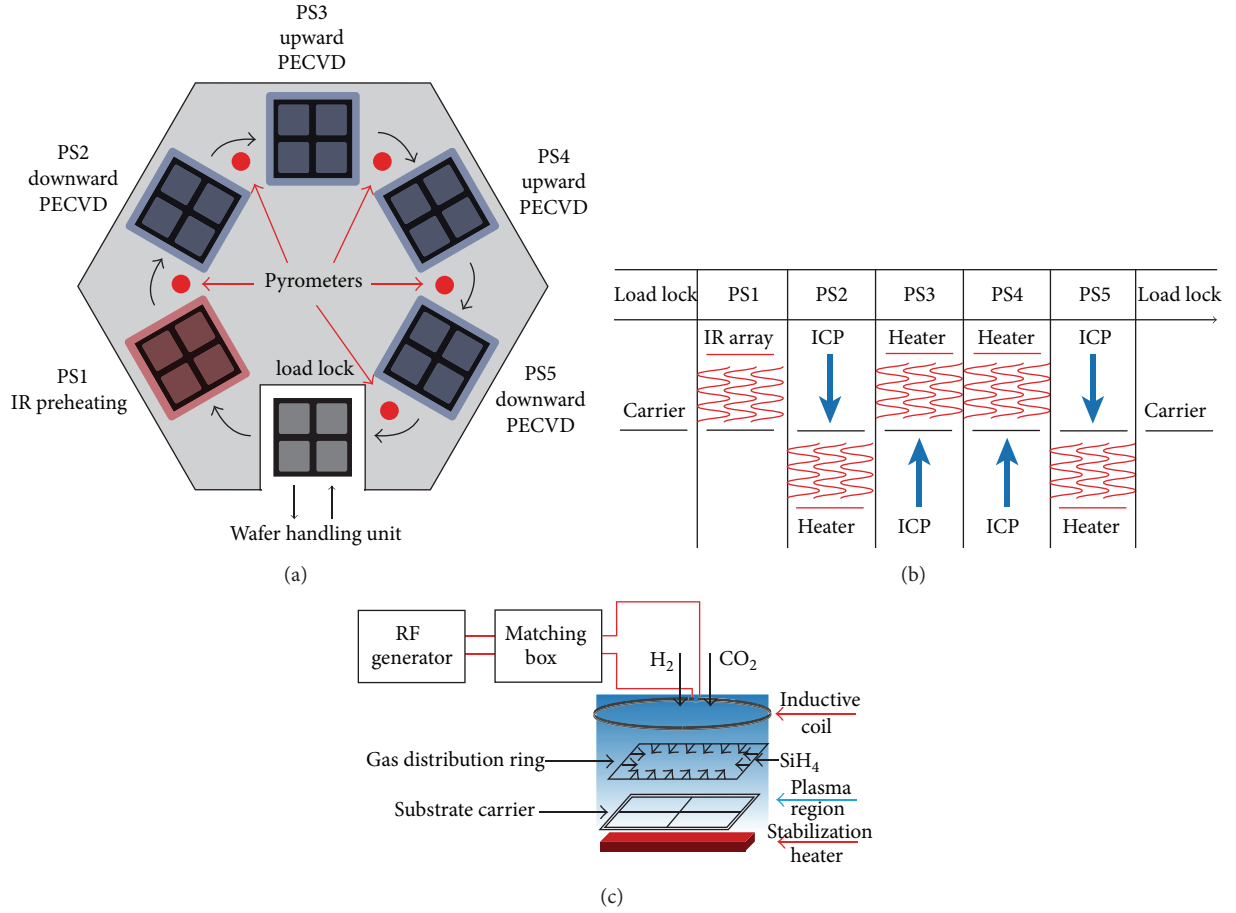


FIGURE 1: (a) Illustration of processing unit structure of the SINGULAR-HET. The arrows indicate the direction for carrier rotation and transfer. (b) Illustration of the process cycle. The horizontal arrow indicates processing order and the vertical arrows represent the direction of deposition in each station. (c) Illustration of process station and plasma design for plasma stations in downward deposition configuration. After [25, 26].

TABLE 2: Bonding types/modes and corresponding wavenumbers investigated by FTIR in this paper.

Bonding type	Mode wavenumber (cm ⁻¹)		
	Wagging/rocking	Bending	Stretching
Si-O-Si	—	810 ^a	—
Si-H(Si ₃)	640 ^b	—	2000–2200 ^c
Si-H(Si ₂ O)	—	—	1054 ^{d,e}
Si-H(SiO ₂)	—	—	1107 ^{d,e}
Si-H(SiO ₃)	—	—	1156 ^{d,e}
(SiH ₂) _n	—	845 ^f	—
	—	883 ^f	—

^aReference [34].

^bReference [35].

^cReference [36].

^dReference [15].

^eReference [37].

^fReference [38].

thickness of 1 nm, an a-SiO_x:H(i) layer characterized by Tauc-Lorentz (TL) model [40], and an overlayer consisting of 50% bulk material and 50% voids to represent the surface

roughness. The absorption coefficient (α) of the film was determined from the fitted distinction coefficient (k) using $\alpha = 4\pi k/\lambda$, where λ is the wavelength.

The optical bandgap of the film was then determined by Tauc's method [41]. In order to investigate the bonding configuration in the film, FTIR measurement (500–4000 cm⁻¹) in transmission mode was carried out with a spectral resolution of 2 cm⁻¹. The bonding configurations of interest are summarized in Table 2. The total H content (C_H) in the film was obtained from the integrated intensity under the Si-H(Si₃) wagging mode peak [35], while the microstructure factor (r) was determined by the following equation [42]:

$$r = \frac{I_{2100}}{I_{2000} + I_{2100}}, \quad (2)$$

where I_j represents the integrated intensity under the peak denoted by the corresponding subscript. The peak intensity was obtained by deconvoluting the Si-H(Si₃) stretching peak using Gaussian curves. In particular, the peak centred at 2000 cm⁻¹ usually represents monohydride configuration,

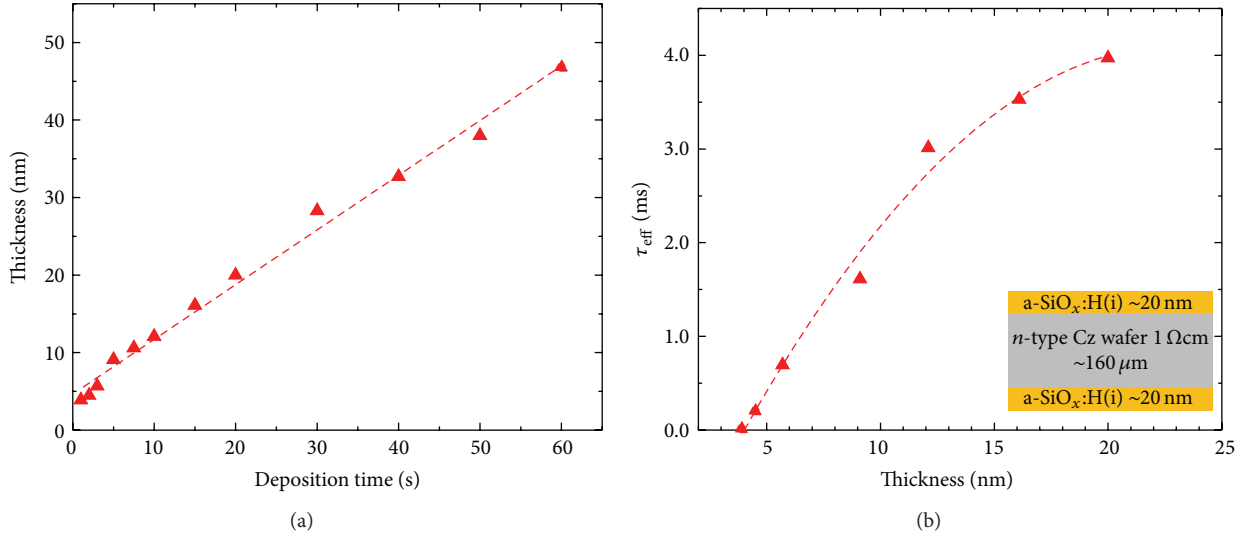


FIGURE 2: (a) a-SiO_x:H(i) thin film thickness as a function of deposition time; (b) τ_{eff} as a function of a-SiO_x:H(i) film thickness. The inset shows the sample structure used in lifetime determination. The lines are guides for the eye. A constant deposition rate is observed for all samples in this series. Lifetime saturation is observed after 20 nm film deposition.

while the peak at 2100 cm⁻¹ represents the response from higher order hydrides [43, 44].

In order to quantify the atomic concentration of C and O under different χ_o , TOF SIMS (IONTOF) was conducted on selected samples using a 25 keV Bi+ beam with a current of 1 pA on a 80 × 80 μm² spot. Sputtering was done using a 1 keV Cs+ gun with a current of 8 nA on a 250 × 250 μm² area. The data were presented in both absolute atomic concentration per cubic centimetre and percentage over the host Si atoms. For percentage calculation, standard atomic concentration of crystalline Si was used (5 × 10²² cm⁻³) without considering density change in amorphous material. This is justified by the negligible density change in amorphous Si reported by Smets et al. [45] and Remeš et al. [46, 47] under different C_H.

3. Results and Discussions

3.1. Deposition Time and Film Thickness. The investigation first focused on the deposition rate of a-SiO_x:H(i) in the ICP system in order to determine the thickness of film on which further optimization will be carried out. The result is shown in Figure 2(a).

A linear relationship between thickness and deposition time is observed, demonstrating a stable and robust deposition process for all samples. The nonzero interception at 0 deposition time can be attributed to the fluctuating plasma condition and nucleus formation at plasma ignition. A deposition rate of about 7 Ås⁻¹ can be deduced from the slope of the linear fit. The same linear growth was also reported by Pysch et al. in a different ICP system for a-Si:H(i) deposition [48]. The linear behaviour can facilitate the thickness control in the subsequent optimization. Notably, the relatively high deposition rate can greatly reduce deposition time needed in real device fabrication. For a typical passivation layer of

5 nm or below, 1 to 2 s deposition is sufficient, thus largely enhancing the throughput.

The relationship between passivation quality and film thickness was then explored and presented in Figure 2(b). It can be observed that the passivation quality increases rapidly at low film thickness. The improvement of lifetime slows down after a film thickness of 10 nm and then tends to saturate after 20 nm. The saturation of τ_{eff} in terms of film thickness can be attributed to the reduction of interface defect density due to better network and surface coverage. This saturation effect was reported in the literature on different passivation materials [16, 24]. Further increase in film thickness can only provide marginal improvement of passivation quality, with the possible risk of inducing morphological change in the film (discussed in Section 3.3.3). Therefore, the film thickness is controlled at about 20 nm in this paper to ensure lifetime saturation. Such a thickness avoids second order effects that distort the actual passivation quality of the film while maintaining the minimal process time. At the same time, the similar film thickness ensures fair comparison on passivation quality across different plasma settings.

3.2. CO₂ Partial Pressure

3.2.1. Passivation Quality. While fixing the film thickness at about 20 nm, a scan on CO₂ partial pressure was performed in this experiment. Other plasma parameters were kept constant in this section. By varying the concentration of CO₂ in the plasma, compositional change that affected film passivation quality was expected. The lifetime results are illustrated in Figure 3.

It is shown that the increase of CO₂ partial pressure of up to about 10% improves passivation quality. Any increase beyond the optimal amount deteriorates the lifetime. The relatively low lifetime in Figure 3 is due to nonoptimized

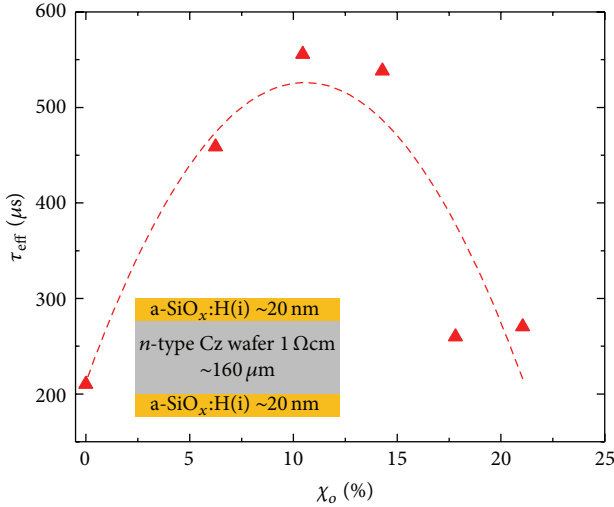


FIGURE 3: Lifetime as a function of CO_2 partial pressure while keeping other deposition conditions constant. The inset shows sample structure used in measuring lifetime. The line is a guide to the eye. A lifetime peak is observed at CO_2 partial pressure of 10%.

wafer temperature in this series. However, it should be noted that only a small amount of CO_2 is needed to greatly improve the passivation quality, as compared to a-Si:H(i) (denoted by 0% partial pressure in the same figure). It is also interesting to notice that the optimal CO_2 partial pressure in our ICP system is only about half of what was reported by Mueller et al. [16, 18, 20]. The difference could be a strong indication of different plasma chemistry and reactor design. The initial improvement of lifetime with respect to CO_2 flow rate can be explained by the increase of H content (C_H) in the film. Higher CO_2 partial pressure in the plasma induces higher O content inside the resultant film. As H atoms can easily bond to Si atoms that are back bonded by O atoms [49], higher C_H is expected due to O incorporation. Indeed, this argument will be supported with FTIR spectra and H content calculations.

Once beyond the optimal point, lifetime starts to reduce with increasing CO_2 flow rate. Several groups [16, 18, 19] attribute this phenomenon to increasing defect density due to higher C impurity concentration in the film. Considering similar CO_2 partial pressure used by Mueller et al. [16, 18] and Hoex et al. [19] compared to this work, higher impurity incorporation can be regarded as one of the reasons that cause lifetime degradation at higher CO_2 flow rate in this study as well. However, by examining FTIR spectra and bonding configuration under different CO_2 flow conditions, it can be concluded that the reduction of C_H at higher O concentration is a key reason for the degradation beyond the optimal point. TOF SIMS analysis also reveals that the concentration of C atoms in a-SiO_x:H(i) is quite small even at the highest χ_o used in this work.

3.2.2. Bonding Configuration Analysis. In order to further investigate the influence of CO_2 partial pressure on the film property, FTIR analysis was carried out. The results are shown in Figure 4. Note that for all samples, contribution from O–H

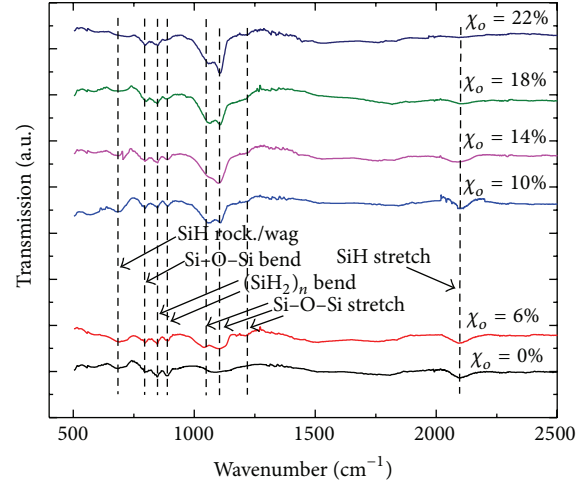


FIGURE 4: FTIR transmission spectra of a-SiO_x:H(i) films under different χ_o . Higher O content in the film is observed with increasing CO_2 partial pressure, with Si–H(SiO₂) being the dominant bonding configuration. C_H increases with O content at first due to O facilitated inclusion but reduces beyond the optimal χ_o due to O induced effusion. Doublet at 845 cm^{-1} and 890 cm^{-1} shows evidence of low temperature processing. The lines are guides for the eye.

bonding group is not observable, which is similar to other a-SiO_x:H(i) thin films commonly reported in the literature [15, 19, 37]. The Si–C or C–H bonding configuration is also not clearly visible in the spectra due to extremely small inclusion of C atoms in the film [50, 51].

From Figure 4, it can be observed that Si–O–Si stretching peak intensity increases with χ_o . The observed small peak for spectrum with 0 sccm CO_2 flow is probably due to thin native oxide grown on the wafer during transfer. Assuming the peak intensity is proportional to O concentration in the film [38, 52], it can be concluded that the film contains higher O content with increasing CO_2 flow. It is interesting to observe that the Si–O–Si stretching peak at 1107 cm^{-1} becomes more significant with higher χ_o compared to that at 1053 cm^{-1} . Jana et al. [37] and Zhou et al. [15] associate these peaks to Si–H(Si_{3–n}O_n) with $n = 2$ and 1, respectively, according to random bonding model [53]. The increase of peak intensity at 1107 cm^{-1} indicates an increase of Si–H(SiO₂) bonding concentration. The shift of overall Si–O–Si stretching mode to a higher wavenumber is also an indication of higher O content in the film [54, 55]. Therefore, high O content and higher order Si–O–Si bonding configuration resulted in high CO_2 flow condition. The highest O bonding configuration at 1156 cm^{-1} reported by the mentioned groups is not clearly observed even at over 20% CO_2 partial pressure in our case, indicating that Si–H(SiO₂) is the dominant bonding configuration in the χ_o range used in this paper. Notably, two sharp peaks appear at 845 cm^{-1} and 890 cm^{-1} , which are not commonly observed in a-SiO_x:H(i) spectra. This doublet is associated with the polymer chain, (SiH₂)_n, in the film. The appearance of such a doublet is an indicator for low process temperature [38]. Therefore, the lifetime result in this section is much lower than optimized.

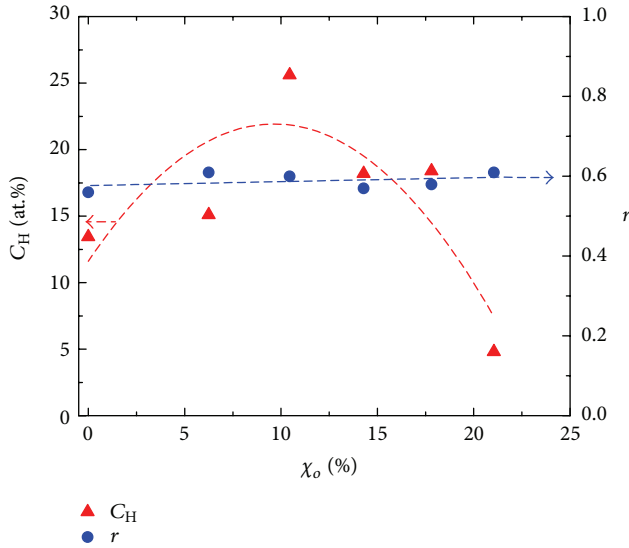


FIGURE 5: C_H and r as functions of χ_o . C_H displays a peak at about 10% CO_2 partial pressure, while r is insensitive to χ_o variation. The lines are guides for the eye.

The peaks at 640 cm^{-1} and 2000 cm^{-1} denote Si–H rocking/wagging and stretching mode [35], respectively. Total H content and bonding configuration can be deduced from these peaks [56]. The results are shown in Figure 5.

It can be observed that C_H inside the film increases with χ_o . Compared with Figure 4, the increase of C_H can be regarded as the result of increasing O content in the film at higher CO_2 flow rate. At the same time, increasing O incorporation does not significantly affect the microstructure factor. Therefore, the improvement of passivation quality is mainly due to the increasing amount of H atoms that can saturate the interface dangling bonds. Indeed, when O content is further increased beyond the optimal point, C_H starts to decrease, leading to a reduction of τ_{eff} . The reduction of C_H could be due to the increased H effusion rate at low temperature as a function of O content in the film. The O cluster formed at higher χ_o induces a void-rich network and promotes the effusion of H atoms [57, 58]. Same fluctuation and reduction of H content with increasing O content was also observed by Janotta et al. [49] and Yun et al. [52]. The direct dependence of passivation quality on C_H indicates that besides impurity incorporation, C_H in a- $\text{SiO}_x\text{:H(i)}$ still dominates the passivation quality, which can be adjusted by χ_o . The same dependence on C_H is also widely observed in a-Si:H(i) [10]. However, higher passivation quality of a- $\text{SiO}_x\text{:H(i)}$ comes from the fact that it has much higher C_H (>20 at.% in our case) compared to that in a-Si:H(i) (12–14 at.%) [16, 59].

3.2.3. Film Composition Analysis. In order to get more insight on the elemental composition of a- $\text{SiO}_x\text{:H(i)}$ films deposited at various χ_o , TOF SIMS analysis was carried out to quantify the depth-resolved concentration for C and O. The results are shown in Figure 6.

Similar to the result obtained by FTIR, O concentration increases with CO_2 partial pressure (cf. Figure 6(a)). The highest O concentration achieved in this work is about $7 \times 10^{20}\text{ cm}^{-3}$, which agrees well with Mueller et al. [16] at a similar CO_2 partial pressure. It should be noted that the uneven distribution of O content throughout the film could be related to the specific depth resolution of SIMS technique used in this paper. The thinness of the film and short deposition duration could also cause such an observation.

Figure 6(b) shows the change of C impurity concentration in the passivation film at different χ_o . C concentration increases at about one order of magnitude for a CO_2 partial pressure change of 20%. C content in this study is slightly higher compared to the result obtained by Mueller et al. [16]. This could be due to the difference in plasma chemistry and reactor design. Nevertheless, the highest C content in the film is only about 0.1 at.%, and it is not sensitive to the change in CO_2 partial pressure. Therefore, the change of H content in the film is the main reason for the change of passivation quality, as concluded in the previous sections.

3.3. Process Temperature

3.3.1. Passivation Quality. In Section 3.2.2, we have shown that the used process temperature is below optimum. Therefore, a scan in process temperature while fixing film thickness at 20 nm and χ_o (10%) at optimum was performed. Other plasma parameters were kept constant. The result for temperature dependent passivation quality is shown in Figure 7.

The temperature process window of a- $\text{SiO}_x\text{:H(i)}$ in ICP system seems to be very wide compared to a-Si:H(i) thin film [12]. For a very broad temperature range (over 200°C), the lifetime stays above 1 ms, demonstrating a very stable process with suppression of epitaxial formation by a- $\text{SiO}_x\text{:H(i)}$ thin film [15, 60]. Despite the stable lifetime, a peak is apparently present near $250\text{--}300^\circ\text{C}$, with a lifetime exceeding 4 ms at about 300°C . The excellent passivation quality is mainly due to a very high H content at the optimal condition.

The initial increase of lifetime is due to better bonding structure benefited from thermal relaxation [42, 61]. Higher temperature releases incorporated H atoms from trapped state (Si– H_2), which is reflected by a reducing r (see Figure 9). These H atoms are mobilized to saturate the interface dangling bonds, thus providing chemical passivation. This phenomenon is further investigated in the following section using FTIR. Once beyond the optimal temperature, the lifetime reduces as a result of H effusion. Indeed, 300°C seems to be the optimal process temperature in our ICP system, which agrees with H effusion temperature reported in the literature [16, 62]. The slightly lower effusion temperature is probably due to the difference in material and deposition technique. The reduction in C_H is the cause of deteriorated passivation quality due to insufficient interface dangling bond saturation.

3.3.2. Bonding Configuration Analysis. In order to understand the temperature dependence of a- $\text{SiO}_x\text{:H(i)}$ passivation, FTIR analysis was carried out. The main features on

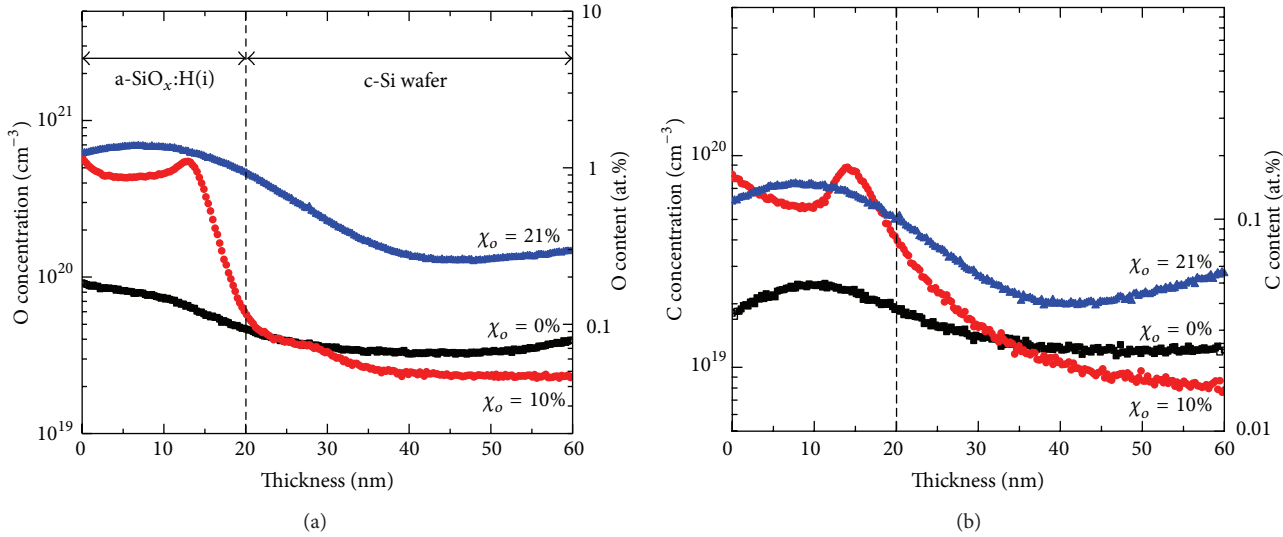


FIGURE 6: Depth resolved (a) O and (b) C concentrations obtained from TOF SIMS. The respective elemental content in a-Si host is calculated based on standard c-Si atomic concentration. Both O and C concentrations show increasing trend with respect to CO₂ partial pressure during deposition. The highest C content achievable in this work is about 0.1 at. %.

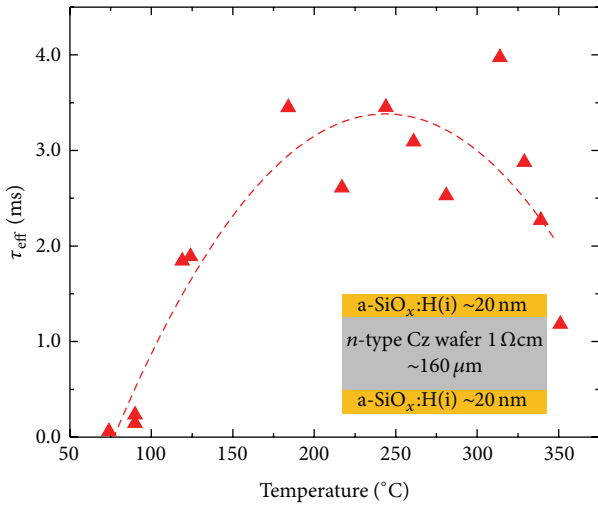


FIGURE 7: Effective lifetime as a function of process temperature. A relatively large process window is observed, which makes the a-SiO_x:H films less sensitive to deposition temperature. The line is a guide to the eye. The inset shows the sample structure for lifetime extraction.

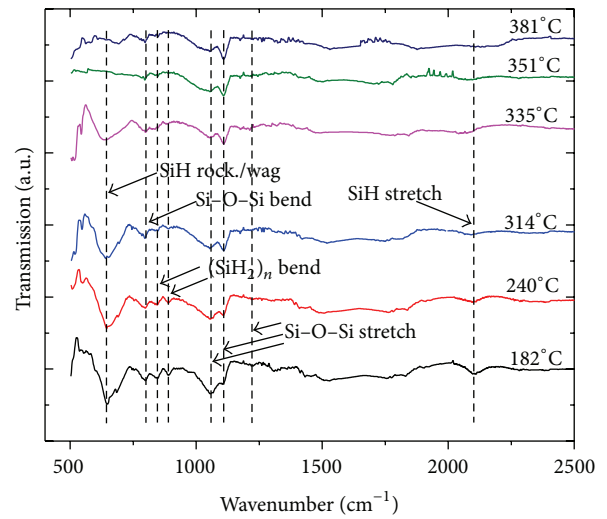


FIGURE 8: FTIR transmission spectra of a-SiO_x:H(i) films with different process temperatures. O in the film tends to be bonded in higher order configuration with increasing temperature. The diminishing peak at 640 cm⁻¹ and 2000 cm⁻¹ indicates the effusion of H atoms. The disappearance of doublet at 845 cm⁻¹ and 890 cm⁻¹ indicates the optimised temperature. The lines are guide to the eye.

FTIR transmission spectra are similar to those shown in Figure 4. The results are illustrated in Figure 8.

The intensity change in Si-O-Si stretching mode peaks with respect to process temperature is not evident, indicating a roughly constant O content in the film throughout the temperature range used. This is reasonable as χ_o is kept constant in this section. However, the shift of O bonding structure to higher order (Si-H(SiO₂)) with temperature is more prominent in this temperature series compared to the previous sections, as evidenced from the heightening and sharpening of the peak at 1107 cm⁻¹. It seems that process

temperature and χ_o has similar effect in altering the bonding configuration inside the film. The shift of Si-O-Si stretching peak position at high temperature is also observed by Yun et al. [52] and is caused by the disproportionation of the reaction chemistry of a-SiO_x:H(i) into a more oxygen-rich suboxide.

In order to find the direct reason for improved lifetime with respect to temperature, C_H and *r* are calculated following the same procedure described in Section 3.2.2. The results are illustrated in Figure 9.

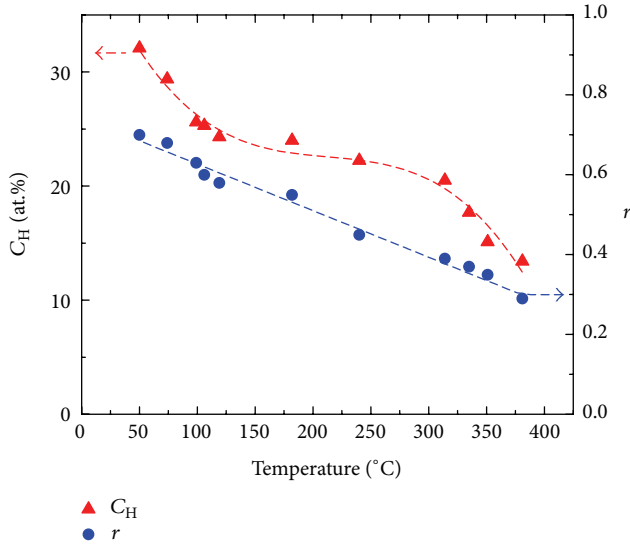


FIGURE 9: C_H and r as functions of temperature. The C_H displays a gradual reduction with a plain over a large span of temperature, resulting in good lifetime with a wide process window. The lines are guides for the eye.

C_H at low temperature is over 30 at.%, indicating a void-rich network with a dominating Si-H₂ bonding configuration. The defective network is also evident from strong (SiH₂)_n doublet peaks at 845 cm⁻¹ and 890 cm⁻¹, similar to those observed in Figure 4. With increasing temperature, C_H reduces in a nonlinear behaviour, showing a plain over a wide range of temperature. At the same time, the intensity of the doublet reduces, indicating a better network structure at elevated temperature. On the other hand, r reduces in a linear manner, indicating a better a-SiO_x:H(i) network with less H clusters and microvoids [42, 61]. The combination of a high C_H due to slow H depletion and an improved amorphous network results in an excellent passivation quality within the process window observed in Figure 7. It is interesting to notice that the sudden reduction of lifetime in Figure 6 coincides with the abrupt loss of H in Figure 9 at around 300°C. As 300°C is close to the commonly reported temperature at which H effusion takes place, the reduction of lifetime beyond the optimal temperature is indeed due to H effusion. Comparing the trend shown in Figures 7 and 9, it can be concluded that the passivation quality of a-SiO_x:H(i) is strongly influenced by C_H in the film, similar to its a-Si:H(i) counterpart. This observation is also intuitive because interface passivation in such samples utilizes H atoms to saturate the dangling bonds as well. Yet, in this study, the apparent large process window in terms of temperature is mainly benefited from the gentle and wide slope that crosses a temperature range of more than 200°C, with a constantly decreasing r . The excellent lifetime at optimal condition is a result of much higher C_H (over 20 at.%) compared to standard a-Si:H(i) thin film [59], as mentioned in Section 3.2.2.

It should be noted that several groups [63, 64] reported improved lifetimes after an H plasma postdeposition treatment with even increasing r . This seems contradictory to our

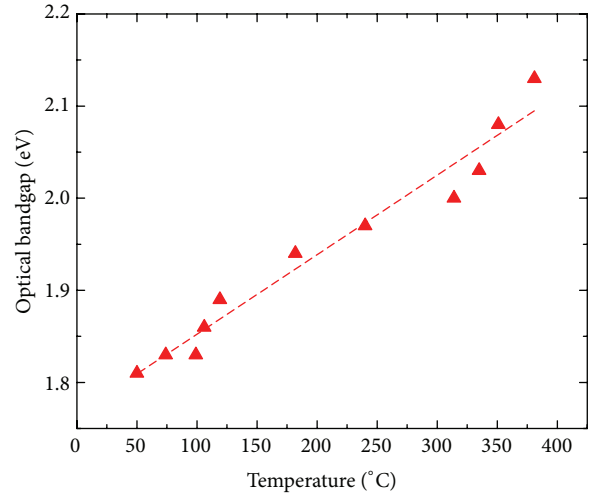


FIGURE 10: Optical bandgap as a function of process temperature. The line is a guide for the eye. A linear dependence of bandgap on temperature can be observed.

finding but can be attributed to greatly increased C_H upon plasma treatment, which diffuses into the interface upon annealing. The improvement of lifetime then cannot be solely explained by the bonding configuration in the amorphous structure. Indeed, the combination of both high C_H and low r in our a-SiO_x:H(i) is the key to such an excellent surface passivation quality, as concluded in the earlier discussion. In case of a-SiO_x:H(i), the use of H plasma treatment is therefore not necessary to achieve high passivation quality due to the inherent high H inclusion of the film.

3.3.3. Optical Property. The optimized a-SiO_x:H(i) has demonstrated excellent passivation properties due to enhanced H content and bonding structure. However, in order to apply the film to HET solar cells, optical properties are equally important. Therefore, Tauc's method [41] was used to find the optical bandgap from SE fitting result. The results are shown in Figure 10.

The optical bandgap increases almost linearly with deposition temperature despite the fact that C_H reduces, as shown in Figure 9. In the case of a-Si:H(i), optical bandgap is positively dependent on C_H in the film [65]. In our case, the contradiction could possibly be explained with an altered O bonding structure. As shown in Figure 8, the elevated temperature shifts the O bonding configuration in a-SiO_x:H(i) thin films to a higher mode and could possibly cause an increase in the stoichiometry parameter x in the a-SiO_x:H(i) film. This change can be one of the reasons for the improved optical bandgap. The optical bandgap at optimal temperature is above 2 eV, which greatly suppresses optical absorption at low wavelengths and improves J_{sc} when applied in HET solar cells.

On the other hand, the film thickness reduces slightly (not shown) with process temperature despite the same deposition time. Since the thickness is obtained from SE fitting, one can argue that the reduction of thickness is due to increased

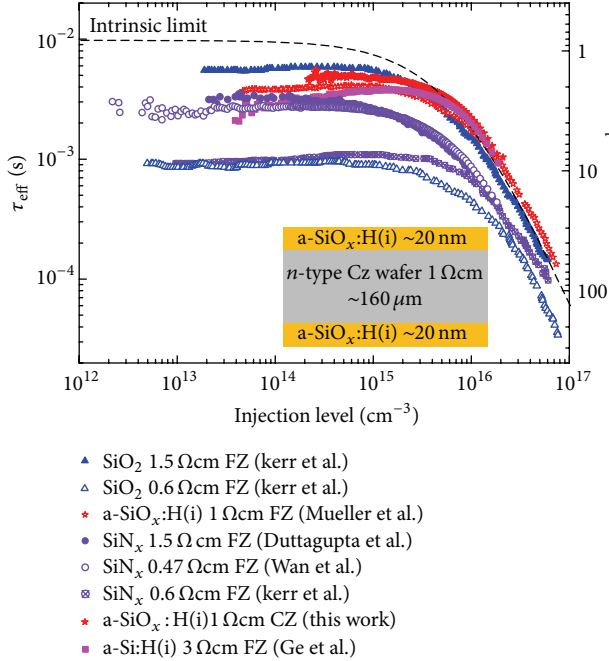


FIGURE 11: Measured QSSPC lifetime of optimized a-SiO_x:H(i) film as a function of minority carrier injection level. The calculation of effective surface recombination velocity is based on wafer thickness of our samples. The dashed line represents intrinsic limit of the 1 Ωcm wafer assuming no extrinsic recombination [27]. As a comparison, other high-quality passivation schemes from Mark and Andres [28, 29], Duttagupta et al. [30], Wan et al. [31], Mueller et al. [16, 18], and Ge et al. [10] are also shown in the graph. The inset shows the sample structure for ICP a-SiO_x:H(i) passivation.

film density at higher temperature. Indeed, the loss of H content and the reduction of microvoid volume (see Figure 9) indicate an optically compact network, therefore causing a reduction in the film thickness. The reduction of thickness also has an impact on the film morphology, altering its crystallinity and optical bandgap as well [66].

3.4. Comparison with Existing Passivation Schemes

3.4.1. Passivation Quality. In order to demonstrate the excellent surface passivation result of the optimized a-SiO_x:H(i) thin film, a comparison in terms of lifetime between our film and some other high-quality passivation schemes was made. The result is shown in Figure 11. By assuming identical surface passivation on both sides of the wafer and sufficiently low surface recombination, the effective surface recombination velocity (S_{eff}) can be related to τ_{eff} using the following relationship:

$$S_{\text{eff}} = \frac{W}{2} \left(\frac{1}{\tau_{\text{eff}}} - \frac{1}{\tau_{\text{bulk}}} \right), \quad (3)$$

where W is the thickness of the wafer and τ_{bulk} represents the bulk lifetime of the wafer, which is a combined result of Auger, radiative, and Shockley-Read-Hall recombination. By further assuming a perfect bulk quality (i.e., $\tau_{\text{bulk}} \rightarrow \infty$), the

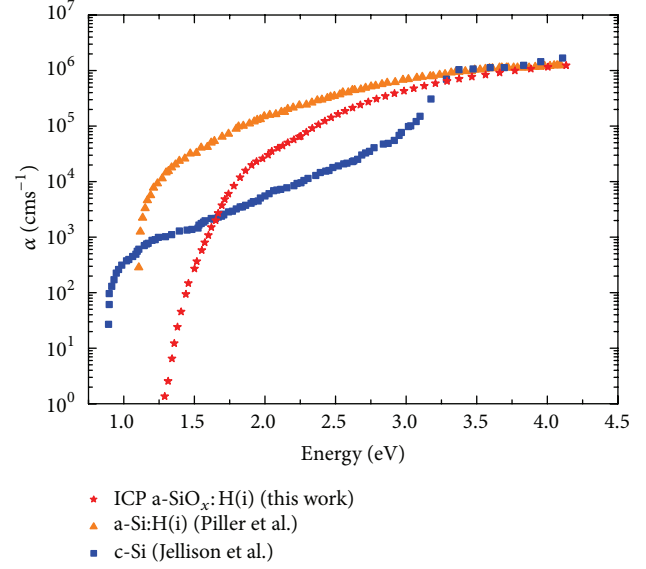


FIGURE 12: Absorption coefficient as a function of photon energy. For comparison, the absorption coefficients of crystalline Si (Jellison 3-1-91) [32] and a-Si:H(i) [33] are shown in the same graph. ICP a-SiO_x:H(i) film shows excellent optical properties compared to a-Si:H(i) throughout the whole wavelength range.

upper limit of S_{eff} can be calculated using (3). From the same equation, it can be shown that the lower the S_{eff} , the better the surface passivation quality.

From Figure 11 it can be concluded that the a-SiO_x:H(i) thin film reported in this paper has similar high-quality passivation quality compared to other schemes, despite the usage of Cz wafers in this work. It should be noted that the reported lifetimes in this work are as-deposited values. Comparing the passivation quality of the a-SiO_x:H(i) film in this work to that of Mueller et al. [16, 18], which appears to be the record lifetime on low-resistivity wafers at the time of reporting, the ICP a-SiO_x:H(i) films deposited in this work yield a slightly better passivation quality which may be attributed to the lower damage remote ICP deposition. The optimized a-SiO_x:H(i) passivation layer features a very high lifetime of over 4.7 ms at an injection level of 10^{15} cm^{-3} with an equivalent S_{eff} of below 1.7 cm s^{-1} and an implied V_{oc} of 741 mV. This passivation quality is excellent considering the wafer type that was used. Therefore, the ICP a-SiO_x:H(i) has demonstrated great potential to be used in HET solar cells.

3.4.2. Optical Properties. As a passivation layer in HET solar cells, the layer should not only have excellent electronic passivation quality but also be highly transparent so as to reduce optical absorption in the layer. The better optical property also allows the use of slightly thicker passivation layer to enhance the passivation quality. Therefore, material with high bandgap with low absorption coefficient is preferred.

We have demonstrated excellent passivation quality of our ICP a-SiO_x:H(i) thin film in the previous section. An ideal bandgap of about 2 eV is also illustrated. A comparison of α of our film and other materials is made in Figure 12.

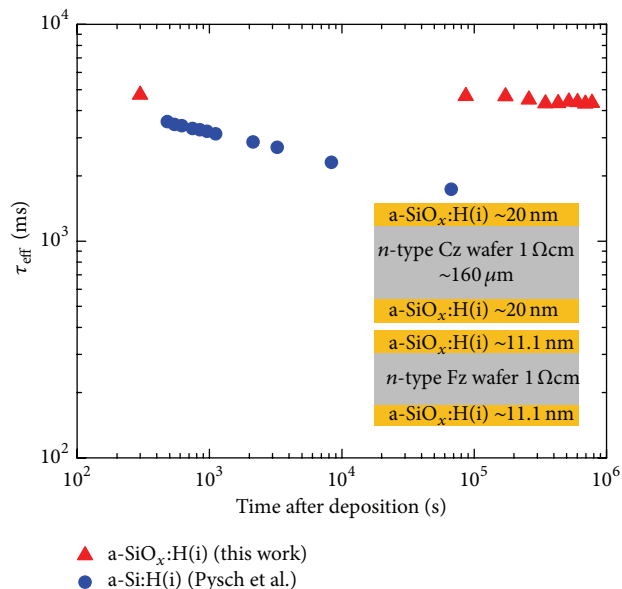


FIGURE 13: Effective lifetime as a function of time after deposition. The insets show sample structures and dimensions for both materials used in the degradation study. The passivation quality of a-SiO_x:H(i) film (20 nm) hardly degrades even after one week of storage. As a comparison, lifetime degradation data of ICP a-Si:H(i) [24] (11.1 nm) is superposed in the same graph. The a-Si:H(i) passivation layer shows constant degradation of lifetime immediately after deposition.

Comparing to the standard a-Si:H(i) film, ICP a-SiO_x:H(i) has much lower α across the whole energy range in Figure 12, showing excellent optical property. This might be due to suppressed band-to-band absorption and subband absorption, benefiting from the high bandgap and the low defect density in the film. Therefore, the ICP a-SiO_x:H(i) deposited in this work has superior optical properties.

3.4.3. Stability. In this section, we investigate the stability of the passivation layer by storing the samples in dark environment and monitoring the passivation quality of the films in regular intervals. The first lifetime measurement was usually conducted two minutes after deposition of the film. The subsequent measurements were made once every 24 hours, throughout a period of one week. The results are shown in Figure 13.

It can be observed that the ICP a-SiO_x:H(i) film (20 nm) in the as-deposited state shows negligible degradation after one week of storage, as reflected by the almost constant τ_{eff} over time. On the other hand, the ICP a-Si:H(i) from Pysch et al. shows severe degradation after two days of storage. The relatively more stable behaviour of ICP a-SiO_x:H(i) might be due to (a) slightly thicker film in this work that shields the delicate interface from the environment and (b) a less sensitive interface against degradation due to the incorporation of O atoms during deposition. Therefore, it can be concluded that the passivation film developed in the present work is robust against degradation caused by exposure to the ambient environment. It should be noted that passivated wafers are

usually sent for subsequent processing (doped layers and TCO depositions) immediately after deposition. Long-time exposure to the ambient environment is rarely observed in industrial processes. Thus, the stable ICP a-SiO_x:H(i) will definitely maintain its excellent passivation quality during the short time periods between the different processes. The same stable behaviour is also reported by Larionova et al. [67], however, only with a SiN_x capping layer.

4. Conclusion

In this paper, we presented a novel passivation scheme featuring low-temperature ICPECVD a-SiO_x:H(i) thin films. By tuning the CO₂ partial pressure and process temperature, the thin film was optimized in terms of passivation and optical quality. An excellent as-deposited lifetime on solar-grade highly doped *n*-type Cz wafers of over 4.7 ms with S_{eff} less than 1.7 cm s⁻¹ was obtained. At the same time, the film also had high bandgap and low absorption, showing excellent optical properties as well. Comparing to typically used a-Si:H(i), the ICP a-SiO_x:H(i) shows superior stability against degradation after being exposed to ambient environment. We propose the ICP a-SiO_x:H(i) as an alternative candidate for high-quality surface passivation layers in HET solar cell applications.

Conflict of Interests

The authors declare that there is no conflict of interests regarding the publication of this paper.

Acknowledgments

The Solar Energy Research Institute of Singapore is sponsored by the National University of Singapore (NUS) and Singapore's National Research Foundation (NRF) through the Singapore Economic Development Board (EDB). This research is supported by the National Research Foundation, Prime Minister's Office, Singapore under its Clean Energy Research Programme (CERP Award no. NRF2010EWT-CERP001-022).

References

- [1] M. Taguchi, A. Yano, S. Tohoda et al., "24.7% record efficiency HIT solar cell on thin silicon wafer," *IEEE Journal of Photovoltaics*, vol. 99, pp. 1–4, 2013.
- [2] M. Taguchi, Y. Tsunomura, H. Inoue et al., "High-efficiency HIT solar cell on thin (<100 μm) silicon wafer," in *Proceedings of the 24th European Photovoltaic Solar Energy Conference*, pp. 1690–1693, 2009.
- [3] Y. Tsunomura, Y. Yoshimine, M. Taguchi et al., "Twenty-two percent efficiency HIT solar cell," *Solar Energy Materials and Solar Cells*, vol. 93, no. 6–7, pp. 670–673, 2009.
- [4] J.-W. A. Schttauf, K. H. M. van der Werf, I. M. Kielen, W. G. J. H. M. van Sark, J. K. Rath, and R. E. I. Schropp, "High quality crystalline silicon surface passivation by combined intrinsic and *n*-type hydrogenated amorphous silicon," *Applied Physics Letters*, vol. 99, no. 20, Article ID 203503, 2011.

- [5] M. Taguchi, K. Kawamoto, S. Tsuge et al., "HIT cells-high-efficiency crystalline Si cells with novel structure," *Progress in Photovoltaics: Research and Applications*, vol. 8, pp. 503–513, 2000.
- [6] M. Tanaka, M. Taguchi, T. Matsuyama et al., "Development of new a-Si/c-Si heterojunction solar cells: ACJ-HIT (Artificially Constructed Junction-Heterojunction with Intrinsic Thin-layer)," *Japanese Journal of Applied Physics*, vol. 31, no. 11, pp. 3518–3522, 1992.
- [7] J. I. Pankove and M. L. Tarnag, "Amorphous silicon as a passivant for crystalline silicon," *Applied Physics Letters*, vol. 34, no. 2, pp. 156–157, 1979.
- [8] M. Taguchi, A. Terakawa, E. Maruyama, and M. Tanaka, "Obtaining a higher voc in HIT cells," *Progress in Photovoltaics: Research and Applications*, vol. 13, no. 6, pp. 481–488, 2005.
- [9] K. Wakisaka, M. Taguchi, T. Sawada et al., "More than 16% solar cells with a new "HIT" (doped a-Si/non-doped a-Si/crystalline Si) structure," in *Proceedings of the IEEE Photovoltaic Specialists Conference*, pp. 887–892, October 1991.
- [10] J. Ge, Z. P. Ling, J. Wong, T. Mueller, and A. G. Aberle, "Optimisation of Intrinsic a-Si:H passivation layers in crystalline-amorphous silicon heterojunction solar cells," *Energy Procedia*, vol. 15, pp. 107–117, 2012.
- [11] J. Ge, Z. P. Ling, J. Wong, R. Stangl, A. G. Aberle, and T. Mueller, "Analysis of intrinsic hydrogenated amorphous silicon passivation layer growth for use in heterojunction silicon wafer solar cells by optical emission spectroscopy," *Journal of Applied Physics*, vol. 113, no. 23, Article ID 234310, 2013.
- [12] H. Fujiwara and M. Kondo, "Impact of epitaxial growth at the heterointerface of solar cells," *Applied Physics Letters*, vol. 90, Article ID 013503, 2007.
- [13] U. Kroll, J. Meier, P. Torres, J. Pohl, and A. Shah, "From amorphous to microcrystalline silicon films prepared by hydrogen dilution using the VHF (70 MHz) GD technique," *Journal of Non-Crystalline Solids*, vol. 227–230, part 1, pp. 68–72, 1998.
- [14] S. de Wolf and M. Kondo, "Abruptness of interface revealed by carrier lifetime measurements," *Applied Physics Letters*, vol. 90, Article ID 042111, 2007.
- [15] H. P. Zhou, D. Y. Wei, S. Xu et al., "Si surface passivation by $\text{SiO}_x\text{:H}$ films deposited by a low-frequency ICP for solar cell applications," *Journal of Physics D: Applied Physics*, vol. 45, Article ID 395401, 2012.
- [16] T. Mueller, S. Schwertheim, and W. R. Fahrner, "Crystalline silicon surface passivation by high-frequency plasma-enhanced chemical-vapor-deposited nanocomposite silicon suboxides for solar cell applications," *Journal of Applied Physics*, vol. 107, no. 1, Article ID 014504, 2010.
- [17] G.-Z. Jia, H.-G. Liu, and H.-D. Chang, "PECVD amorphous silicon suboxide films for surface passivation of silicon solar cells," in *Proceedings of the 10th IEEE International Conference on Solid-State and Integrated Circuit Technology*, pp. 2013–2015, November 2010.
- [18] T. Mueller, S. Schwertheim, M. Scherff, and W. R. Fahrner, "High quality passivation for heterojunction solar cells by hydrogenated amorphous silicon suboxide films," *Applied Physics Letters*, vol. 92, no. 3, Article ID 033504, 2008.
- [19] B. Hoex, F. J. J. Peeters, M. Creatore, M. A. Blauw, W. M. M. Kessels, and M. C. M. van de Sanden, "High-rate plasma-deposited SiO_2 films for surface passivation of crystalline silicon," *Journal of Vacuum Science and Technology A: Vacuum, Surfaces and Films*, vol. 24, no. 5, pp. 1823–1830, 2006.
- [20] S. Schwertheim, M. Scherff, T. Mueller, W. R. Fahrner, and H. C. Neitzert, "Lead-free electrical conductive adhesives for solar cell interconnectors," in *Proceedings of the 33rd IEEE Photovoltaic Specialists Conference, PVSC 2008*, pp. 1–6, May 2008.
- [21] T. Mueller, W. Duengen, R. Job, M. Scherff, and W. Fahrner, "Crystalline silicon surface passivation by PECV-deposited hydrogenated amorphous silicon oxide films [$\text{a-SiO}_x\text{:H}$]," in *MRS Online Proceedings Library*, vol. 989, pp. 75–80, April 2007.
- [22] S. Q. Xiao, S. Xu, H. P. Zhou et al., "Amorphous/crystalline silicon heterojunction solar cells via remote inductively coupled plasma processing," *Applied Physics Letters*, vol. 100, no. 23, Article ID 233902, 2012.
- [23] J. Li, J. Wang, M. Yin et al., "Deposition of controllable preferred orientation silicon films on glass by inductively coupled plasma chemical vapor deposition," *Journal of Applied Physics*, vol. 103, Article ID 043505, 2008.
- [24] D. Pysch, M. Bivour, K. Zimmermann, C. Schetter, M. Hermle, and S. W. Glunz, "Comprehensive study of different PECVD deposition methods for deposition of thin intrinsic amorphous silicon for heterojunction solar cells," in *Proceedings of the 24th European Photovoltaic Solar Energy Conference*, pp. 1580–1585, 2009.
- [25] Z. Zhang, T. Dippell, M. Huber et al., "SINGULAR platform for dual-sided plasma treatment and coating of Si-based passivation layers," in *Proceedings of the 29th European Photovoltaic Solar Energy Conference*, 2014.
- [26] J. Ge, M. Tang, J. Wong et al., "State-of-the-art amorphous silicon sub-oxide passivation layer by ICPECVD for heterojunction solar cell applications," in *Proceedings of the 29th European Photovoltaic Solar Energy Conference*, 2014.
- [27] A. Richter, F. Werner, A. Cuevas, J. Schmidt, and S. W. Glunz, "Improved parameterization of auger recombination in silicon," *Energy Procedia*, vol. 27, pp. 88–94, 2012.
- [28] J. K. Mark and C. Andres, "Very low bulk and surface recombination in oxidized silicon wafers," *Semiconductor Science and Technology*, vol. 17, p. 35, 2002.
- [29] J. K. Mark and C. Andres, "Recombination at the interface between silicon and stoichiometric plasma silicon nitride," *Semiconductor Science and Technology*, vol. 17, p. 166, 2002.
- [30] S. Duttagupta, F. Lin, M. Wilson, M. B. Boreland, B. Hoex, and A. G. Aberle, "Extremely low surface recombination velocities on low-resistivity *n*-type and *p*-type crystalline silicon using dynamically deposited remote plasma silicon nitride films," *Progress in Photovoltaics: Research and Applications*, vol. 22, no. 6, pp. 641–647, 2012.
- [31] Y. Wan, K. R. McIntosh, A. F. Thomson, and A. Cuevas, "Low surface recombination velocity by low-absorption silicon nitride on c-Si," *IEEE Journal of Photovoltaics*, vol. 3, no. 1, pp. 554–559, 2013.
- [32] G. E. Jellison Jr., "Optical functions of GaAs, GaP, and Ge determined by two-channel polarization modulation ellipsometry," *Optical Materials*, vol. 1, no. 3, pp. 151–160, 1992.
- [33] H. Piller, *Handbook of Optical Constants of Solids*, vol. 1, 1985.
- [34] C. T. Kirk, "Quantitative analysis of the effect of disorder-induced mode coupling on infrared absorption in silica," *Physical Review B*, vol. 38, pp. 1255–1273, 1988.
- [35] L. He, Y. Kurata, T. Inokuma, and S. Hasegawa, "Analysis of SiH vibrational absorption in amorphous $\text{SiO}_x\text{:H}$ ($0 \leq x \leq 2.0$) alloys in terms of a charge-transfer model," *Applied Physics Letters*, vol. 63, no. 2, pp. 162–164, 1993.

- [36] M. H. Brodsky, M. Cardona, and J. J. Cuomo, "Infrared and Raman spectra of the silicon-hydrogen bonds in amorphous silicon prepared by glow discharge and sputtering," *Physical Review B*, vol. 16, no. 8, pp. 3556–3571, 1977.
- [37] T. Jana, S. Mukhopadhyay, and S. Ray, "Low temperature silicon oxide and nitride for surface passivation of silicon solar cells," *Solar Energy Materials and Solar Cells*, vol. 71, no. 2, pp. 197–211, 2002.
- [38] G. Lucovsky, J. Yang, S. S. Chao, J. E. Tyler, and W. Czubytyj, "Oxygen-bonding environments in glow-discharge-deposited amorphous silicon-hydrogen alloy films," *Physical Review B*, vol. 28, no. 6, pp. 3225–3233, 1983.
- [39] H. Nagel, C. Berge, and A. G. Aberle, "Generalized analysis of quasi-steady-state and quasi-transient measurements of carrier lifetimes in semiconductors," *Journal of Applied Physics*, vol. 86, no. 11, pp. 6218–6221, 1999.
- [40] G. E. Jellison Jr. and F. A. Modine, "Parameterization of the optical functions of amorphous materials in the interband region," *Applied Physics Letters*, vol. 69, no. 3, pp. 371–373, 1996.
- [41] J. Tauc, "Optical properties and electronic structure of amorphous Ge and Si," *Materials Research Bulletin*, vol. 3, pp. 37–46, 1968.
- [42] T. F. Schulze, H. N. Beushausen, C. Leendertz, A. Dobrich, B. Rech, and L. Korte, "Interplay of amorphous silicon disorder and hydrogen content with interface defects in amorphous/crystalline silicon heterojunctions," *Applied Physics Letters*, vol. 96, no. 25, Article ID 252102, 2010.
- [43] J. K. Rath, R. E. I. Schropp, and W. Beyer, "Hydrogen at compact sites in hot-wire chemical vapour deposited polycrystalline silicon films," *Journal of Non-Crystalline Solids*, vol. 266–269, pp. 190–194, 2000.
- [44] D. Gracin, U. Desnica, and M. Ivanda, "Microstructural properties of dc magnetron sputtered a-Si:H by IR spectroscopy," *Journal of Non-Crystalline Solids*, vol. 149, no. 3, pp. 257–263, 1992.
- [45] A. H. M. Smets, W. M. M. Kessels, and M. C. M. van de Sanden, "Vacancies and voids in hydrogenated amorphous silicon," *Applied Physics Letters*, vol. 82, no. 10, pp. 1547–1549, 2003.
- [46] Z. Remeš, M. Vaněček, A. H. Mahan, and R. S. Crandall, "Silicon network relaxation in amorphous hydrogenated silicon," *Physical Review B*, vol. 56, pp. R12710–R12713, 1997.
- [47] Z. Remeš, M. Vaněček, P. Torres, U. Kroll, A. H. Mahan, and R. S. Crandall, "Optical determination of the mass density of amorphous and microcrystalline silicon layers with different hydrogen contents," *Journal of Non-Crystalline Solids*, vol. 227–230, part 2, pp. 876–879, 1998.
- [48] D. Pysch, C. Meinhardt, K.-U. Ritzau et al., "Comparison of intrinsic amorphous silicon buffer layers for silicon heterojunction solar cells deposited with different PECVD techniques," in *Proceedings of the 35th IEEE Photovoltaic Specialists Conference (PVSC '10)*, pp. 3570–3576, June 2010.
- [49] A. Janotta, R. Janssen, M. Schmidt et al., "Doping and its efficiency in a-SiO_x:H," *Physical Review B*, vol. 69, p. 115206, 2004.
- [50] A. Grill and D. A. Neumayer, "Structure of low dielectric constant to extreme low dielectric constant SiCOH films: Fourier transform infrared spectroscopy characterization," *Journal of Applied Physics*, vol. 94, no. 10, pp. 6697–6707, 2003.
- [51] D. M. Wolfe, B. J. Hinds, F. Wang et al., "Thermochemical stability of silicon-oxygen-carbon alloy thin films: a model system for chemical and structural relaxation at SiC-SiO₂ interfaces," *Journal of Vacuum Science and Technology A*, vol. 17, no. 4, pp. 2170–2177, 1999.
- [52] F. Yun, B. J. Hinds, S. Hatatani, S. Oda, Q. X. Zhao, and M. Willander, "Study of structural and optical properties of nanocrystalline silicon embedded in SiO₂," *Thin Solid Films*, vol. 375, no. 1-2, pp. 137–141, 2000.
- [53] H. R. Philipp, "Optical and bonding model for non-crystalline SiO_x and SiO_xNy materials," *Journal of Non-Crystalline Solids*, vol. 8–10, pp. 627–632, 1972.
- [54] D. V. Tsu, G. Lucovsky, and B. N. Davidson, "Effects of the nearest neighbors and the alloy matrix on SiH stretching vibrations in the amorphous SiO_r:H (0 < r < 2) alloy system," *Physical Review B*, vol. 40, no. 3, pp. 1795–1805, 1989.
- [55] P. G. Pai, S. S. Chao, Y. Takagi, and G. Lucovsky, "Infrared spectroscopic study of SiO_x films produced by plasma enhanced chemical vapor deposition," *Journal of Vacuum Science and Technology A*, vol. 4, pp. 689–694, 1986.
- [56] H. Shanks, C. J. Fang, L. Ley, M. Cardona, F. J. Desmond, and S. Kalbitzer, "Infrared spectrum and structure of hydrogenated amorphous silicon," *Physica Status Solidi B*, vol. 100, no. 1, pp. 43–56, 1980.
- [57] F. Einsele, W. Beyer, and U. Rau, "Infrared spectrum and structure of hydrogenated amorphous silicon," *Journal of Applied Physics*, vol. 112, Article ID 054905, 2012.
- [58] W. Beyer, "Infrared absorption and hydrogen effusion of hydrogenated amorphous silicon-oxide films," *Journal of Non-Crystalline Solids*, vol. 266–269, part 2, pp. 845–849, 2000.
- [59] R. Janssen, A. Janotta, D. Dimova-Malinovska, and M. Stutzmann, "Optical and electrical properties of doped amorphous silicon suboxides," *Physical Review B*, vol. 60, no. 19, pp. 13561–13572, 1999.
- [60] H. Fujiwara, T. Kaneko, and M. Kondo, "Application of hydrogenated amorphous silicon oxide layers to Si heterojunction solar cells," *Applied Physics Letters*, vol. 91, Article ID 133508, 2007.
- [61] M. Jeon, S. Yoshida, and K. Kamisako, "Hydrogenated amorphous silicon film as intrinsic passivation layer deposited at various temperatures using RF remote-PECVD technique," *Current Applied Physics*, vol. 10, no. 2, pp. S237–S240, 2010.
- [62] M. Park, C. W. Teng, V. Sakhrani et al., "Optical characterization of wide band gap amorphous semiconductors (a-Si:C:H): effect of hydrogen dilution," *Journal of Applied Physics*, vol. 89, no. 2, pp. 1130–1137, 2001.
- [63] M. Mews, T. F. Schulze, N. Mingirulli, and L. Korte, "Hydrogen plasma treatments for passivation of amorphous-crystalline silicon-heterojunctions on surfaces promoting epitaxy," *Applied Physics Letters*, vol. 102, no. 12, Article ID 122106, 2013.
- [64] A. Descoedres, L. Barraud, S. de Wolf et al., "Improved amorphous/crystalline silicon interface passivation by hydrogen plasma treatment," *Applied Physics Letters*, vol. 99, no. 12, Article ID 123506, 2011.
- [65] G. D. Cody, C. R. Wronski, B. Abeles, R. B. Stephens, and B. Brooks, "Optical characterization of amorphous silicon hydride films," *Solar Cells*, vol. 2, no. 3, pp. 227–243, 1980.
- [66] G. M. Ferreira, C. Chen, R. J. Koval, J. M. Pearce, C. R. Wronski, and R. W. Collins, "Optimization of protocrystalline silicon p-type layers for amorphous silicon n-i-p solar cells," *Journal of Non-Crystalline Solids*, vol. 338–340, no. 1, pp. 694–697, 2004.
- [67] Y. Larionova, V. Mertens, N.-P. Harder, and R. Brendel, "Surface passivation of n-type Czochralski silicon substrates by thermal-SiO₂/plasma-enhanced chemical vapor deposition SiN stacks," *Applied Physics Letters*, vol. 96, no. 3, Article ID 032105, 2010.

Research Article

Ultrathin Anode Buffer Layer for Enhancing Performance of Polymer Solar Cells

Dun Wang,¹ Jian Wang,¹ Ling-liang Li,¹ Qiao-shi An,¹ Hui Huang,²
Chao-qun Jiao,² Yang Liu,¹ and Fu-jun Zhang¹

¹ Key Laboratory of Luminescence and Optical Information, Ministry of Education, Beijing Jiaotong University, Beijing 100044, China

² School of Electrical Engineering, Beijing Jiaotong University, Beijing 100044, China

Correspondence should be addressed to Fu-jun Zhang; fjzhang@bjtu.edu.cn

Received 23 April 2014; Accepted 11 May 2014; Published 28 May 2014

Academic Editor: Dewei Zhao

Copyright © 2014 Dun Wang et al. This is an open access article distributed under the Creative Commons Attribution License, which permits unrestricted use, distribution, and reproduction in any medium, provided the original work is properly cited.

A series of polymer solar cells (PSCs) based on poly[(4,8-bis-(2-ethylhexyloxy)-benzo[1,2-b:4,5-b']dithiophene)-2,6-diyl-alt-(4-(2-ethylhexanoyl)-thieno[3,4-b]thiophene)-2,6-diyl] (PBDDTTT-C) and [6,6]phenyl-C71-butyric acid methyl ester (PC₇₁BM) were fabricated with various anode buffer layers. The power conversion efficiency (PCE) of PSCs was improved to 4.91% for the cells with PEDOT:PSS/LiF (1 nm) as anode buffer layer, which corresponds to 26.2% efficiency improvement compared with the cells with PEDOT:PSS as anode buffer layer. The PSCs with PEDOT:PSS/LiF as anode buffer layer show a maximum short-circuit density (J_{sc}) of 13.70 mA/cm², with open circuit voltage (V_{oc}) of 0.73 V and fill factor (FF) of 49.1% under illumination 100 mW/cm² AM 1.5 G simulated solar light. The dominant mechanism for the performance improvement of PSCs could be attributed to the increased charge carrier collection ability by anode buffer layers.

1. Introduction

In the past ten years, as the demand for renewable energy becomes more and more urgent, polymer solar cells (PSCs) have been considered as next generation photovoltaic devices to solve energy crisis due to its many advantages, such as flexibility, light weight, environmental friendly, and easy large-area applications [1]. Many strategies have been introduced on improving the power conversion efficiency (PCE) and stability of PSCs, such as the development of novel donor and acceptor materials [2], the novel processing approaches to induce optimal microstructures in the active layer [3], and the optimization of interfacial buffer layer for efficient charge carriers collection [4]. The PCE of PSCs has been improved to more than 6% with a narrow band gap polymer poly[(4,8-bis-(2-ethylhexyloxy)-benzo[1,2-b:4,5-b']dithiophene)-2,6-diyl-alt-(4-(2-ethylhexanoyl)-thieno[3,4-b]thiophene)-2,6-diyl] (PBDDTTT-C). The key requirement for efficient operation of all-organic electronic devices is the process of the charge carriers injection and collection between active layer and electrodes. Therefore, the

optimization of interfacial buffer layer is required to form ohmic contact for better charge carriers collection, resulting in increased short-circuit current density (J_{sc}) and fill factor (FF) of PSCs.

It is known that anode buffer layer plays an important role in determining the performance of organic light emitting diodes (OLEDs) and the PSCs. The operation mechanism of anode buffer layer is more complex in real PSCs. The main mechanism can be summarized as follows: (i) to adjust the effective work function of the electrode [5], (ii) to realize a vacuum level offset between the active layer and the electrode by forming a dipole layer [6], (iii) to increase built-in electric field by forming a tunneling junction [7], and (iv) to protect organic active layer from the hot electrode atoms during thermal deposition [8]. Helander et al. reported that the alkali halide (typically LiF in combination with an Al cathode) inserted between electrodes and the active layer can form a dipolar salt layer, then reducing the electron-injection barriers or extraction losses in the PSCs [9, 10]. As we know, poly(3,4-ethylenedioxythiophene):poly(styrenesulfonate) (PEDOT:PSS) is commonly

used as anode buffer layer to enhance J_{sc} as well as open circuit voltage (V_{oc}) for PSCs. PEDOT:PSS consists of PSS, which has hygroscopic and acidic characteristics. The PSS can corrode ITO and set off chemical reaction with the active layer materials, which degrades the cell performance [11]. In order to solve this problem, the metal oxides of zinc oxide (ZnO) [12], nickel oxide (NiO) [13], molybdenum oxide (MoO_3) [14, 15], and tungsten oxide (WO_3) [16] have been demonstrated as an effective replacement of PEDOT:PSS to improve the stability of PSCs. However, it is difficult to control the work function of the metal oxides for desired applications [17]. Recently, Chen et al. reported that solution-processed MoO_3 doped into PEDOT:PSS extends the interfacial contact area between the active layer and PEDOT:PSS layer, which facilitates hole collection at the anode; the performance and stability of the PSCs were improved [18]. In this paper, we reported the effects of PEDOT:PSS/LiF as anode buffer layer on the performance of PSCs. The PCE of PSCs was improved to 4.91% with a PEDOT:PSS/LiF (1 nm) double anode buffer layer system, which leads to a significant efficiency improvement of about 26.2% compared with a single PEDOT:PSS buffer layer. The optimized PSCs have J_{sc} of 13.70 mA/cm^2 , with V_{oc} of 0.73 V and FF of 49.1% under illumination 100 mW/cm^2 AM 1.5 G simulated solar light.

2. Experimental Section

The indium tin oxide (ITO) glass substrates with sheet resistance $15 \Omega/\square$ were cleaned continuously in ultrasonic baths containing acetone, detergent, deionized water, and ethanol. Then the cleaned ITO substrates were blow-dried by high pure nitrogen gas and then treated by UV-ozone for 10 minutes to increase the work function of ITO. The solution of PEDOT:PSS (Clevios PVP Al 4083, purchased from H.C. Starck co. Ltd.) was spin-coated onto the cleaned ITO substrates under 5000 rounds per minute (RPM) for 40 s to fabricate the interfacial layers. Then PEDOT:PSS coated ITO glass substrates were annealed in air at 120°C . After drying for 10 minutes, the substrates were transferred to a nitrogen-filled glove box. The polymer material PBDTTT-C (Product number: SMI-P9001, purchased from Solarmer Energy, Inc.) and [6,6]phenyl- C_{71} -butyric acid methyl ester ($PC_{71}BM$) (Product number: LT-S923, purchased from Luminescence Technology Corp) with a weight ratio of 1:1.5 were dissolved in 1,2-dichlorobenzene at a concentration of 25 mg/mL . The blend solution was stirred by a magnetic stirrer at 27°C for 24 hours; then the active layers were fabricated by spin-coating method at rate of 1400 RPM in a high purity nitrogen filled glove box. The 1 nm LiF interfacial layer and about 100 nm cathode layer Al were deposited by thermal evaporation under 10^{-4} Pa vacuum conditions, and the thickness was monitored by a quartz crystal microbalance. The active area of about 3.8 mm^2 is defined by the vertical overlap of ITO anode and Al cathode. The cell architecture is ITO/buffer layer/PBDTTT-C: $PC_{71}BM$ /LiF/Al. For convenient comparison, the PSCs with various anode buffer layers were marked by Cells A to D:

Cells A: Glass/ITO/PBDTTT-C: $PC_{71}BM$ /LiF/Al,

Cells B: Glass/ITO/LiF (1 nm)/PBDTTT-C: $PC_{71}BM$ /LiF/Al,

Cells C: Glass/ITO/PEDOT:PSS/PBDTTT-C: $PC_{71}BM$ /LiF/Al,

Cells D: Glass/ITO/PEDOT:PSS/LiF (1 nm)/PBDTTT-C: $PC_{71}BM$ /LiF/Al.

The absorption spectra of films were measured with a Shimadzu UV-3101 PC spectrophotometer. The current density-voltage (J - V) characteristics of the PSCs were measured using a Keithley 4200 source measurement unit and an ABET Sun 2000 solar simulator at room temperature in air. The external quantum efficiency (EQE) spectra were measured by a Zolix Solar Cell Scan 100. The schematic architecture of the PSCs, the molecular structures of PBDTTT-C and $PC_{71}BM$, and the energy level structure are shown in Figure 1.

3. Results and Discussion

The normalized absorption spectra of pure PBDTTT-C and $PC_{71}BM$ films and their blend films (1:1.5) were measured and are shown in Figure 2. It is apparent that pure PBDTTT-C films show a relatively strong absorption in the range from 600 nm to 750 nm and a relative weak absorption in the shorter wavelength range from 350 nm to 600 nm. The main absorption peak of PBDTTT-C locates at 700 nm. The highest occupied molecular orbital (HOMO) and the lowest unoccupied molecular orbital (LUMO) levels of PBDTTT-C are 5.12 eV and 3.35 eV, with the band gap of about 1.77 eV according to the absorption peak at about 700 nm [19]. There are two apparent absorption peaks at 375 nm and 480 nm for pure $PC_{71}BM$ films, which could broaden light absorption range of the blend films. Therefore, the normalized absorption spectrum of blend films shows two distinct absorption peaks at 460 nm and 700 nm, resulting from their absorption spectral overlap. Based on the PBDTTT-C: $PC_{71}BM$ as the active layers, a series of PSCs with various anode buffer layers were fabricated and measured under the same conditions.

The current density-voltage (J - V) characteristic curves of PSCs were measured under dark conditions and are shown in Figure 3(a). It is apparent that Cells B, C, and D with anode buffer layers have lower leak current densities under reverse bias, compared with that of Cells A prepared on bare ITO substrates. This indicates that anode buffer layers could improve the interface between the ITO anode and the active layer. Cells D with PEDOT:PSS/LiF as anode buffer layer show the best diode quality with lower leak current density and high rectification ratio; the rectification ratio $|J(1v)|/|J(-1v)|$ is as high as $\sim 10^4$.

The J - V characteristic curves of PSCs with various anode buffer layers were measured under illumination 100 mW/cm^2 AM 1.5 G simulated solar light and are shown in Figure 3(b). The key parameters of PSCs are summarized in Table 1. It is apparent that Cells D have relatively larger V_{oc} than those of Cells A and B, and the V_{oc} of Cells D remain almost the same compared with that of Cells C. As we know V_{oc} of PSCs is primarily determined by two factors: (i) the energy levels difference between the HOMO

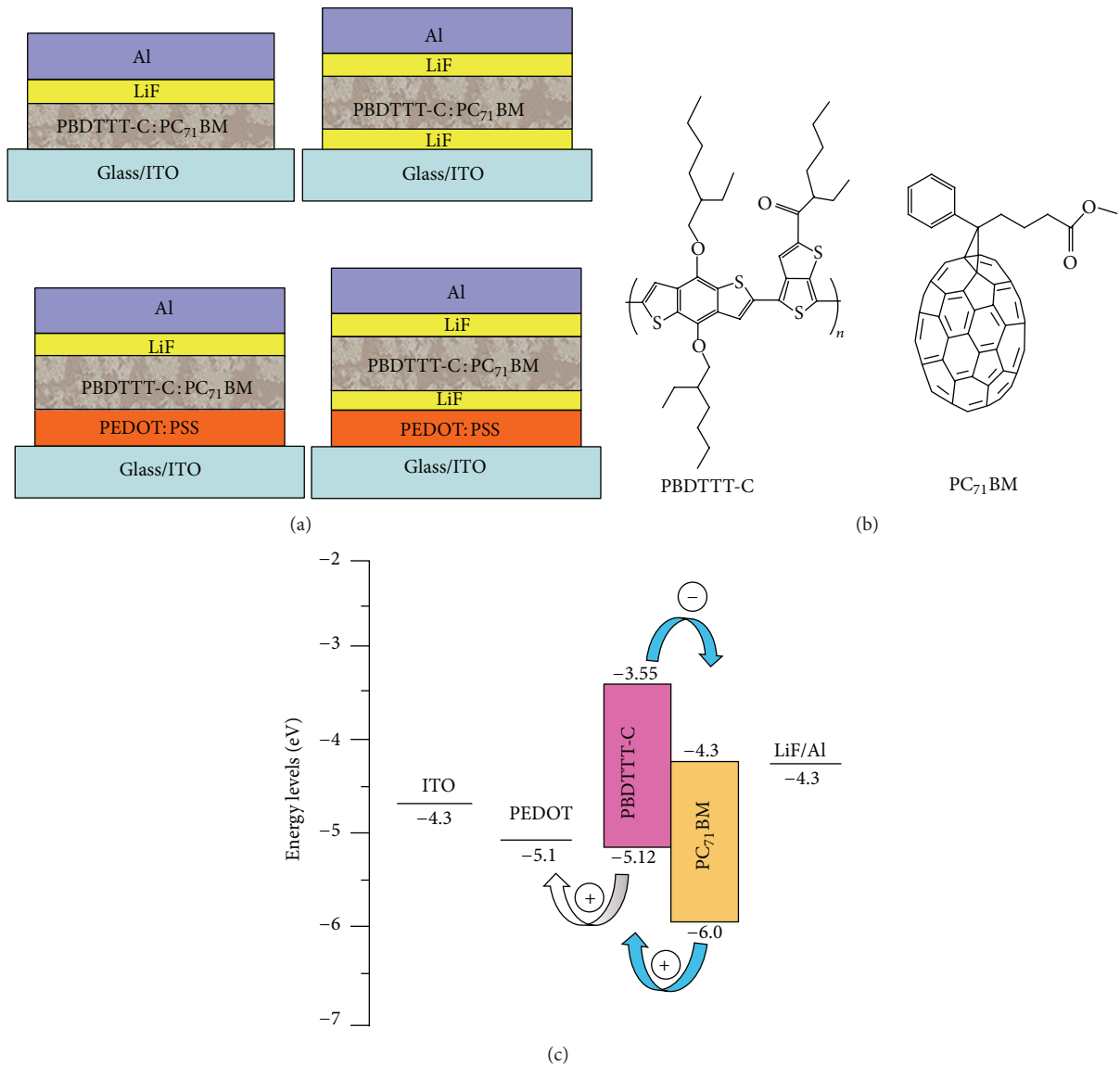


FIGURE 1: (a) The schematic architecture of the PSCs. (b) Molecular structure of PBDTTT-C and PC₇₁BM. (c) The energy level structure of materials.

of the electron donor and the LUMO of electron acceptor and (ii) the work function difference between anode and cathode electrode [20]. It could be assumed that the improved V_{oc} of Cells D was due to the changes of anode work function since the active layer fabrication condition and the cathode layer deposition remain constant. The work function of PEDOT:PSS (5.1 eV) is 0.4 eV higher than that of ITO (4.7 eV). The PEDOT:PSS layer can effectively tune the work function of ITO substrates for Cells C and D. According to the V_{oc} of Cells C and D, the thin LiF layer may have no obvious effect on the work function of ITO substrates. It is worthwhile to mention that the J_{sc} of Cells D is 13.70 mA/cm², which is a 14.4% increase compared with that of Cells C. The increase of J_{sc} could be attributed to the enhancement of holes extraction efficiency by the ultrathin anode buffer layer. It is known that PEDOT:PSS is conductive polymer

with high ductility, which could be considered as a kind of metal. The metal-insulator-semiconductor (MIS) model could be formed, which is based on PEDOT:PSS/LiF/organic active layer, because LiF and organic active layer materials are commonly considered as insulator and semiconductor, respectively. As reported by Xi et al. when the generated holes in the active layer come to the interface of LiF/organic active layer, a large number of them will pass through the ultrathin LiF layer by the tunneling [21]. The FF of Cells D is increased about 10.3% compared with that of Cells C. This may be due to the improved interfacial contact between the active layer and PEDOT:PSS layer due to the insertion of a thin LiF layer. Kim and Chang reported that a thin LiF layer evaporated onto PEDOT:PSS layer could reduce film roughness, which shows smooth surface morphology of the anode buffer layer [22]. It is known that the shunt resistance (R_{sh}) and series

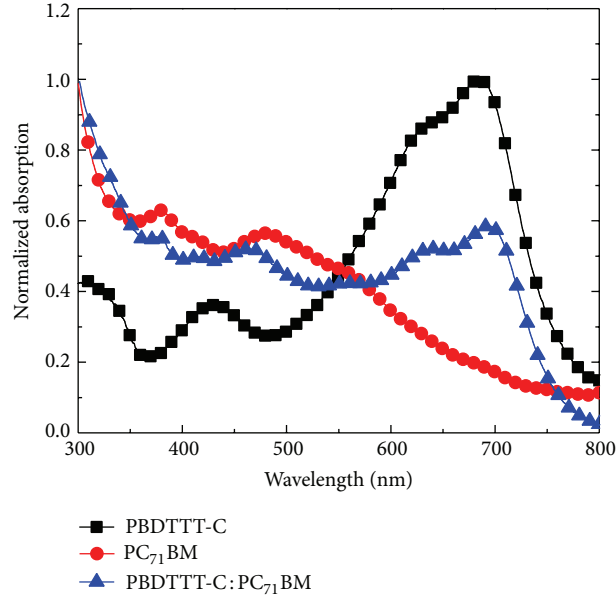


FIGURE 2: Normalized absorption spectra of PBDTTT-C, PC₇₁BM, and their blend films with 1:1.5 weight ratio.

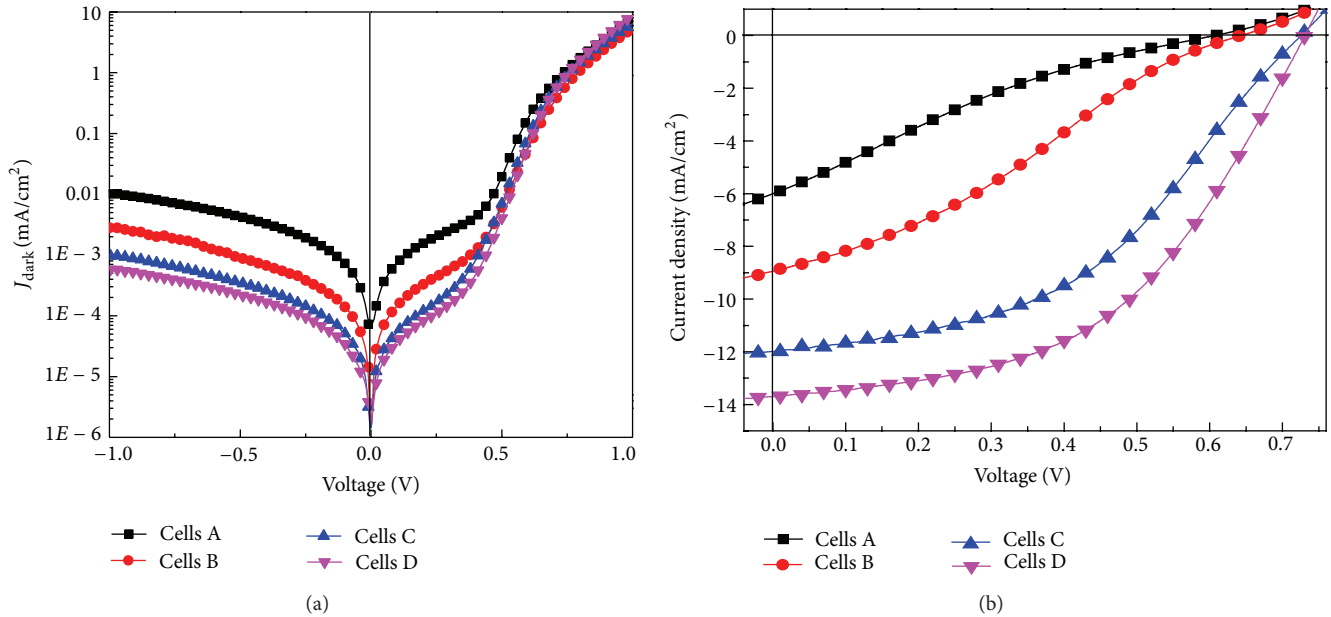


FIGURE 3: (a) Single logarithmic of J - V characteristics curves of PSCs with various anode buffer layers in dark conditions. (b) J - V characteristics curves of PSCs with various anode buffer layers under illumination 100 mW/cm^2 AM 1.5 G simulated solar light.

resistance (R_s) are two important parameters in the PSCs. In contrast to Cells C, the R_{sh} of Cells D was increased about 19% and the R_s was decreased about 44% due to the insertion of a thin LiF layer. The R_{sh} is generally associated with leakage current which is determined by the film quality and its interfaces. Small R_{sh} results from the loss of charge carriers through leakage paths including pinholes in the films and the recombination and trapping of the carriers during their transit through the active layer [23]. The R_s is mainly related to the contact resistance between the active layer and

anode electrode. The decrease of R_s of Cells D should be attributed to the formation of a better ohmic contact due to the insertion of a thin LiF layer.

In order to further clarify the effect of the LiF interlayer on performance of the PSCs, the external quantum efficiency (EQE) spectra of Cells C and D are investigated and shown in Figure 4. It is observed that there is an increase in the EQE at wavelengths between 360 nm and 720 nm for Cells D in comparison to Cells C. The EQE of Cells D with a thin LiF layer is increased up to 60%, which exhibits

TABLE 1: Key photovoltaic parameters for the PSCs with various anode buffer layers under illumination 100 mW/cm² AM 1.5 G simulated solar light.

Samples	V_{oc} (V)	J_{sc} (mA/cm ²)	FF (%)	Best PCE (%)	* Ave. PCE (%)	R_s (Ω cm ²)	R_{sh} (Ω cm ²)
Cells A	0.61	6.0	19.3	0.71	0.63 ± 0.08	177.1	95.7
Cells B	0.64	8.96	29.5	1.69	1.66 ± 0.03	115.5	284.0
Cells C	0.73	11.98	44.5	3.89	3.82 ± 0.07	36.2	321.6
Cells D	0.73	13.70	49.1	4.91	4.86 ± 0.05	20.1	381.9

* Average PCE: more than 30 cells were evaluated.

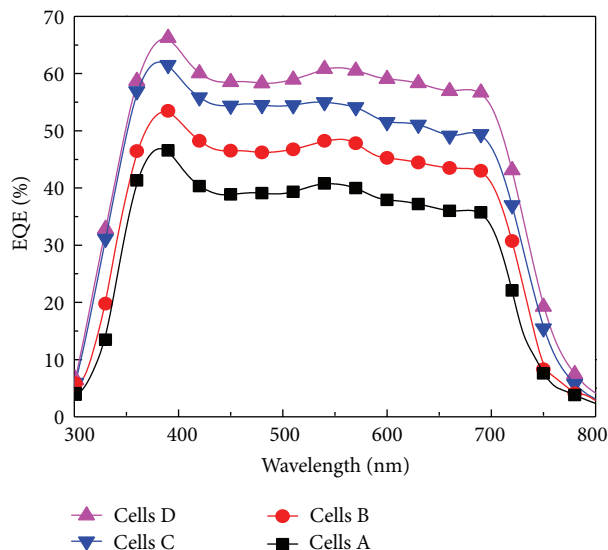


FIGURE 4: The EQE spectra of PSCs with various anode buffer layers.

efficient photon-to-electron conversion. The EQE spectra of PSCs also demonstrate that PEDOT:PSS/LiF as anode buffer layer could play positive effect on charge carrier collection. The adopting appropriate interfacial layers may provide an effective method to improve the performance of PSCs.

4. Conclusions

In summary, a series of PSCs based on PBDTTT-C and PC₇₁BM as active layer were fabricated to investigate the anode buffer layers on the performance of PSCs. The performance of PSCs with PEDOT:PSS/LiF as anode buffer layer was improved compared with the cells fabricated on bare ITO substrates, LiF/ITO substrates, and PEDOT:PSS/ITO substrates. Cells D maintain a maximum J_{sc} and FF, yielding a highest PCE of 4.91%, which has a 26.2% improvement compared to the cells with PEDOT:PSS buffer layer. The improvement performance of PSCs can primarily be attributed to the efficient holes collection induced by the interfacial layer. The PEDOT:PSS/LiF anode buffer layer has positive effect on PSCs based on P3HT:PCBM system. These findings indicate that the optimization of anode buffer layer is an effective method for the improvement of PSCs.

Conflict of Interests

The authors declare that there is no conflict of interests regarding the publication of this paper.

Acknowledgments

This work was supported by Fundamental Research Funds for the Central Universities (2013JBZ004); National Natural Science Foundation of China (61377029); Beijing Natural Science Foundation (2122050); and the State Key Laboratory of Catalysis, CAS (n-11-09).

References

- [1] W. Tang, J. Hai, Y. Dai et al., "Recent development of conjugated oligomers for high-efficiency bulk-heterojunction solar cells," *Solar Energy Materials and Solar Cells*, vol. 94, no. 12, pp. 1963–1979, 2010.
- [2] L. Bian, E. Zhu, J. Tang, W. Tang, and F. Zhang, "Recent progress in the design of narrow bandgap conjugated polymers for high-efficiency organic solar cells," *Progress in Polymer Science*, vol. 37, no. 9, pp. 1292–1331, 2012.
- [3] Z.-L. Zhuo, F.-J. Zhang, X.-W. Xu, J. Wang, L.-F. Lu, and Z. Xu, "Photovoltaic performance improvement of P3HT:PCBM polymer solar cells by annealing treatment," *Acta Physico-Chimica Sinica*, vol. 27, no. 4, pp. 875–880, 2011.
- [4] D. W. Zhao, P. Liu, X. W. Sun, S. T. Tan, L. Ke, and A. K. K. Kyaw, "An inverted organic solar cell with an ultrathin Ca electron-transporting layer and MoO₃ hole-transporting layer," *Applied Physics Letters*, vol. 95, no. 15, Article ID 153304, 2009.
- [5] S.-I. Na, T.-S. Kim, S.-H. Oh, J. Kim, S.-S. Kim, and D.-Y. Kim, "Enhanced performance of inverted polymer solar cells with cathode interfacial tuning via water-soluble polyfluorenes," *Applied Physics Letters*, vol. 97, no. 22, Article ID 223305, 2010.
- [6] Z. He, C. Zhong, X. Huang et al., "Simultaneous enhancement of open-circuit voltage, short-circuit current density, and fill factor in polymer solar cells," *Advanced Materials*, vol. 23, no. 40, pp. 4636–4643, 2011.
- [7] J. Gao, C. L. Perkins, J. M. Luther et al., "N-type transition metal oxide as a hole extraction layer in PbS quantum dot solar cells," *Nano Letters*, vol. 11, no. 8, pp. 3263–3266, 2011.
- [8] C. J. Brabec, S. E. Shaheen, C. Winder, N. S. Sariciftci, and P. Denk, "Effect of LiF/metal electrodes on the performance of plastic solar cells," *Applied Physics Letters*, vol. 80, no. 7, pp. 1288–1290, 2002.

- [9] H. Wang, P. Amsalem, G. Heimel, I. Salzmann, N. Koch, and M. Oehzelt, "Band-bending in organic semiconductors: the role of alkali-halide interlayers," *Advanced Materials*, vol. 26, no. 6, pp. 925–930, 2014.
- [10] M. G. Helander, Z. B. Wang, and Z. H. Lu, "Metal/fullerene electrode structure: physics and device applications," in *Organic Light Emitting Materials and Devices XII*, vol. 7051 of *Proceedings of SPIE*, San Diego, Calif, USA, August 2008.
- [11] H. Xu, L.-Y. Yang, H. Tian, S.-G. Yin, and F.-L. Zhang, "Rhenium oxide as the interfacial buffer layer for polymer photovoltaic cells," *Optoelectronics Letters*, vol. 6, no. 3, pp. 176–178, 2010.
- [12] F. Zhang, X. Xu, W. Tang et al., "Recent development of the inverted configuration organic solar cells," *Solar Energy Materials and Solar Cells*, vol. 95, no. 7, pp. 1785–1799, 2011.
- [13] Y. Liu, F. J. Zhang, H. D. Dai et al., "Interfacial layer for efficiency improvement of solution-processed small molecular solar cells," *Solar Energy Materials and Solar Cells*, vol. 118, pp. 135–140, 2013.
- [14] F. J. Zhang, D. W. Zhao, Z. L. Zhuo, H. Wang, Z. Xu, and Y. S. Wang, "Inverted small molecule organic solar cells with Ca modified ITO as cathode and MoO₃ modified Ag as anode," *Solar Energy Materials and Solar Cells*, vol. 94, no. 12, pp. 2416–2421, 2010.
- [15] D. W. Zhao, S. T. Tan, L. Ke et al., "Optimization of an inverted organic solar cell," *Solar Energy Materials and Solar Cells*, vol. 94, no. 6, pp. 985–991, 2010.
- [16] S. B. Lee, J. Ho Beak, B. H. Kang et al., "The annealing effects of tungsten oxide interlayer based on organic photovoltaic cells," *Solar Energy Materials and Solar Cells*, vol. 117, pp. 203–208, 2013.
- [17] M. T. Greiner, L. Chai, M. G. Helander, W.-M. Tang, and Z.-H. Lu, "Transition metal oxide work functions: the influence of cation oxidation state and oxygen vacancies," *Advanced Functional Materials*, vol. 22, no. 21, pp. 4557–4568, 2012.
- [18] L. Chen, P. Wang, F. Li, S. Yu, and Y. Chen, "Efficient bulk heterojunction polymer solar cells using PEDOT/PSS doped with solution-processed MoO₃ as anode buffer layer," *Solar Energy Materials and Solar Cells*, vol. 102, pp. 66–70, 2012.
- [19] J. H. Seo, D.-H. Kim, S.-H. Kwon et al., "High efficiency inorganic/organic hybrid tandem solar cells," *Advanced Materials*, vol. 24, no. 33, pp. 4523–4527, 2012.
- [20] Z. Wang, F. Zhang, J. Wang et al., "Organic photovoltaic cells: novel organic semiconducting materials and molecular arrangement engineering," *Chinese Science Bulletin*, vol. 57, no. 32, pp. 4143–4152, 2012.
- [21] X. Xi, Q. Meng, F. Li et al., "The characteristics of the small molecule organic solar cells with PEDOT:PSS/LiF double anode buffer layer system," *Solar Energy Materials and Solar Cells*, vol. 94, no. 3, pp. 623–628, 2010.
- [22] K. H. Kim and H. J. Chang, "Effects of buffer layers on properties of bulk hetero junction flexible organic solar cells," *Ceramics International*, vol. 39, no. 1, pp. S605–S609, 2013.
- [23] H. Ma, H.-L. Yip, F. Huang, and A. K.-Y. Jen, "Interface engineering for organic electronics," *Advanced Functional Materials*, vol. 20, no. 9, pp. 1371–1388, 2010.

Research Article

The Promotion of the Efficiency of Organic Photovoltaic Devices by Addition of Anisotropic CdSe Nanocrystals

Shu-Ru Chung,¹ Hong-Shuo Chen,² Chen-Yu Chien,² Meng-Yi Bai,³ and Kuan-Wen Wang²

¹ Department of Materials Science and Engineering, National Formosa University, Yunlin 63201, Taiwan

² Institute of Materials Science and Engineering, National Central University, Taoyuan 32001, Taiwan

³ Graduate Institute of Biomedical Engineering, National Taiwan University of Science and Technology, Taipei 10607, Taiwan

Correspondence should be addressed to Shu-Ru Chung; srchung@nfu.edu.tw and Kuan-Wen Wang; kuanwen.wang@gmail.com

Received 13 March 2014; Revised 28 April 2014; Accepted 30 April 2014; Published 21 May 2014

Academic Editor: Aung Ko Ko Kyaw

Copyright © 2014 Shu-Ru Chung et al. This is an open access article distributed under the Creative Commons Attribution License, which permits unrestricted use, distribution, and reproduction in any medium, provided the original work is properly cited.

CdSe nanocrystals (NCs) with different morphologies have been synthesized and applied as the acceptor in the active layer of the organic photovoltaic (OPV) devices. CdSe tetrapod (TP)/nanorod (NR) with zinc-blended seeds and wurtzite arms is prepared by seed growth method and mixed with poly(3-hexylthiophene) (P3HT): [6,6]-phenyl-C61-butyric acid methyl ester (PCBM). When the concentrations of CdSe in P3HT: PCBM system are 50 wt% optimally, the efficiency can be promoted about 4.3%, suggesting that an enhancement of 13.2% can be obtained and the addition of anisotropic CdSe NCs content in the active layer can be beneficial for the transport of electrons and light absorption in the OPV devices.

1. Introduction

Polymeric solar cells have attracted much attention during the last years due to their lower fabrication cost and possibility of using flexible substrates [1]. However, their efficiency is still about 9%, because various factors, such as photo absorption window and coefficient, excitons separation and transportation, and excitons diffusion length have not been optimized fully [2–6]. Moreover, the active layer morphology related to blend preparation and annealing processes can also influence the efficiency significantly. Park et al. have reported that the power conversion efficiency increases from 0.5 to 2.6% for a single junction cell by carrying out thermal annealing of P3HT:PCBM cell due to the enhanced spectral absorption and decrease in charge carrier recombination [7]. Inorganic semiconductor nanocrystals (NCs), due to their tunable photo absorption window, longer excitons diffusion length, and anisotropic crystal morphology, are promising candidates to be added to improve the photon to current conversion efficiency (PCE) of OPV devices. Celik et al. have reported that the bulk-hetero junction (BHJ) hybrid solar cells based on CdSe nanorods (NRs) and the low band gap polymer poly[2,6-

(4,4-bis-(2-ethylhexyl)-4H-cyclopenta[2,1-b;3,4-b0]-dithiophene)-alt-4,7-(2,1,3-benzothiadiazole)] (PCPDTBT) have PCE about 3.5% [8]. Moreover, the excitons transportation of direction in semiconductor NCs with anisotropic morphologies can improve PCE of polymer-based solar cell [8]. A high short-circuit current density (J_{SC}) can be achieved, which is attributed to the improved CdSe NRs surface modification resulting in lower recombination losses and better charge transport within the inorganic percolation network of the hybrid film [8].

The NCs with different morphologies and novel optical, electronic, and mechanical properties can be prepared by solution-grown methods [9–12]. Currently, NCs are used as electron acceptors in the hybrid NC/polymer solar cells [13]. When increasing the Se content in CdSeTe tetrapods (TPs), the band level positions between the polymer donor and the NCs acceptor may be modified, thereby promoting the open circuit voltage (V_{OC}) and J_{SC} [13]. Furthermore, the use of tetrapod-shaped NCs is an attractive route to obtain high efficiencies through the promotion of electron transport perpendicular to the plane of the film [14]. CdSe NCs acting as electron-transporting and hole-blocking layers can substantially improve cell performance [15]. When CdSe

NCs with different morphologies are blended with poly(3-hexylthiophene) (P3HT), rod-like structures can provide a pathway for the electrons to move away from the dissociation site, which cause enhanced carrier lifetimes and increased devices efficiencies [16]. On the other hand, for CdSe nanoparticles (NPs), due to the lack of dimensionality for charge separation at the polymer/CdSe interface, the performance of CdSe:P3HT devices is poor [16].

The morphology of CdSe NCs can be controlled by reaction temperatures, reaction time, and Cd/Se atomic ratios [17]. Besides, when seeded growth method is used, the structure of the CdSe seeds determines the morphology of CdSe/CdS nanoheterostructures. The CdSe NCs with wurtzite structure seed the formation of CdSe/CdS NRs whereas CdSe with zinc-blended structure initiates the growth of CdSe/CdS TPs [18]. Wurtzite CdS NR and zinc-blended CdSe extensions can also be synthesized by isolation of the first-generation NCs and reintroduction of Cd precursor before injecting the second anion precursor [19].

In this study, we try to investigate the morphological effect of hybrid NRs and TPs on the conversion efficiency of PV cell. CdSe TPs are prepared by seed growth method and zinc-blended CdSe NCs are used as seeds to grow wurtzite CdSe arms. The CdSe NCs dissolved into dichlorobenzene (DCB) and mixed with P3HT: [6, 6]-phenyl-C61-butyric acid methyl ester (PCBM) are used as the active layer of the organic photovoltaic devices (OPV) devices.

The morphology, structure, optical properties, and efficiency detection are analyzed by transmission electron microscopy (TEM), X-ray diffraction (XRD), UV-visible absorption spectroscopy (UV-vis), fluorescence (FL), high fidelity solar simulator, and IV measurement (IV), respectively.

2. Experimental Procedure

2.1. Preparation of CdSe NCs. 2 mmol of CdO and 4 mmol of stearic acid (SA) were mixed in 5 mL 1-octadecene (ODE) and heated to 200°C under Ar. After the solution became clear, the temperature was reduced to RT. 37 mL ODE and 1 mmol of Se powder were then added and the temperature was raised from RT to 240°C with the rise rate of 8°C/min to grow the CdSe seeds. After the temperature reached 240°C, the solution was harvested at room temperature and by washing with methanol it was stored in hexane and named as CdSe-NP. The concentration of the NPs in hexane is about 0.115 M. After that, 3 mL of NPs solution was mixed with 0.4 mmol of Se powders and 1 mL of tri-n-octylphosphine (TOP) as the Se precursor, and Se precursor was injected into Cd precursor of a mixture of 0.8 mmol of CdO, 1.6 mmol of n-hexylphosphonic acid (HPA), and 1.7344 g of tri-n-octylphosphine oxide (TOPO) at 300°C, when the reaction time increases to 60 mins. After that the sample was cooled down to room temperature immediately and purified by hot anhydrous methanol at 70°C to remove residual surfactants and named as CdSe-TP.

2.2. Preparation of OPV Devices. Firstly, the ITO surface was exposed to UV-ozone for 10 min. Then, a PEDOT: PSS layer

was deposited by spin coating with a spin rate of 5000 rpm for 50 sec in order to increase its conductivity and then dried on hot plate at 120°C for 10 min in air. After cooling to room temperature, the ITO glasses were taken into the glove box in high purity nitrogen atmosphere. P3HT and PCBM were dissolved into 0.7 mL dichlorobenzene (DCB) with the weight ratio of 1:1 as the standard active layer solution, and the prepared samples, CdSe TP/NR, were dissolved in the standard active layer solution with the concentration of 10, 30, 50, 100, and 175 wt% and named as CdSe-TP/NR1, 2, 3, 4, and 5, respectively. Moreover, CdSe NP with 50 wt% was also prepared for comparison. The active layer solution was then coated on the PEDOT: PSS layer by spin coating (500 rpm for 50 sec and then 1600 rpm for 1 sec). After that, the ITO glasses were put into the petri dish to have solvent annealing until the surface color turned from yellow to dark purple. The ITO glasses were dried on the hot plate at 150°C for 30 min and cooled down to room temperature. Afterwards the ITO glasses were scratched as a part of the PEDOT: PSS and active layer as the anode. Then the ITO glasses were put on the mask and taken into high vacuum chamber and Ca and Al were evaporated and deposited on the ITO surface as the cathode. In standard device, the thickness of PEDOT:PSS, P3HT:PCBM, and Ca/Al layer is 40, 300, and 50/90 nm, respectively. The active area of all devices is $0.5 \times 0.2 \text{ cm}^2$. The device architecture and the energy band diagram of the CdSe NCs modified OPV cells are illustrated in Figure 1. Based on the energy band diagram we know that the CdSe NCs are promising candidates to transport the electron from PCBM to Al/Ca cathode.

2.3. Characterization. Optical absorption spectra were carried out by UV-visible absorption spectrophotometer (UV-vis) at room temperature (Thermo Fisher Scientific, Evolution 60 s). The light emission spectra of CdSe NCs were determined at room temperature by fluorescence (FL, Hitachi F-7000). Emission spectra were taken by using an excitation wavelength of 365 nm and a slit width of 2.5 nm. The measurements were carried out in the range of 450–700 nm.

The morphologies of CdSe NCs were determined by high resolution transmission electron microscopy (HRTEM, JEOL, JEM-2100). The purified NCs were dispersed in hexane and the solution was dropped on a 300-mesh carbon-coated copper grid and then put into oven (100°C) for 2 hrs followed by natural evaporation at room temperature. The phases and structures of CdSe NCs were detected by X-ray diffraction (XRD) with Cu K α radiation. A Guinier powder diffractometer (Huber, Germany), set at 45° transmission angle, was used in this work. The purpose of solar simulator was to provide a controllable indoor test facility under laboratory conditions.

The standard of solar simulator (Newport, 69911, 95-264VAC, 50/60 Hz, 8AMPS) for the detection of solar cell was under AM 1.5 G and 100 mW/cm². The detection of IV curves for solar cell was measured by the IV measurement (IV, Keithley semiconductor characterization system 4200-SCS and Keithley interactive test environment software). The light source in this case was a class A quality solar simulator (PECeL11, AM1.5G, Peccell Technologies Inc.); light

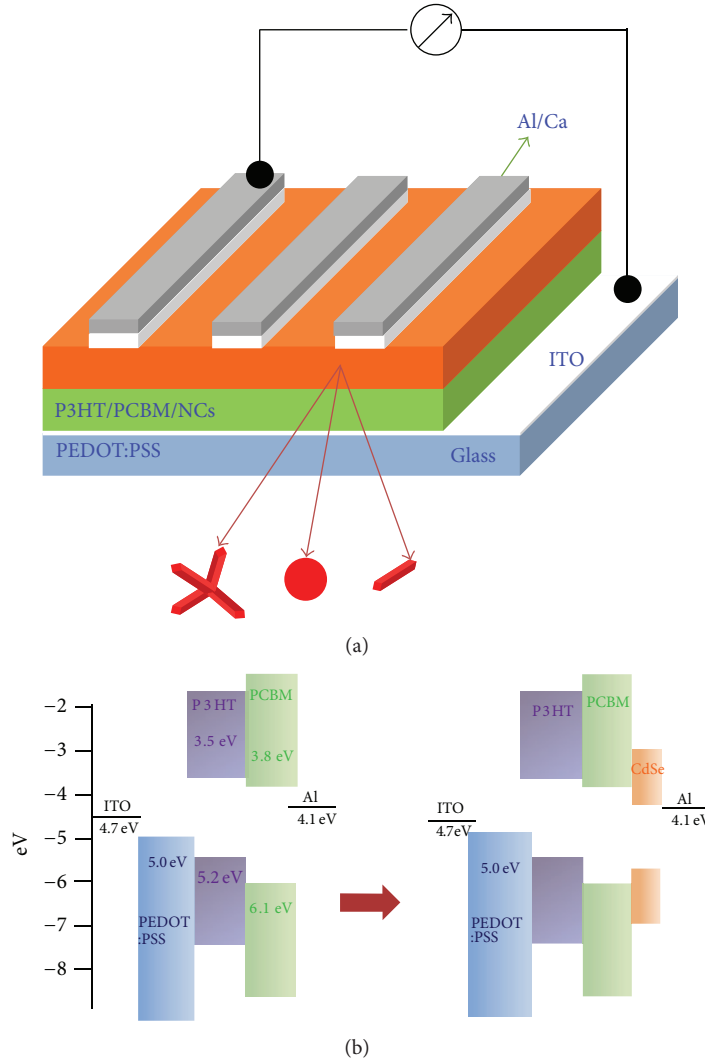


FIGURE 1: The device architecture and the energy band diagram of the CdSe NCs-modified OPV cells.

was focused through a monochromator (Oriel Instrument, Stratford, CT, model 74100) onto the photovoltaic cell. The monochromator was moved in steps from 300 nm to 900 nm (through the visible spectrum) to generate the incident photon to current conversion efficiency (IPCE) as defined in

$$\text{IPCE}(\%) = 1240 \left(\frac{J_{\text{SC}}}{\lambda \phi} \right), \quad (1)$$

where λ is the wavelength, J_{SC} is the short-circuit photocurrent density (mA/cm^2) recorded using a potentiostat/galvanostat, and ϕ is the incident radiative flux (W/m^2) measured using an optical detector (Oriel Instrument, model 71580) and power meter (Oriel Instrument, model 70310) [20].

3. Results and Discussion

3.1. The Physical Properties of CdSe NCs. Since the absorption and emission properties of semiconductor NCs affect the efficiency of OPV, two basic methods, including extending

the absorption window and reducing emission intensity of NCs, have been applied to improve the PCE of devices [21]. The UV-vis and FL spectra of spherical and anisotropic CdSe NCs are compared in Figure 2. Due to the stronger quantum confinement effect for CdSe-NP, their absorption and emission peaks are obvious, implying that electron-hole (e-h) separation and recombination efficiency are good. However, this significant emission behavior for the CdSe-NP sample means that the carrier transport to positive and negative electrodes is poor, which suggests that this CdSe-NP may not have positive effect on the device efficiency when used as acceptor materials. As we have mentioned above that, based on the energy band diagram shown in Figure 1, the CdSe NC can be used as acceptor materials to promote the transportation of the electrons from PCBM to Al/Ca cathode. If the carrier is recombined in CdSe NP, a decrease in the concentration of (e-h) pairs and the number of carriers will be observed in the CdSe NP-modified OPV devices.

On the other hand, in Figure 2, although the absorption edge of CdSe TP/NR is not obvious, its absorption window is

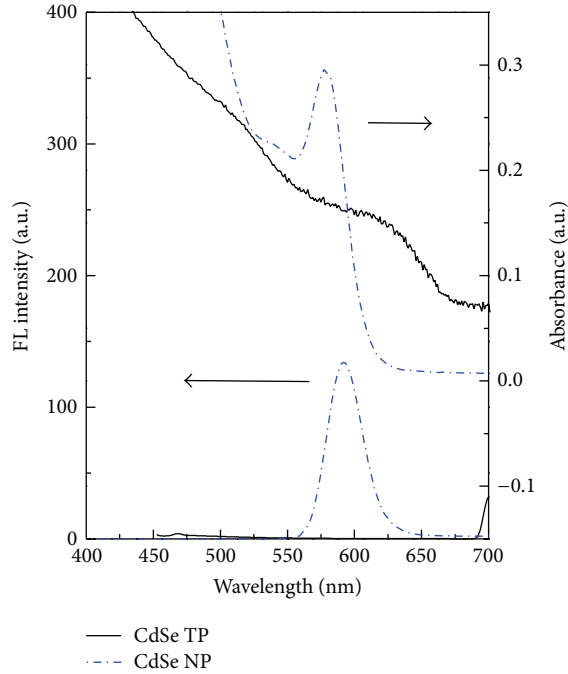


FIGURE 2: The UV-vis and FL spectra of CdSe NCs.

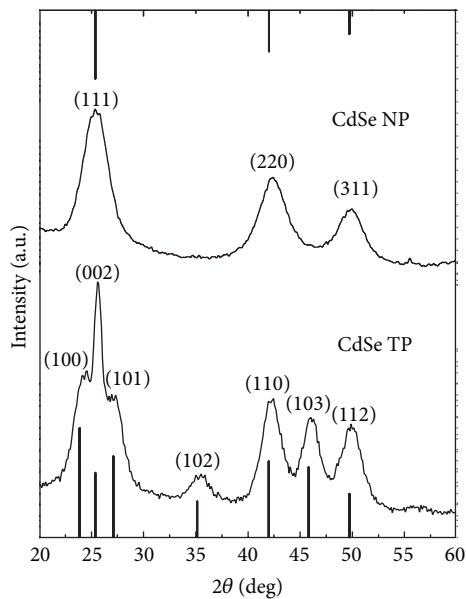


FIGURE 3: The XRD patterns of CdSe NCs.

longer than that of CdSe NP. Moreover, the emission intensity of CdSe-NP is much more obvious than that of CdSe-TP/NR. Since the emission phenomenon of CdSe-TP/NR is suppressed, the sample may not form effective e-h pairs, meaning that the carrier separation may not be effective and e-h pair recombination is suppressed. Therefore, CdSe-NP can effectively form excitons, suggesting that it has better carrier separation efficiency. Because of the large absorption window and lower recombination efficiency in CdSe TP/NR sample, it is expected that the carrier transport to cathode

and anode in this sample is more effectively than that in CdSe NP sample, and the device efficiency of OPV may be improved by combining CdSe TP/NR as donor material. It has been reported that the NCs with different morphologies have a tendency to form directed chains with the particles stacking along their long axis, which can promote the PCE [21].

Figure 3 displays the XRD patterns of CdSe NCs. The peaks of CdSe NP are located at 25.36, 42.01, and 49.72° which belong to (111), (220), and (311) planes of zinc-blended structure (JCPDS 88-2346), respectively. Based on thermodynamics, it has been reported that zinc blend is the most stable form at lower temperature, while wurtzite is more stable in high temperature [20]. For CdSe TP/NR, peaks located at 23.88, 25.39, 27.09, 35.13, 41.99, 45.81, and 49.71° corresponding to wurtzite structure of CdSe (JCPDS 77-0046) are observed, proving that wurtzite arms successfully cover the zinc-blended seeds. It is noted that (002) plane is the preferred orientation and this anisotropic structure of NCs might be beneficial for the conversion efficiency of OPV devices.

Figure 4 displays the morphologies of CdSe NCs by HRTEM. The CdSe NP has spherical shape with an average particle size of 3.6 ± 0.3 nm. On the other hand, the tetrapod and rod-like morphologies are observed with an average length of the arms about 14.0 nm when using HPA and TOPO as cosolvents. The ratio between TP and NR is about 2.3 in the CdSe TP/NR sample. It is reported that HPA molecule can absorb certain crystal surface of CdSe, thereby promoting the same direction growth and resulting in anisotropic morphology [22]. Moreover, based on the above characterizations, it can be summarized that CdSe TP/NR with longer absorption window, lower carrier recombination efficiency, and anisotropic shape may improve the OPV efficiency.

3.2. The Efficiency of OPV Devices Modified by CdSe NC with Various Concentrations. In order to understand the absorption phenomenon of the active layer, the absorbance of CdSe NP and CdSe TP/NR and standard samples under different wavelengths are compared in Figure 5. The absorption curves of CdSe TP/NR and standard sample are very similar in which the absorbance increases slightly in the range from 570 to 610 nm when the P3HT/PCBM is combined with CdSe NCs. Furthermore, although the band gap of CdSe NCs is smaller than that of P3HT/PCBM, the absorption window is not changed significantly. As a result, when the CdSe NCs are mixed with P3HT/PCBM as active layer, the UV-vis spectra are almost the same for all samples, meaning that the light absorption is similar for standard and CdSe NCs modified samples.

As we know that carrier transport efficiency affects the device performance [21], based on previous discussion, although the CdSe TP/NR possesses larger absorption window, poor (e-h) recombination efficiency, preferable orientation, and anisotropic morphology, its UV-vis spectra are almost the same with standard active layer material, meaning that adding CdSe NC may not have positive effect on the

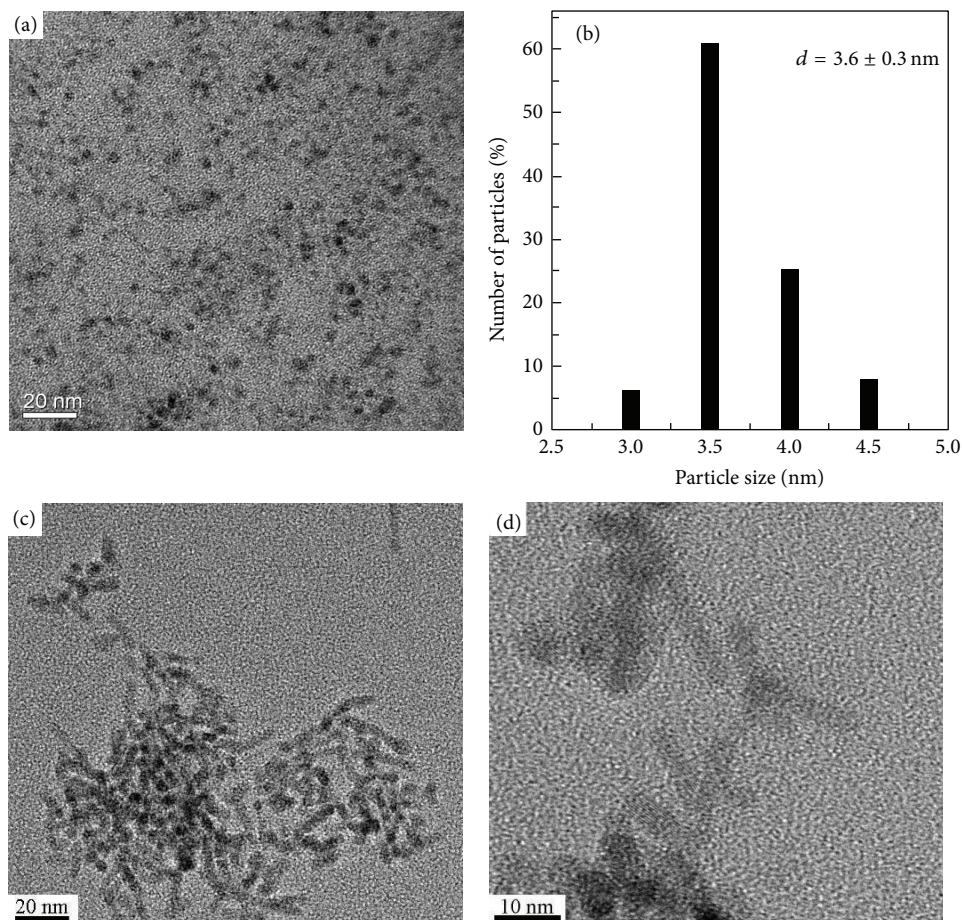


FIGURE 4: (a) TEM micrographs and (b) size distribution of CdSe NP. (c) and (d) are TEM micrographs of CdSe TP/NR.

light absorption and the possibility of IPCE enhancement stemming from light absorption can be ruled out. On the other hand, since the electron mobility in inorganic crystals is faster than that in organic material, the electron transport phenomena may be modified by the addition of CdSe NC, which can also have a chance to promote IPCE. In order to understand the carrier transfer between P3HT/PCBM and CdSe NC modified active layers, the IPCE and device performance of CdSe NP and TP/NR and standard samples are shown in Figure 6 and listed in Table 1. IPCE of the device can be improved by modification of CdSe TP/NR sample in the range of 400 and 600 nm and is decreased significantly by modification with CdSe-NP sample, confirming that anisotropic morphology can benefit the transport of the carrier, but the carrier is consumed and recombined in CdSe NP. Compared to the CdSe NP-modified device, the PCE enhancement is mainly due to the increased J_{SC} . Suggesting that through the addition of a suitable amount of elongated TP/NRs inorganic NC phase, a better connection between PCBM and NCs can be achieved, benefitting the electron transport to the negative electrode.

In order to optimize the concentration of CdSe TP/NR for the modification of the OPV device, the efficiencies of standard sample and CdSe TP/NR modified devices with

various concentrations from 10 to 175 wt% are compared in Table 2 and Figure 7. Among them, the CdSe-TP/NR3 sample has the largest efficiency, suggesting that using CdSe TP/NR with an appropriate concentration to modify the active layer can significantly promote the efficiency by about 4.3% and suggesting an enhancement of 13.2% as listed in Table 2. When the concentration increases from 0 to 10, 30, and 50 wt%, J_{SC} increases from 9.6 to 9.8, 10.1, and 10.9 mA/cm², and the efficiency increases from 3.80 to 3.86, 4.01, and 4.30%, respectively. However, when the concentration further increases to 100 and 175 wt%, J_{SC} decreases to 9.6 and 9.4 mA/cm² and the efficiency decreases to 3.58 and 3.19%, respectively. Similar trend has been observed in the CdSe TPs and poly(2-methoxy-5-(2-ethylhexyloxy)-1,4-phenylene vinylene)(MEH-PPV) system [13]. When the weight ratio of CdSe:MEH-PPV increases from 1:2 to 9:1, the efficiency increases from 0.13 to 1.13%, but when the weight ratio further increases from 9:1 to 20:1, the efficiency then decreases from 1.13 to 0.16%. It seems that increasing CdSe content in the active layer will generate more percolation pathways and help the transport of electrons, thereby increasing the photocurrent and efficiency [13]. However, further increasing CdSe in the active layer decreases the contribution of polymer to the light absorption and destroys the pathway for holes

TABLE 1: The J_{SC} , V_{OC} , FF, efficiency, and enhancement of the standard sample, CdSe-NP, and CdSe-TP/NR3 added OPV device.

Device	J_{SC} (mA/cm ²)	V_{OC} (V)	FF	Efficiency (%)	Improvement (%)
Standard	9.6	0.63	0.63	3.80	0
CdSe-NP	9.0	0.60	0.60	3.26	-14.2
CdSe-TP/NR3	10.9	0.64	0.62	4.30	13.2

TABLE 2: The J_{SC} , V_{OC} , FF, efficiencies, and enhancement of the standard sample and CdSe-TP/NR modified OPV device with different concentrations.

Device	Concentrations (wt%)	J_{SC} (mA/cm ²)	V_{OC} (V)	FF	Efficiency (%)	Improvement (%)
Standard	0	9.6	0.63	0.63	3.80	0
CdSe-TP/NR1	10	9.8	0.62	0.63	3.86	1.5
CdSe-TP/NR2	30	10.1	0.63	0.63	4.01	5.5
CdSe-TP/NR3	50	10.9	0.64	0.62	4.30	13.2
CdSe-TP/NR4	100	9.6	0.62	0.60	3.58	-5.8
CdSe-TP/NR5	175	9.4	0.62	0.55	3.19	-16.0

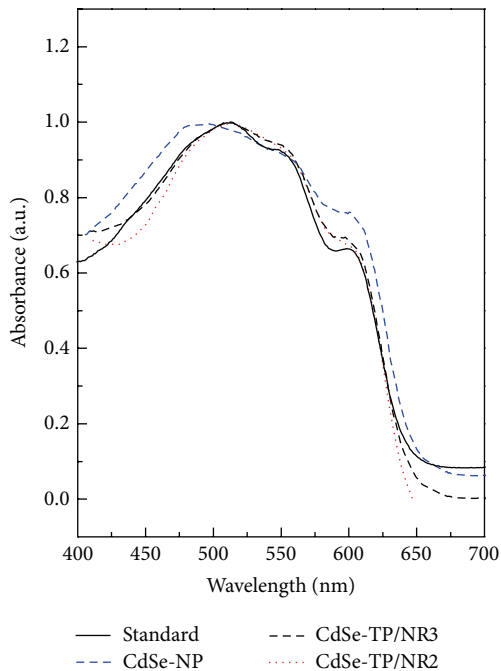


FIGURE 5: The UV-vis of the active layer on ITO glass.

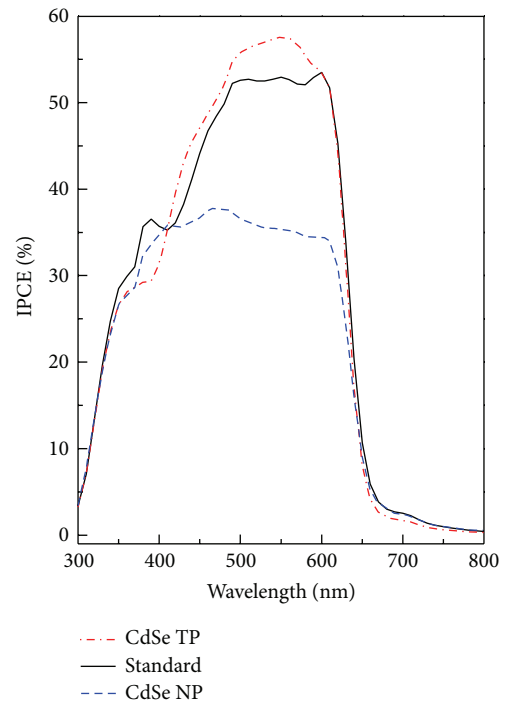


FIGURE 6: IPCE spectra of OPV devices used different addition in active layer.

transport. As a result, the efficiency decreases accordingly [13]. Zhou et al. have pointed out that PCE of blend CdSe NPs and NRs is higher than that of pure NPs and NRs [23]. Besides, higher NP concentration can enhance the PCE. It could be attributed to the improved conductivity of the active layer network due to the addition of suitable amounts of NPs and NRs, which provide more direct and continuous pathways for the electron transport. In our study the ratio between TP and NR is about 2.3 and we know that the TPs can offer more direct and continuous pathways for the electron transport, resulting in more effective power conversion of CdSe-TP/NR samples. Moreover, the optimal concentration of CdSe in P3HT:PCBM system should be 50 wt%.

It is worth mentioning that, in Figure 7, CdSeTP/NR3-device performs a J_{SC} of 10.9 mA/cm², implying that the EQE should be >75%. However, the real EQE displayed in Figure 6 is obviously lower than 75%. Generally, the EQE and conventional efficiency of devices cannot be measured simultaneously. If Ca/Al electrode is evaporated after EQE measurement, the efficiency decreases very significantly. Since the device is prepared under gloves box, the environmental effect can be ignored and similar trends of EQE and J_{SC} for various samples are obtained in this study.

Moreover, it has been reported that when the aspect ratio of the NRs increases from 1 to 10, the charge transport can

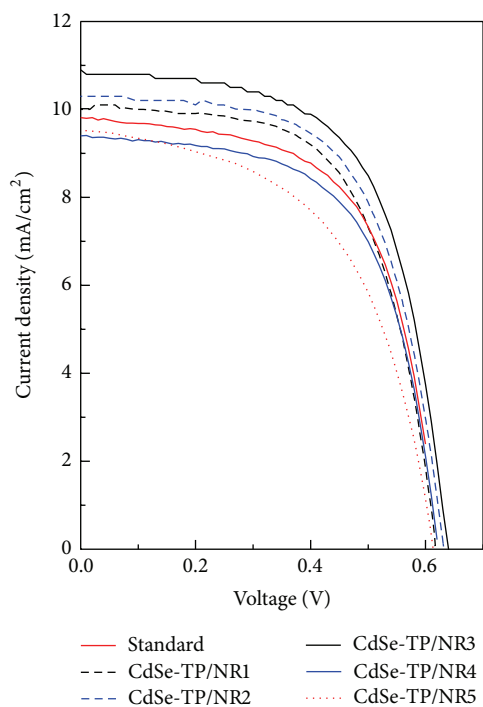


FIGURE 7: The J - V curves of CdSe TP/NR modified devices.

be improved substantially and an EQE enhancement is noted [24]. The cell performance is strongly dependent on blend morphology, and solution-based fabrication techniques often cause uncontrolled and irreproducible blends. As a result, the cell performance of blending with hyperbranched CdSe NCs is better than that of NRs [12]. In principle, elongated or branched NCs such as NRs and TPs can provide more extended electrical conductive pathways, because the number of interparticle hopping events for extracting electrons towards the electrode is reduced. Therefore, it is reported that, for pyridine capped CdSe NCs, devices with NRs and TPs usually exhibit better performance than QDs based devices [24]. However, NRs tend to be horizontally aligned instead of being aligned vertically to the film. In such case, elongated structures are not superior to spherical QDs for extracting free carriers since the electrons need to hop in the vertical direction from the exciton dissociation site to the cathode. It seems that if we can make the larger size of CdSe-NR/TP NCs perpendicular on the PEDOT:PSS film precisely, it will be more beneficial to the charge transport and the enhancement of PCE of devices.

4. Conclusions

In this study, CdSe NCs with spherical-like and tetrapod/rod-like morphologies have been prepared and applied as the donor in the active layer of the OPV devices to increase their photoelectron conversion efficiency. Seed growth synthesis is used for the preparation of CdSe TP/NR samples with a wurtzite arms length of 14.0 nm covering the zinc-blended seeds.

For the devices with concentrations of CdSe TP/NR from 0 to 50 wt%, J_{SC} is increased from 9.6 to 10.9 mA/cm², and efficiency is promoted from 3.80 to 4.30%, respectively, due to the generation of pathways for electrons transport. However, further increasing of the concentration to 100 and 175 wt% decreases the contribution of polymer to the light absorption and destroys the pathway for holes transport. As a result, J_{SC} and efficiency are declined accordingly.

Conflict of Interests

The authors declare that there is no conflict of interests regarding the publication of this paper.

Authors' Contribution

Shu-Ru Chung and Kuan-Wen Wang have contributed equally to this work.

Acknowledgment

This work was supported by the National Science Council of Taiwan under Contract nos. 102-2221-E-008-030, 102-2120-M-007-007, and 102-2218-E-150-001.

References

- [1] Y. Chang and L. Wang, "Efficient poly(3-hexylthiophene)-based bulk heterojunction solar cells fabricated by an annealing-free approach," *Journal of Physical Chemistry C*, vol. 112, no. 45, pp. 17716–17720, 2008.
- [2] X. Wang, T. Ishwara, W. Gong, M. Campoy-Quiles, J. Nelson, and D. D. C. Bradley, "High-performance metal-free solar cells using stamp transfer printed vapor phase polymerized poly(3,4-ethylenedioxythiophene) top anodes," *Advanced Functional Materials*, vol. 22, no. 7, pp. 1454–1460, 2012.
- [3] W. Li, A. Furlan, K. H. Hendriks, M. M. Wienk, and R. A. J. Janssen, "Efficient tandem and triple-junction polymer solar cells," *Journal of the American Chemical Society*, vol. 135, pp. 5529–5532, 2013.
- [4] J. M. Lobe, T. L. Andrew, V. Bulović, and T. M. Swager, "Improving the performance of P3HT-fullerene solar cells with side-chain-functionalized poly(thiophene) additives: a new paradigm for polymer design," *ACS Nano*, vol. 6, no. 4, pp. 3044–3056, 2012.
- [5] K. Foe, G. Namkoong, M. Samson, E. M. Younes, I. Nam, and T. M. Abdel-Fattah, "Stability of high band gap P3HT :PCBM organic solar cells using TiO_x interfacial layer," *International Journal of Photoenergy*, vol. 2014, Article ID 784724, 6 pages, 2014.
- [6] Z. He, C. Zhong, S. Su, M. Xu, H. Wu, and Y. Cao, "Enhanced power-conversion efficiency in polymer solar cells using an inverted device structure," *Nature Photonics*, vol. 6, pp. 591–595, 2012.
- [7] S. K. Park, Y. H. Kim, and J. I. Han, "Effect of annealing treatment and surface morphology on power conversion in organic photovoltaics," *Japanese Journal of Applied Physics*, vol. 48, no. 8R, Article ID 081505, 3 pages, 2009.
- [8] D. Celik, M. Krueger, C. Veit et al., "Performance enhancement of CdSe nanorod-polymer based hybrid solar cells utilizing

- a novel combination of post-synthetic nanoparticle surface treatments,” *Solar Energy Materials and Solar Cells*, vol. 98, pp. 433–440, 2012.
- [9] Y.-W. Jun, S.-M. Lee, N.-J. Kang, and J. Cheon, “Controlled synthesis of multi-armed CdS nanorod architectures using monosurfactant system,” *Journal of the American Chemical Society*, vol. 123, no. 21, pp. 5150–5151, 2001.
- [10] L. Fang, J. Y. Park, Y. Cui et al., “Mechanical and electrical properties of CdTe tetrapods studied by atomic force microscopy,” *Journal of Chemical Physics*, vol. 127, no. 18, Article ID 184704, 2 pages, 2007.
- [11] T. Mokari, E. Rothenberg, I. Popov, R. Costi, and U. Banin, “Selective growth of metal tips onto semiconductor quantum rods and tetrapods,” *Science*, vol. 304, no. 5678, pp. 1787–1790, 2004.
- [12] I. Gur, N. A. Fromer, C. Chen, A. G. Kanaras, and A. P. Alivisatos, “Hybrid solar cells with prescribed nanoscale morphologies based on hyperbranched semiconductor nanocrystals,” *Nano Letters*, vol. 7, no. 2, pp. 409–414, 2007.
- [13] Y. Zhou, Y. Li, H. Zhong et al., “Hybrid nanocrystal/polymer solar cells based on tetrapod-shaped CdSe_xTe_{1-x} nanocrystals,” *Nanotechnology*, vol. 17, no. 16, pp. 4041–4047, 2006.
- [14] B. Sun, E. Marx, and N. C. Greenham, “Photovoltaic devices using blends of branched CdSe nanoparticles and conjugated polymers,” *Nano Letters*, vol. 3, no. 7, pp. 961–963, 2003.
- [15] J. H. Jeon, D. H. Wang, H. Park, J. H. Park, and O. O. Park, “Stamping transfer of a quantum dot interlayer for organic photovoltaic cells,” *Langmuir*, vol. 28, no. 25, pp. 9893–9898, 2012.
- [16] S. Dayal, M. O. Reese, A. J. Ferguson, D. S. Ginley, C. Rumbles, and N. Kopidakis, “The effect of nanoparticle shape on the photocarrier dynamics and photovoltaic device performance of poly(3-hexylthiophene):CdSe nanoparticle bulk heterojunction solar cells,” *Advanced Functional Materials*, vol. 20, no. 16, pp. 2629–2635, 2010.
- [17] Z. A. Peng and X. Peng, “Nearly monodisperse and shape-controlled CdSe nanocrystals via alternative routes: nucleation and growth,” *Journal of the American Chemical Society*, vol. 124, no. 13, pp. 3343–3353, 2002.
- [18] D. V. Talapin, J. H. Nelson, E. V. Shevchenko, S. Aloni, B. Sadtler, and A. P. Alivisatos, “Seeded growth of highly luminescent CdSe/CdS nanoheterostructures with rod and tetrapod morphologies,” *Nano Letters*, vol. 7, no. 10, pp. 2951–2959, 2007.
- [19] D. Milliron, S. M. Hughes, Y. Cui et al., “Colloidal nanocrystal heterostructures with linear and branched topology,” *Nature*, vol. 430, no. 6996, pp. 190–195, 2004.
- [20] Z. Deng, L. Cao, F. Tang, and B. Zou, “A new route to zinc-blende CdSe nanocrystals: mechanism and synthesis,” *Journal of Physical Chemistry B*, vol. 109, no. 35, pp. 16671–16675, 2005.
- [21] W. U. Huynh, X. Peng, and A. P. Alivisatos, “CdSe nanocrystal rods/poly(3-hexylthiophene) composite photovoltaic devices,” *Advanced Materials*, vol. 11, no. 11, pp. 923–927, 1999.
- [22] K. P. Rice, A. E. Saunders, and M. P. Stoykovich, “Seed-mediated growth of shape-controlled wurtzite CdSe nanocrystals: platelets, cubes, and rods,” *Journal of the American Chemical Society*, vol. 135, no. 17, pp. 6669–6676, 2013.
- [23] Y. Zhou, M. Eck, C. Men et al., “Efficient polymer nanocrystal hybrid solar cells by improved nanocrystal composition,” *Solar Energy Materials and Solar Cells*, vol. 95, no. 12, pp. 3227–3232, 2011.
- [24] W. U. Huynh, J. J. Dittmer, and A. P. Alivisatos, “Hybrid nanorod-polymer solar cells,” *Science*, vol. 295, no. 5564, pp. 2425–2427, 2002.